seit 1558

Improving Structured Illumination Microscopy by blind reconstruction and multifocus detection

Dissertation

zur Erlangung des akademischen Grades

Doctor rerum naturalium (Dr. rer. nat.)

vorgelegt dem Rat der

Chemisch-Geowissenschaftlichen Fakultät

der Friedrich-Schiller-Universität Jena

von M.Sc. Aurélie Jost

geboren am 06.03.1988 in Straßburg, Frankreich

Gutachter

1. Prof. Dr. Rainer Heintzmann

2. Prof. Dr. Michael Schmitt

Tag der öffentlichen Verteidigung: 09.08.2017

Zusammenfassung

Mikroskopie mit strukturierter Beleuchtung (SIM) zählt zu den hochauflösenden Mikroskopieverfahren und erreicht die doppelte Auflösung im Vergleich zur normalen Weitfeldmikroskopie. Bei SIM wird die Probe mit einem Muster - typischerweise einem Lichtgitter - beleuchtet. Dieses Muster entsteht durch die Interferenz zweier oder dreier ebener Wellen.

Die nötige Datenverarbeitung der rohen SIM-Bilder führt zu Artefakten, wenn das Beleuchtungsmuster unbekannt oder verzerrt ist. Blind-SIM ist ein Entfaltungsbasierter Ansatz, der sowohl die Rekonstruktion der Probe als auch die des Beleuchtungsmusters ermöglicht. Blind-SIM ist fähig, Daten mit völlig oder teilweise unbekanntem Beleuchtungsmuster zu bearbeiten und ist deswegen robust gegenüber Verzerrungen dieser Muster. *Thick slice* blind-SIM hingegen erzeugt einen 3D Stapel aus einer 2D-Aufnahme. Dadurch ist es in der Lage, Beiträge von Licht außerhalb der Fokusebene ("out-of-focus") zu entfernen. Dieses Licht würde anderenfalls die Bildqualität von dicken Proben beeinträchtigen. Durch das Zweistrahl-SIM-Verfahren lassen sich entweder optisch Probenschnitte erzeugen ("optisches Sectioning") oder eine Maximierung der lateralen Auflösung erzielen. Eine Kombination mit *thick slice* blind-SIM ermöglicht beides gleichzeitig. *Thick slice* blind-SIM zeigt durch die Bearbeitung einer einzelnen ausgewählten Ebene eine vergleichbare Verbesserung des Auflösungsvermögens und der optische Sectioning Fähigkeit wie die 3D Bearbeitung eines 3D aufgenommenen SIM Stapels.

Da SIM eine Weitfeld-detektion benutzt, bietet es einen Geschwindigkeitsvorteil im Vergleich zu anderen hochauflösenden Ansätzen. Die Aufnahmegeschwindigkeit für 3D SIM ist durch axiales mechanisches Abtasten in Verbindung mit Nachfokussierung begrenzt, wohingegen eine multifokus Detektion die gleichzeitige Aufnahme einer fokalen Serie ermöglicht. Die Kombination von SIM-Anregung und multifokus Detektion (MF-SIM) ermöglicht es, die Aufnahmegeschwindigkeit von 3D SIM

zu verbessern. Das MF-SIM Verfahren macht neue Ansätze der Rekonstruktion nötig, wofür sich ein entfaltungsbasierter Algorithmus, welcher auf bekannten 3D-Beleuchtungsmustern beruht, eignet.

Abstract

Structured Illumination Microscopy (SIM) is a super-resolution microscopy method which enables a two-fold resolution enhancement with respect to classical wide-field (WF) fluorescence microscopy. In SIM, the sample is illuminated by a pattern, typically a sinusoidal grid of light. This pattern is typically the result of interference of either two or three plane waves.

The wide dissemination of SIM is limited by the difficulties arising during the necessary numerical reconstruction. Artefacts are observed in the SIM reconstructed images if the illumination pattern is distorted or unknown. Blind-SIM is a deconvolution-based reconstruction approach that enables to reconstruct both the sample and the illumination pattern. Blind-SIM is able to reconstruct partially or fully unknown illumination patterns and is therefore robust to distortions. However, so far blind-SIM was not able to process data from thick samples where the visibility of the fringes is reduced by the presence of out-of-focus light. In this work, we present the *thick slice* blind-SIM algorithm which reconstructs a 3D stack from a 2D measurement, thus removing the out-of-focus light. Furthermore, *thick slice* blind-SIM is a possible computational approach for solving the dilemma between optical sectioning and lateral resolution in the two-beam SIM method.

The fact that the SIM method uses a WF acquisition scheme gives it a speed advantage compared to other super-resolution approaches. However, the acquisition speed in 3D SIM is limited by the axial scanning and sequential focusing. Using a multifocus detection enables to simultaneously acquire a focal series. Merging SIM excitation with multifocus detection (MF-SIM) permits to enhance the volumetric acquisition speed of 3D SIM as well as removing the need for axial mechanical scanning, a source of sample drift and vibrations. The recorded MF-SIM data does not obey the same theoretical description as the conventional scanning 3D SIM data. Hence, the classical approach for 3D SIM reconstruction cannot be applied. We

developed a deconvolution-based algorithm using known 3D illumination pattern that can be applied to the reconstruction of MF-SIM data. The results demonstrate enhanced resolution in all three dimensions.

Mathematical operators

$\lvert\cdot\rvert$	Absolute value norm	$\lvert\boldsymbol{u}\rvert = \sum_{m=1}^{n} \lvert u_m\rvert$
$\lVert\cdot\rVert$	Euclidian norm	$\lVert\boldsymbol{u}\rVert^2 = \sum_{m=1}^{n} \lvert u_m\rvert^2$
$\langle\cdot,\cdot\rangle$	Scalar product	$\langle\boldsymbol{u},\boldsymbol{v}\rangle = \sum_{m=1}^{n} u_m v_m^*$
$\otimes$	Convolution	$(f\otimes g)(\boldsymbol{r}) = \int_{\mathbb{R}^n} f(\boldsymbol{r'})\cdot g(\boldsymbol{r}-\boldsymbol{r'})d\boldsymbol{r'}$
$\tilde{\cdot}$	Fourier transformation (FT)	$\tilde{f}(\boldsymbol{k}) = \left(\frac{1}{2\pi}\right)^{\frac{n}{2}} \int_{\mathbb{R}^n} f(\boldsymbol{r})\cdot e^{-i2\pi\boldsymbol{k}\cdot\boldsymbol{r}} d\boldsymbol{r}$

Contents

1. Introduction

Parts of this chapter including figures have been published in [1]:

1. The introduction to section 1.1, the beginning of section 1.1.1 and the second paragraph of section 1.1.2;
2. Section 1.2.1;
3. The first paragraph as well as the fourth to eighth paragraphs of section 1.2.2;
4. Section 1.2.3 except for its last paragraph.
5. Fig. 1.4 and its caption was used without modification;
6. Figs. 1.1, 1.3, 1.5, 1.8 and 1.9 and their captions were very slightly modified.

Microscopy is an essential tool for research in biology, enabling the observation of intra-cellular features and processes. The performance of a microscope as measuring device can be assessed according to several criteria, for instance lateral resolution, frame rate and axial resolution. Quite often, improving one characteristic comes at the cost of another one. Recent approaches emphasize selected requirements, thus becoming tailored for specific applications or samples.

In this chapter, the scope of work of this thesis will be defined. For this, we will first introduce important notions for work in the field of fluorescence microscopy and the wide field of high resolution techniques. Then, background information on Structured Illumination Microscopy will be given.

1.1. Fundamentals

This work stays within the framework of fluorescence microscopy. Label-free methods receive much attention due to the growing concern that excessive interaction with the sample may hinder the relevancy of the observations into question. However, fluorescence microscopy is a very successful method for imaging biological samples. It is very popular because specific targets inside a cell under study can be labelled and are then brightly visible on a dark background. It offers good contrast and sensitivity down to the single-molecule regime because the wavelength of the emitted light differs from the excitation wavelength. Finally, fluorescent light is, unlike back-scattered light, incoherent between different molecules, establishing a very useful linear imaging relationship between the emitted light and the detected intensity image [1].

One accepted way to quantify resolution is through the criterion of the Abbe limit [2]. Let us assume an object made of thin parallel lines placed at a repetition distance d. When d gets smaller, it is commonly said that the grating gets finer or its spatial frequency increases. The resolution limit is the cut-off distance under which the contrast of the image of this grating will be zero, and the grating will not be visible any more:

$$d_{min} = \frac{\lambda_{em}}{2\mathrm{NA}} \tag{1.1}$$

is the minimum resolvable distance using a standard full-field epifluorescence microscope, often called wide-field (WF) microscope, when one is using emission light with a wavelength in vacuum of λ_{em} and a microscope objective of numerical aperture

$$\mathrm{NA} = n \sin \alpha \tag{1.2}$$

where α is the half opening angle of the detection objective and n is the refractive index of the immersion medium. A typical d_{min} figure for the diffraction limit in the field of optical microscopy is 200 nm as further explained in section 1.1.1.

The field of fluorescence microscopy has witnessed the creation of several novel methods in the last decades, several of which claiming super-resolution [3, 4, 5, 6]. Even though Abbe's equation 1.1 was first conceived for the case of transmission

imaging under oblique illumination, the same equation applies just as well to the case of imaging the incoherent fluorescence emission. It is agreed to qualify a method as super-resolving if its measured resolution is below what Abbe's diffraction limit predicts. An overview of various super-resolution microscopy techniques is given in section 1.2.1.

1.1.1. Image formation in fluorescence microscopy

Each fluorophore can be considered as a point in the sample plane. However, due to diffraction, the resulting image of this point will be blurred. This blurred spot, termed the point spread function (PSF), has (approximately) the shape of an Airy pattern. As a consequence, two fluorophores that stand close to each other will produce a wide blurred area, each individual PSF overlapping with its neighbour's. It will be difficult to resolve them, *i.e.* to discriminate that there are two emitters in this area, as can be seen in fig. 1.1b: this is the Rayleigh resolution criterion. A useful piece of knowledge about a microscope is the so-called transverse full width at half maximum (FWHM) of the measured PSF. If no further precision is given, the FWHM refers to the lateral extent of the 2D PSF. As per conventional notation, we denote the lateral dimensions as x and y, and the axial direction along which the light travels as z. The FWHM is represented in fig. 1.1a and has a value in the paraxial approximation of [7]:

$$\mathrm{FWHM}_{x,y} = 0.52\frac{\lambda_{em}}{\mathrm{NA}}, \tag{1.3}$$

with the same variables as eq. 1.1, *i.e.* the value of the FWHM is very close to the value of Abbe's diffraction limit. For NA = 1.4 (reachable with an oil immersion objective of $n = 1.516$) and a central wavelength of $\lambda_{em} = 550\,\mathrm{nm}$, we estimate a FWHM of 204 nm in the lateral direction. Using the same values for the NA and λ_{em} in Abbe's equation 1.1 yields $d_{min} = 196\,\mathrm{nm}$. The usual order of magnitude taken as the diffraction limit is 200 nm.
FWHM measurements are still a commonly used tool to compare the resolution of different microscopes, however the results should be analysed with respect to eq. 1.1, especially for super-resolution methods [5, 6].

The experimental PSF can be acquired by imaging a sample made of many isolated

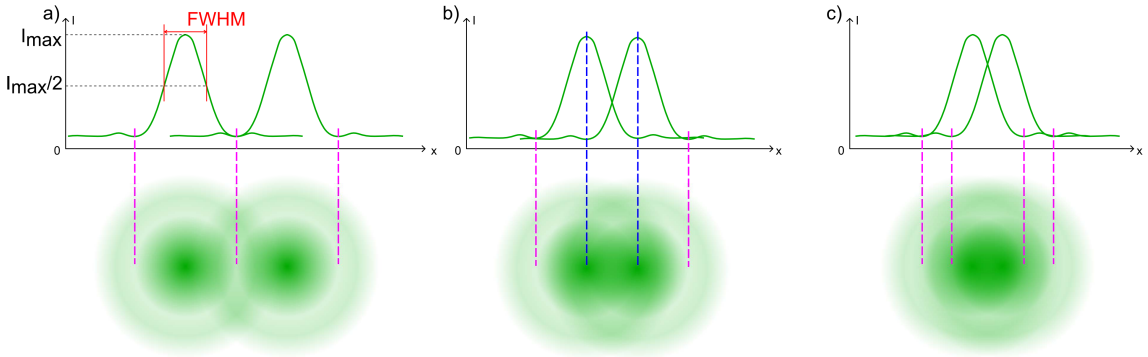

Figure 1.1.: The Point Spread Function (PSF) and the Rayleigh resolution criterion. The Rayleigh criterion is another accepted way to define the resolution. Airy discs (bottom row) as a model for the PSFs of two neighbouring point sources and their corresponding intensity profiles (top row). The magenta dashed lines indicate the position of the first minimum. a) The distance between the two points is larger than the resolution limit: They are resolved. The FWHM of the PSF is indicated in red. b) The two blue dashed lines are separated by a radius of the Airy patterns $R_{Airy} = \frac{1.22\lambda_{em}}{2\mathrm{NA}}$ where λ_{em} is the wavelength of light and NA is the numerical aperture. R_{Airy} is the value of the resolution limit when the Rayleigh criterion is used. c) The distance between the two point sources is smaller than the resolution limit: they are not resolved.

fluorescent particles - beads - of a diameter which is much smaller than the diffraction limit as indicated by Abbe's equation. Typically, 100 nm beads are used, or even smaller ones. Several - at least 10 or more - isolated beads are selected, averaged, and a fit is performed, thus yielding the experimental PSF.

The fluorescent labelled structure is described by its fluorophores density, all fluorophores being seen as single point sources emitting light in the same way. Each of these point sources is imaged as a PSF, a process which is mathematically described by a convolution operation. Therefore, if all fluorophores were equally excited, as it is the case in WF microscopy, and hence are homogeneously emitting in the whole field, then the perfect measured image is

$$I_{\mathrm{perf}} = \rho \otimes h, \tag{1.4}$$

where I_{perf} is the detected image in the absence of noise, ρ is the distribution of fluorophores - describing the sample as explained above, the PSF is denoted as h is the PSF and $\otimes$ stands for the convolution operator.

In the real case, there is noise and the detected image is

$$I_{det} = \rho \otimes h + \mathcal{N} \ , \tag{1.5}$$

with $\mathcal{N}$ accounting for the noise.

1.1.2. Introduction to the Fourier Transform

For the purpose of theoretical description, it is useful to consider the sample ρ as a linear combination of sinusoidal functions, an operation known as Fourier series expansion [8]. The Fourier spectrum of ρ is therefore a representation in k_x, k_y - called the k-space or Fourier space - of the spatial frequency components that are actually included in the decomposition of ρ. The mathematical definition of the Fourier Transform (FT) is included in the preamble chapter "mathematical operators".

Convolution in real space, as in eq. 1.4, has the interesting property of being equivalent to multiplication of the respective Fourier-transformed functions in Fourier space (convolution theorem). The FT of the whole microscope's PSF is called the Optical Transfer Function (OTF). The FT of the sample is multiplied by the OTF of the microscope (see eq. 1.6). Each lens or group of lenses (achromatic doublet, objective...) performs a Fourier Transform between the principal planes. Therefore, an imaging system like a microscope possesses several image and Fourier planes. The back focal plane (BFP) of the microscope objective is a Fourier plane, and is also sometimes referred to as pupil plane.

In Fourier space, eq. 1.4 becomes

$$\tilde{I}_{\text{perf}} = \tilde{\rho} \cdot \tilde{h} \ , \tag{1.6}$$

where $\tilde{}$ represents the FT. $\tilde{h}$ represents therefore the OTF.

The resolution of an optical system is fundamentally limited by the support of the OTF, which defines the maximum spatial frequency range that can be transmitted. The support of the WF OTF is depicted in fig. 1.2.

In the Fourier space, the counterpart of the diffraction limit (given in nm) is therefore

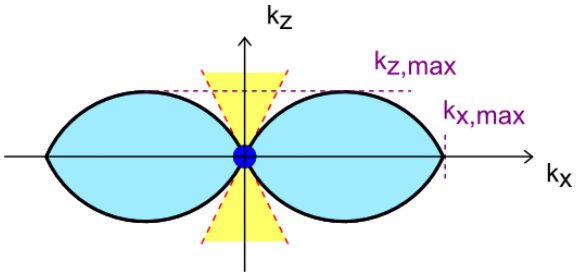

Figure 1.2.: The support of the OTF in a WF microscope, describing the spatial frequencies that can be imaged. The cut-off frequencies are a linked to the diffraction limit. The missing cone (yellow) corresponds to a range of frequencies close to the k_z axis that cannot be transmitted.

the highest transmittable spatial frequency $k_{x,max}$ as denoted in fig. 1.2:

$$k_{x,max} = \frac{2\mathrm{NA}}{\lambda_{em}}, \tag{1.7}$$

Since the OTF is symmetrical around the k_z axis, the same applies along y.

Apart from the lateral resolution, another important feature of a microscope is the axial resolution. In a WF microscope, the highest transmittable axial frequency is [9]:

$$k_{z,max} = \frac{\mathrm{NA}}{\lambda_{em}} \frac{(1-\cos\alpha)}{\sin\alpha}, \tag{1.8}$$

where $k_{z,max}$ is the highest transmittable axial frequency in the WF case and the other variables are similar to the ones employed in eq. 1.1. A graphical representation of $k_{z,max}$ is available in fig. 1.2.

As can be seen in fig. 1.2, the WF microscope cannot transmit spatial frequencies around the k_z axis, this is the so-called missing cone as depicted in yellow in fig. 1.2. As a consequence, structures of very low lateral frequency, e.g. fluorescent planes, yield uniform brightness and, thus, cannot be axially resolved. Due to the missing cone, out-of-focus light distributes only to other regions, but its sum does not weaken. One of the goals of microscopy techniques is to fill this missing cone. When this goal is achieved, the microscope can perform optical sectioning.

Due to the missing cone, the axial resolution is not directly linked to the axial cut-off

frequency $k_{z,max}$ since it depends on the lateral frequency $k_{x,max}$. However, if we want to get an estimate of the axial resolution in a WF microscope for an object that contains a lateral frequency of $k_{x,max}/2$, we can take the inverse of eq. 1.8 and apply the same values for NA, n and λ_{em} as in section 1.1.1:

$$\frac{1}{k_{z,max}} = \frac{\lambda_{em}}{\mathrm{NA}} \frac{\sin\alpha}{(1-\cos\alpha)} = \frac{\lambda_{em}}{n\,(1-\cos\alpha)}, \tag{1.9}$$

with

$$\alpha = \arcsin\frac{\mathrm{NA}}{n}, \tag{1.10}$$

then we get a value for $1/k_{z,max}$ of 589 nm. A generally accepted estimate for the axial resolution of a WF microscope is 600 nm [2, 9].

True super-resolution methods have an effective PSF which is thinner and an OTF which is wider - at least in k_x, k_y- than in the diffraction-limit case, *i.e.* their effective cut-off frequency is higher than $k_{x,max}$ in eq. 1.7.

More thorough discussions are found in [1, 9, 10, 11].

1.2. Structured Illumination Microscopy

1.2.1. Super-resolution microscopy

A number of superresolution methods have been recently developed [3, 4, 5, 6]. They bypass the diffraction limit, resolving structural details spaced by distances well below 100 nm. Stimulated Emission Depletion (STED) [12], Photoactivated Localization Microscopy (PALM) [13], Stochastic Optical Reconstruction Microscopy (STORM) [14], and Structured Illumination Microscopy (SIM) are examples [15, 16].

In STED, a focused laser beam excites the electrons to an upper level. A doughnut-shaped second beam of a different color de-excites the fluorophores by the stimulated emission process, thus minimizing the region of spontaneous fluorescence, leading to improved resolution, as can be seen in fig. 1.3.

Pointillistic imaging techniques - also referred to as single molecule localization

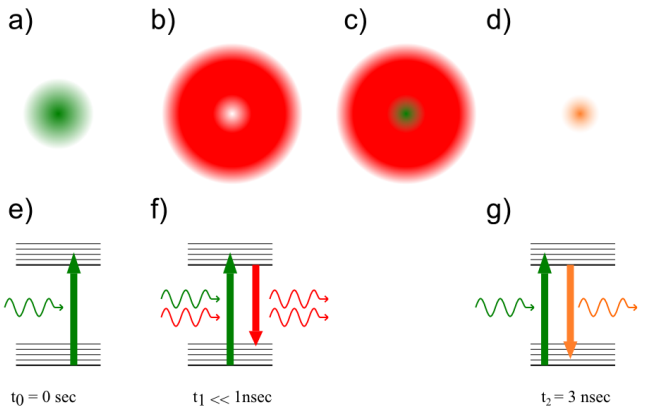

Figure 1.3.: The excitation and de-excitation processes in stimulated emission depletion (STED). a) Excitation PSF. Its size is limited by diffraction of the excited light through the objective. e) Corresponding transition in the Jablonski energy scheme. b) Stimulated emission doughnut-shaped beam. f) The fluorophores within the region of the doughnut are forced to the ground state by the stimulated emission process. The fluorophores in the very center of the doughnut beam remain in the excited state. c) The two previous beams are superimposed and scanned along the region of interest. d) Effective PSF of the combined effects. g) The fluorophores that have not been de-excited by the STED beam can emit fluorescent photons, which come from a region of much smaller radius.

microscopy (SMLM) techniques - like PALM and STORM utilize the property that fluorophores can be sparsely randomly activated, thus leading to a separation in time of the individual images of the fluorophores. Their positions can be determined very precisely by a fit (e.g., using a Gaussian) with a precision far better than the Abbe limit. The result is a pointillistic map of estimated locations, hence the name pointillistic imaging [17]. In PALM, this separate activation is achieved through the use of photoactivatable fluorophores, and in STORM with photoswitchable fluorophores, as can be seen in fig. 1.4.

STED is a point-scanning technique. Its speed is thus limited by its scanning mechanism and the size of the area to be scanned. PALM and STORM are wide-field methods requiring hundreds [18] to tens of thousands [13] of individual images. SIM is also a wide-field method, but it requires the acquisition of only a few frames, as explained in section 1.2.4 and in [1].

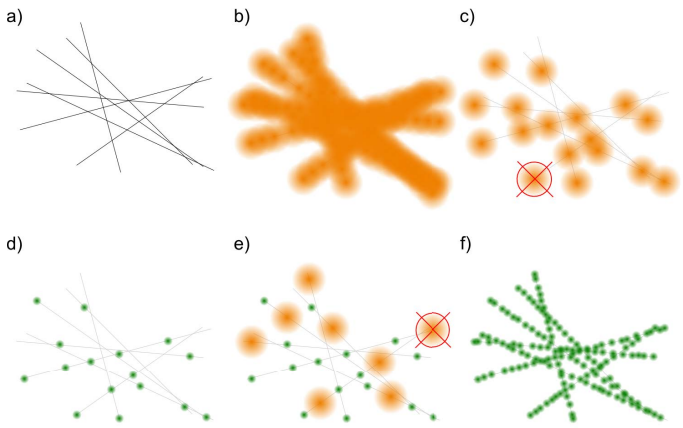

Figure 1.4.: Principles of PALM and STORM. a) Sample consisting of many point sources. b) Simultaneous emission of all the fluorescent markers. c) When photoactivatable (PALM) or photoswitchable (STORM) dyes are used, only very few molecules will emit light in each single frame. A Gaussian fit (red circle) is applied to each of these single-molecule images. The center (red cross) corresponds to the most probable position of the initial point source. d) Location map after processing of a single frame. The green dots represent the estimation of the position with nanometre precision. e) Another camera frame in which another set of fluorophores are shown. The processing procedure is repeated frame by frame. f) After acquisition and processing of many frames, structural information about the sample is pointillistically reconstructed at a much better resolution.

1.2.2. First notions in Structured Illumination Microscopy

Structured illumination microscopy (SIM) is another super-resolution technique. A commercial structured illumination microscope (SIM) offers a resolution of the order of 100 nm. In SIM, the illumination pattern is not uniform as in WF microscopy. The sample is excited with a periodic illumination pattern.

Being a wide-field method, the main advantage of SIM is that it can be significantly faster than conventional point-scanning microscopy techniques [6]. Nevertheless, in SIM one needs to acquire several frames for a single reconstruction, thus the speed of the method scales with the availability of fast camera technology. Amongst the super-resolution methods, SIM offers an excellent trade-off between lateral resolution, acquisition speed, axial resolution, need for specific staining agents and phototoxicity [3, 6].

To account for the patterned illumination, we can modify eq. 1.5 and describe the

imaging process with

$$I_{det,l} = (\rho \cdot I_{illu,l}) \otimes h + \mathcal{N} \ , \tag{1.11}$$

where $I_{det,l}$ is the l^{th} detected image, $I_{illu,l}$ is the l^{th} illumination pattern, and the other variables are the same as used in eq. 1.5.

As explained below, thanks to the periodic illumination, SIM has an effective OTF with extended support in the k_x, k_y plane and/or filled missing cone. These two features are at the core of the two branches of SIM methods.

The first branch of SIM deals with optical sectioning (OS-SIM) [19]. It typically uses incoherent light, thus the contrast of the sinusoidal modulation is high only near the focal plane of the objective. When shifting the grating laterally, the fluorophores that lie near this plane are illuminated by a modulated signal. However, the fluorophores that are away from the focal plane are homogeneously illuminated (see fig. 1.5). Optical sectioning can be achieved with a simple discrimination algorithm [1, 19, 20].

The other branch of SIM deals with high-resolution imaging using the Moiré effect to produce lateral resolution enhancement [15]. Improving axial resolution is also possible as explained below. This effect is based on the frequency mixing of the fine grating with the object (see fig. 1.6). It results in a down-modulation of the high-frequency components in the sample, shifting them into the support region of the OTF of the microscope [21]. Thereby, linear SIM can achieve a twofold lateral resolution enhancement compared with conventional WF microscopy (see fig. 1.8 and fig. 1.9).
This branch of SIM is sometimes referred to as SR-SIM, as opposed to the branch which emphasizes the optical sectioning, OS-SIM. In this work, the acronym SIM refers to SR-SIM.

A SIM system can be implemented by simply placing a fine grating in one of the image planes of a WF epifluorescence microscope. Thus, sinusoidal modulation of the light is produced in the sample space. If this illumination is produced by using a coherent laser beam of the correct polarization, almost perfect modulation

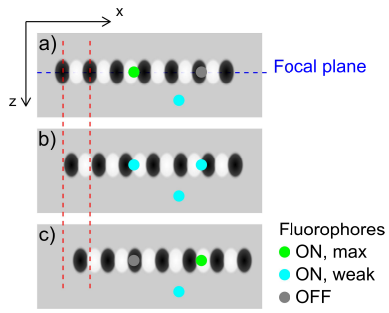

Figure 1.5.: An acquisition series in sectioning SIM shown on an XZ section through sample space. a) First time frame: The contrast of the grating is high only in the focal plane. The fluorophores that lie on a bright fringe are efficiently excited and emit light (green dots). Correspondingly, fluorophores that lie on a dark area do not emit any light (gray dot). Outside the focal plane, the illumination is homogeneous. The out-of-focus fluorophores can also be excited and emit light (cyan dot): the out-of-focus blur. b) Second time frame: The grating has been shifted by a third of a period. The out-of-focus fluorophores are illuminated with the same amount of light as in frame a. c) Third time frame: The grating has been shifted by another third of a period. The in-focus fluorophores experience an intensity modulation, whereas the out-of-focus fluorophores are homogeneously illuminated. They can thus be computationally removed.

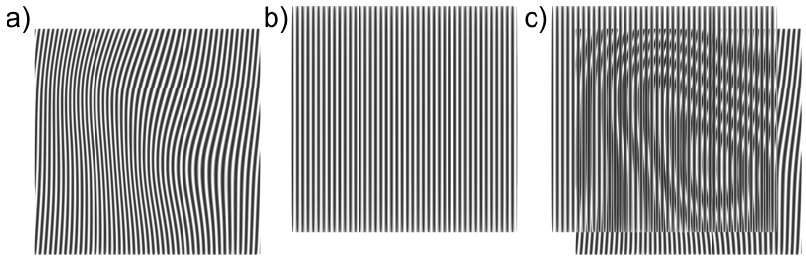

Figure 1.6.: Moiré effect. a) A simple object containing high frequencies. b) A grid of light. c) The overlap of a) and b) containing coarse Moiré fringes. The superposition of two periodic structures produces a down-modulation of the frequencies, *i.e.* two structures of high spatial frequency can generate a low spatial frequency in the overlap.

in the sample can be achieved up to the highest spatial frequency. The sinusoidal modulation of light is the result of two-beam or three-beam interference (see fig. 1.7b and c) in the sample. We refer to these methods respectively as two-beam SIM and three-beam SIM. For simplicity, we restrict ourselves for now to the two-beam SIM case. We describe the illumination pattern $I_{illu,l}$ (see eq. 1.11) as follows:

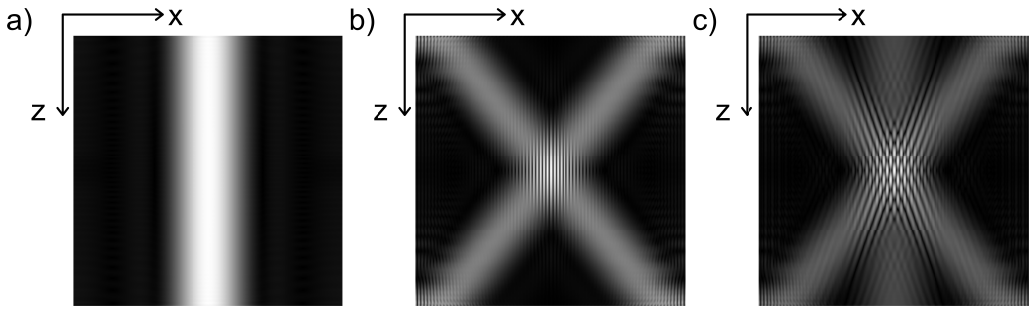

Figure 1.7.: Comparison of the illumination schemes in a) the WF microscope, b) the two-beam SIM microscope and c) the three-beam SIM microscope. The corresponding OTFs can be found in fig. 1.9.

$$I_{illu,l}(\mathbf{r}) = 1 + m_0 \cos\left(\mathbf{k_g r} + \theta_l\right) = 1 + \frac{m_0}{2}\left(e^{i(\mathbf{k_g r}+\theta_l)}\right) + e^{-i(\mathbf{k_g r}+\theta_l)}\Big), \tag{1.12}$$

where bold symbols are vectors, m_0 is the contrast (value between 0 and 1), $\mathbf{r}$ is the vector of spatial coordinates, $\mathbf{k_g}$ is the grating's k-vector and θ_l the phase (*i.e.* the position) of the l^{th} grating. The equivalent for the three-beam case can be found in appendix A.

The multiplication of the illumination pattern and the sample information in real space corresponds to a convolution of their Fourier transforms in Fourier space. In Fourier space, eq. 1.12 becomes:

$$\tilde{I}_{illu,l}(\mathbf{k}) = \delta(\mathbf{k}) + \frac{m_0}{2} e^{i\theta_l} \delta\left(\mathbf{k} - \mathbf{k_g}\right) + \frac{m_0}{2} e^{-i\theta_l} \delta\left(\mathbf{k} + \mathbf{k_g}\right) \tag{1.13}$$

The FT of a sinusoidal grating produced by the interference of two beams consists of three peaks, the intensity orders (shown in blue in fig. 1.8).

Eq. 1.11 becomes in Fourier space, neglecting the noise:

$$\tilde{I}_{det,l} = \left(\tilde{\rho} \otimes \tilde{I}_{illu,l}\right) \cdot \tilde{h}. \tag{1.14}$$

A visual interpretation of the convolution in eq. 1.14 can be seen in fig. 1.8: copies of the sample information are shifted to each of the three intensity orders.

Previously inaccessible sample information outside the detection OTF is thereby

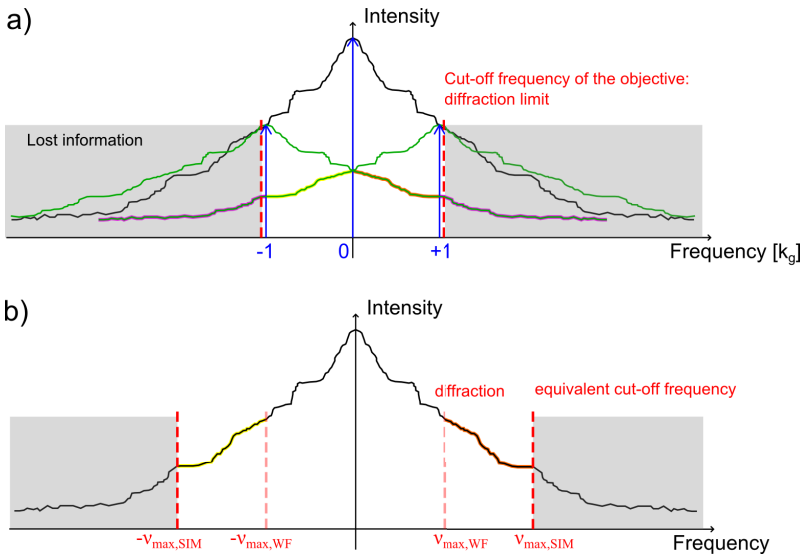

Figure 1.8.: Lateral resolution enhancement. a) Imaging model: The Fourier-transformed sample information (black) is convolved with the Fourier transformation of the illumination pattern (blue). This results in additional object components (green) at the position of the $\pm 1^{st}$ orders. Additional information lies within the support region of the detection optical transfer function (OTF) (yellow and orange). Some information is still lost (magenta). b) Image reconstruction: The equivalent cutoff frequency is twice as big that in the wide-field (WF) case. This figure does not show the decay of the OTF with frequency, only the cut-off outside its support region.

shifted into its support region, making it now accessible to optical imaging. A higher illumination spatial frequency of the excitation grating results in diffraction orders that are spaced further apart in the frequency space. Thus, even higher spatial frequencies of the Fourier-transformed sample information are shifted into the support region of the OTF. If the illumination is achieved through the objective, the highest possible illumination frequency will be close to the edge of the region of support of the OTF (see fig. 1.8). Linear SIM can thus typically achieve a twofold lateral resolution enhancement compared with conventional WF fluorescence microscopy.

As can be seen in between the red dashed lines in fig. 1.8a, we have several components - called orders - mixed in each detected image. These components are unknowns to be determined by the processing routine. In order to separate the components and reconstruct the high-resolution image, most approaches require the acquisition of as many raw images per direction as there are intensity orders [16, 22, 23]. This latter requirement can be weakened by exploiting the redundancies between

components [24, 25, 26], however in this work we did not utilize this idea. The shift of the illumination pattern is incremented of a l^{th} of a period. Experimentally this is realized by shifting a diffraction grating laterally through the beam. For each position of the grating, a new raw SIM image is acquired. The so-called phase step should be equal in between each acquisition, or equivalently the sum of all illumination patterns in one directions should be as close as possible to a homogeneous function for the separation to work as explain in more details in chapter 3.

As can be seen in fig. 1.9a, two-beam SIM broadens the OTF support by a factor two along k_x, k_y. Because it requires the acquisition of less raw images, two-beam SIM has a speed advantage with respect to three-beam SIM. However, it only partially fills the missing cone. This means, in terms of real space, that there is two-fold enhancement in the lateral resolution but only poor optical sectioning. On the other hand, three-beam SIM (see fig. 1.9d) features a two-fold widening of the OTF support in k_x, k_y, k_z, as well as a filled missing cone. Hence, three-beam SIM is an adequate method for 3D imaging. A maximum resolution enhancement is reached when the period of the excitation grid is just above the diffraction limit, which leads to the two-fold wider reconstructed OTF. As long as there is a single objective for illumination and detection, the period of the excitation grid itself cannot be below the excitation diffraction limit.

For applications where the biological problem can be solved by studying only a single slice, two-beam SIM is an interesting method because it enables to overcome many experimental problems due to its more simple experimental implementation and decreased acquisition time, thus leading to less drift or photobleaching issues. However, it can suffer from insufficient optical sectioning (see the missing cone present in fig. 1.9a).

It is nevertheless possible to achieve optical sectioning with two beams by using a slightly coarser grating so that the orders are not exactly at the limit of the OTF. This configuration does not use the full potential resolution but partially fills out the missing cone as a compromise (see fig. 1.9b) [1]. Another method consists of using slightly incoherent light, which produces a smearing of the orders (see fig. 1.9c). Two common methods to make a laser beam partially incoherent are by coupling it into a shaking multimode optical fibre [27] or by sending it through a rotating diffuser. At the output of such devices, the beam focuses into a homogeneous disk of

given diameter and has a certain divergence. The consequence of both methods is that the diffracted orders will not be diffraction-limited spots in the BFP any more, but wider areas. This is directly linked to the spatial incoherence. However, it also means a compromise in resolution because the centres of the diffractions orders will be further away from the border of the BFP. We built such a device and named it "fibre shaker". It is presented in chapter 4, in section 4.3.1.

Another attractive possibility to improve the optical sectioning of two-beam SIM is the total internal reflection (TIRF) mode [28, 29, 30, 31]. In TIRF microscopy, only the fluorophores that are directly on the coverslip get excited by an evanescent field. Since the other layers do not get excited, they also do not produce out-of-focus background.

Finally, the two-beam SIM dilemma between lateral resolution and optical sectioning can be solved by computational methods, either with the zero order suppression in the classical reconstruction method, as mentioned in section 3.1.1, or using the *thick slice* blind-SIM algorithm as presented in section 3.1.2 [32].

Short introduction to non-linear SIM. By using nonlinear properties of the dyes, like saturation of fluorescence emission under intense excitation, it is possible to achieve a resolution enhancement limited only by achieved nonlinearities and the noise [33, 34]. The emission does not depend linearly on the intensity but depends on a nonlinear function of the intensity, therefore the method is called non-linear SIM (NL-SIM). eq. 1.11 must be generalized and becomes

$$I_{det,l} = [\rho \cdot f\,(I_{illu,l})] \otimes h + \mathcal{N}\ , \tag{1.15}$$

where f describes the nonlinear emission response. This leads to the generation of higher harmonics inside the sample. There can theoretically be an infinite number of orders that add information by dragging it into the WF support region [33, 34, 30, 35, 31, 36]. In practice, there will be only a finite number of orders that are detectable above the noise level, which is what truly limits the reached resolution [33, 34].

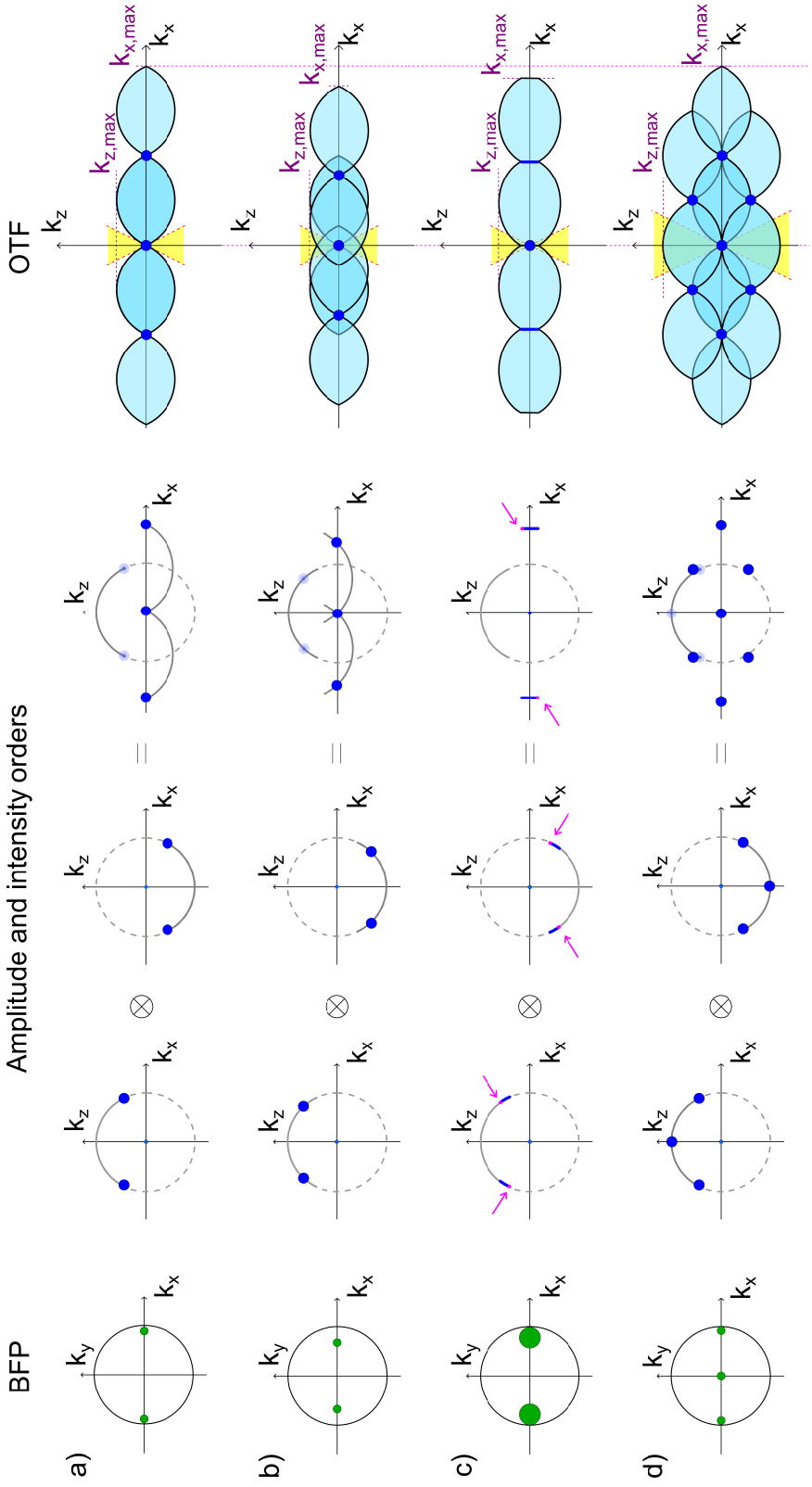

Figure 1.9.: OTFs in SIM (figure caption is continued on the following page).

Figure 1.9.: *Left column*: Diffracted orders in the objective's 2D coherent transfer function. *Middle column*: Corresponding 3D FT of the illumination. The light shadow-like blue dots are the amplitude orders left visible for understanding the construction process during the convolution operation. *Right column*: Corresponding final system OTFs. The FT of the illumination is convolved with the incoherent transfer function of the detection optical system. a) Two-beam SIM case. b) Two-beam SIM with a coarser grating. c) Two-beam SIM using partially incoherent light. The magenta points (emphasized by the magenta arrows) represent the pair of coherent components. d) Three-beam SIM case.

1.2.3. Basic implementation of the SIM technique

The key element of any SIM set-up is the generation of the patterned excitation. In the classical implementation, the sinusoidal modulation of light is the result of two-beam interference. As explained in section 1.2 and in [1], each excitation pattern $I_{illu,l}$ can typically be produced by a phase or amplitude grating acting as an illumination mask. The grating is illuminated by either collimated laser light (for optimum contrast) or incoherent light (for ease of use and sectioning). The grating produces three diffracted beams, which are focused in the BFP. There, the central spot can be blocked. The $\pm 1^{st}$ orders are then directed by a dichromatic reflector onto a microscope objective of high NA. The interference of the $\pm 1^{st}$ orders creates the excitation pattern that illuminates the sample (here corresponding to twice the periodicity of the original grating). The fluorescent light is collected by the same objective. The fluorescence emission passes through the dichromatic reflector and a clean-up detection filter, and is imaged by a tube lens onto a camera.
SIM requires several raw images to be processed into one final super-resolved image. However, each of the raw images contains the whole field of view, as opposed to point-scanning methods. Thus, SIM has an inherent speed advantage with respect to point-scanning methods. This advantage can be further exploited by making the SIM method even faster by novel excitation and detection approaches.
The use of a mechanical grating is, however, not always the preferred solution. It lacks flexibility because changing the period of the grid to adapt to a different wavelength requires changing the components. Moreover, the necessary grating translation and rotation are serious limitations to the speed of the system. Using opto-electronic instead of mechanic action is much faster. Therefore, the use of a spatial light modulator (SLM) is an attractive illumination tool for SIM [29]. The

SLM is a computer-driven opto-electronic device that enables faster changing of the grating position and orientation. SLMs are very useful devices in modern optics and find applications in many different fields.

One goal of the work described in thesis is to enhance the acquisition speed in SIM by using optical components that permit to simultaneously acquire a focal stack (see section 4.1) on the detection side and a fast SLM-based SIM scheme on the illumination side (see section 4.3).

1.2.4. Reconstruction approach in SIM

The reconstruction approach that was chronologically first developed [21, 22] and inspired several modulations and improvements of the same concept [37, 38] is referred to as the classical reconstruction approach and shortly described here.

First, a 2D FT is applied to each of the raw images. The phase shift applied to the illumination pattern allows to separate the three (respectively five) individual intensity orders from the three (respectively five) individual raw images. Once the orders are separated, a scaling factor followed by a shift is applied to them. The recombination of all shifted intensity orders is the effective OTF, to which an inverse Fourier Transform is applied to produce the final image. The good performance of each of these processing steps relies on the knowledge of experimental parameters: global phase and period of the illumination pattern, and more critically, phase shift. Some of the existing algorithms try and estimate these parameters from the data based on an iterative search in the cross-correlation of pre-separated orders [23].

If these experimental parameters are not well known or not controlled, the classical reconstruction algorithm will lead to artefacts, *i.e.* features in the result image that do not reflect the truth. It can be very hard to distinguish such artefacts from the real, desired, super-resolved features. The difficulty to distinguish artefacts from high resolution structures can lead to debates [39, 40]. It is therefore crucial to use a robust reconstruction method.
Experimental conditions can lead to a distortion of the illumination fringes. This is the case for example in strongly scattering samples, thick samples, or living samples which exhibit several refractive indices. In summary, the SIM reconstruction can fail because of

- a poor parameters estimation,
- distortions in the illumination pattern.

A method that solves these limitations and is able to reconstruct artefact-free SIM images irrespective of the illumination pattern therefore promises to extend the field of application of SIM. This is the motivation for developing the blind-SIM algorithm [41]. As presented in detail in chapter 3, we implemented our own version of the blind-SIM concept and brought some useful extensions to the method.

1.3. State of the art

1.3.1. Commercially available SIM systems

There are currently three commercial SIM systems which we here briefly present and compare in terms of acquisition speed. For clarity, we compare the time necessary to acquire a full sequence of 15 images for a size of the region of interest (ROI) of 512×512 pixels (thus leading to what we call the SIM imaging rate as opposed to the raw imaging rate) which is specified on the manufacturer's datasheet or product information document.
The Elyra S.1 (Carl Zeiss Microimaging, Germany) announces a minimal acquisition time of 1.4 s [42]. The N-SIM (Nikon, Japan) is slightly faster with a specified acquisition time of 1 s in the three-beam SIM mode [43]. Finally, the DeltaVision OMX (GE Healthcare, USA) is an impressive order of magnitude faster thanks to its galvo-scanning devices, with an acquisition time of 100 ms [44].

1.3.2. Existing open-source SIM software packages

In recent years, several toolboxes for SIM reconstruction were published and sometimes released in an open-source way. Here we give a short overview of the software packages.

For MATLAB (Mathworks, USA), there are two packages: OpenSIM [45] is only

for now only implemented for two-beam SIM and requires the image processing toolbox - not included in the basic package - from MATLAB. SIMtoolbox [46] has the advantages of distinguishing between several SIM modes, is available as a stand-alone MATLAB toolbox and is implemented also for three-beam SIM. However, despite our best efforts, the parameters estimation seems to be problematic.
Most interesting is the FairSIM software [47] which is a plugin for ImageJ [48] and Fiji [49]. FairSIM gives excellent results for both two-beam and three-beam SIM, but currently no 3D-reconstruction is implemented.

All these software packages are based on the classical Fourier-based approach which consists in separating the SIM orders, shifting and finally recombining them in Fourier space. A crucial preliminary step consists in estimating the illumination parameters, *i.e.* obtaining the orientation and period of the illumination pattern and obtaining the phase offsets (global and also pattern-individual). The parameter estimation step is in practice difficult. A first option consists in analysing the Fourier peak of the illumination pattern in the FT of the raw data [50]. However, this is not applicable to cases where the frequency of the illumination pattern is very high, *i.e.* where this peak is dampens by the WF OTF. Another approach uses the fact that the correctly separated orders contain overlapping information, and maximizes the cross-correlation of the pre-separated orders [22]. Phase estimation with the cross-correlation approach can be performed iteratively [23] or non-iterativaly [51].

2. Motivation of this thesis

2.1. Limitations due to reconstruction issues

One high resolution SIM image is reconstructed from several raw images by a complex algorithm (see section 1.2.4). Several approaches exist, as presented in section 1.3, most of them being based on what we refer to as the classical algorithm [21, 22] since it was initially used by the inventors of the technique and then applied for many years without major modifications.
However, these methods require knowledge of the illumination parameters. These experimental parameters are not always well known or controlled. They can be estimated from the data, but there are limitations as explained in section 1.2.4. In chapter 3, we present a novel reconstruction approach called blind-SIM which is able to deal with SIM data illuminated by unknown patterns. The strength of these approaches is that the requirements on the illumination pattern are drastically loosened, thus widening the field of application of SIM.

2.2. Speed limitation in 3D SIM

The illumination pattern is laterally shifted and rotated in between the acquisitions. The achievable imaging rate is limited by the hardware used

- on the excitation side, for the change of pattern - mechanical movement of a physical grating in the most simple but also slowest implementation -
- on the detection side, for the image acquisition, typically an electron-multiplying

charged coupled device (emCCD) or a scientific complementary metal-oxide-semiconductor (sCMOS) camera.

In the case of 3D imaging, the sample is typically mounted on a scanning stage and translated axially in order to image sequentially several planes of interest. Here another dimension is added to the speed limitation, due to the inherently slow mechanical scanning in z of the probe.

The biological community shows a vivid and growing interest for live-cell study and hence instruments with comparatively faster imaging capabilities are very attractive. The development of new SIM techniques is therefore motivated not only by further lateral resolution enhancement but also an enhanced temporal resolution. SIM imaging has been demonstrated in live mode [27, 52, 53, 54], however for 3D imaging axial mechanical scanning is typically required. In chapter 4, we present a novel experimental SIM set-up which enables instantaneous acquisition of a SIM focal stack without z-scanning. This so-called multifocus-SIM (MF-SIM) method paves the way for a significant improvement of the temporal resolution in 3D-SIM imaging.

3. Blind-SIM: a novel reconstruction method

Parts of this chapter including figures have been published in [32]:

1. Section 3.1.2, except for figs. 3.1 - 3.5 and the text referring to these figures, especially the discussion related to fig. 3.5;
2. Section 3.2 (figs. 3.6 – 3.8 were only slightly modified);
3. The two first and the fourth paragraphs of section 3.4.

3.1. Presentation of the blind-SIM approach

3.1.1. 2D Blind-SIM

As presented in section 1.2.4, the classical approach to SIM reconstruction is prone to artefacts in certain cases, which motivates the development of the blind-SIM algorithm [41].
The idea is to reconstruct the unknown illumination pattern I_{illu} along with the sample information ρ. If the algorithm does not require any prior knowledge of I_{illu}, then it can be anything: a sinusoidal pattern of unknown period and phase, distorted fringes, or even random speckles. This is achieved by a blind deconvolution approach.

The first version of the blind-SIM algorithm [41] demonstrated SIM using random

speckle illumination patterns. However, in the case of conventional SIM illumination, it is possible to have at least a partial knowledge of the illumination pattern [55]. As explained in next section 3.1.2, this information can be used in the form of a Fourier mask.

However, to this point the blind-SIM algorithm was only applicable to ultra-thin samples. Indeed, the out-of-focus blur stemming from out-of-focus structures in thick samples is captured in the SIM data and reduces the ability of blind-SIM to reconstruct the illumination pattern with satisfactory contrast. Furthermore, there is a conceptual dilemma in two-beam SIM between optimal lateral resolution enhancement - requiring fine grating - and optical sectioning - requiring coarser grating. *Thick slice* blind-SIM was developed in order to solve this dilemma [32] and is detailed in next section 3.1.2.

It should be noted that the Fourier-based, so-called "classical", approaches to SIM reconstruction can also achieve optical sectioning. Before recombining the previously separated and shifted orders, the 2D OTF is re-weighted in such a way that the different orders do not contribute around their missing cone: this is called "zero order suppression" [23, 56, 57].

3.1.2. Thick slice Blind-SIM

We developed a reconstruction algorithm, hereafter named *thick slice* blind-SIM, capable of processing SIM *single slice* data acquired in *thick* samples. Our approach is inspired by the recently developed deconvolution-based reconstruction method called blind-SIM in which the illumination pattern is reconstructed along with the object [41, 58]. Since blind-SIM does not require the knowledge of the illumination pattern, it is more robust to experimental imprecision and possible sample-induced distortion than classical SIM reconstruction approaches, while maintaining high resolution and tight optical sectioning abilities. Up to now, blind-SIM has been developed in a strict two-dimensional framework only compatible with very thin samples. Any out-of-focus contribution caused the algorithm to fail. The main idea of *thick slice* blind-SIM is to process the 2D data with an alternate 3D deconvolution over the sample and illuminations but accounting for incomplete measured data, thus having the ability to reject the out-of-focus blur.

Principle of blind-SIM. The imaging process in a SIM microscope can be described by eq. 1.11. In eq. 1.11, ρ describes the biological reality - the fluorophore density -, whereas the variable denoted $\widehat{\rho}$ in eq. 3.1 below is an estimate of this reality. The blind-SIM algorithm described below reconstructs both the sample information $\widehat{\rho}$ and the collection of gratings $\{\widehat{I}_{illu,l}\}_{l=1..L}$. Here, $L = 9$ since we assume 3 lateral shifts of the grating in each of the 3 directions. The reconstruction is done by minimizing the functional

$$F(\widehat{\rho}, \widehat{I}_{illu,l}) = \sum_{l=1}^{L} \| \left[\widehat{\rho} \cdot \widehat{I}_{illu,l}\right] \otimes h - I_{det,l}\|^2. \tag{3.1}$$

More precisely, the algorithm estimates values of the object $\widehat{\rho}$ and the gratings $\{\widehat{I}_{illu,l}\}$, projects these estimates according to the model (eq. 1.11) to calculate the predicted image, and then evaluates the quality of this prediction by calculating the least square error to the measured image $I_{det,l}$. Contrary to the blind-SIM algorithm presented in [41], our algorithm is based on an update scheme that alternates between object and illumination updates, $\widehat{\rho}$ and $\{\widehat{I}_{illu,l}\}$. Similar schemes are common [59, 60]. This choice was made to keep the mathematics and the code simple and fast. Each iteration i contains an object estimation sub-iteration, in which $\{\widehat{I}_{illu,l}\}$ is fixed and equal to its most recent estimate. $\widehat{\rho}$ is thus updated and subsequently fixed for the illumination estimation sub-iterations, in which $\{\widehat{I}_{illu,l}\}$ is optimized. The object is estimated for m iterations and the illumination pattern is estimated for n iterations. It should be noted that the optimizer might have not yet reached a minimum within these m or n iterations. This procedure is repeated for $i = 1..N$ cycles.

1. Initial values: $\widehat{\rho}_0$ and $\{\widehat{I}_{illu,l}\}_0$ homogeneous

2. Cycle i - object m estimation steps by approaching the zero by using the gradient of F:
   $\frac{\partial F\left(\widehat{\rho},\{\widehat{I}_{illu,l}\}\right)}{\partial \widehat{\rho}}$ for $\{\widehat{I}_{illu,l}\} = \{\widehat{I}_{illu,l}\}_{i-1}$ fixed (m iterations)

3. Cycle i - grating n estimation steps by approaching the zero by using the gradient of F:
   $\frac{\partial F\left(\widehat{\rho},\{\widehat{I}_{illu,l}\}\right)}{\partial \widehat{I}_{illu,l}}$ for $\widehat{\rho} = \widehat{\rho}_i$ from previous step and fixed (n iterations)

4. End of cycle i: estimated values of $\widehat{\rho}$ and $\{\widehat{I}_{illu,l}\}$ updated.

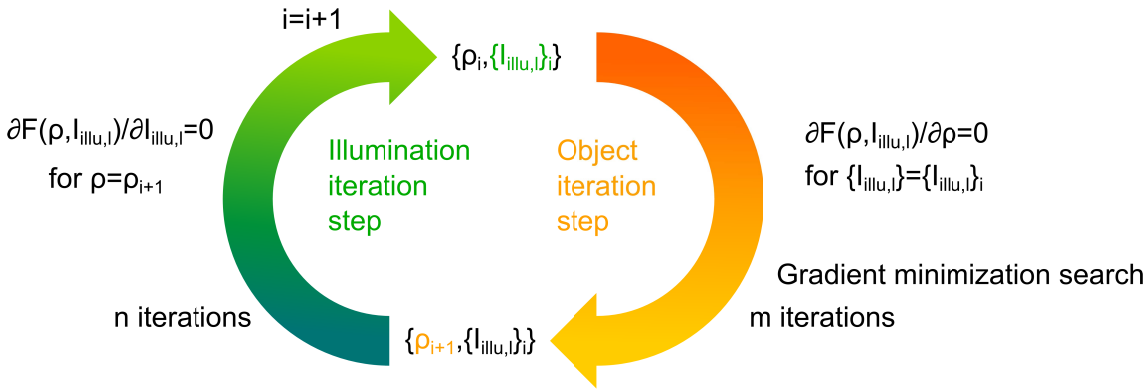

Figure 3.1.: Schematic view of the alternate blind-SIM approach. We removed the $\hat{\cdot}$ to make the figure easier to read, but all ρ and $\{I_{illu,l}\}$ are estimates.

5. Go to step 2 and repeat for cycle $i+1$ until $i = N$

An illustration of the alternate blind-SIM algorithm is presented in fig. 3.1.

In practice, we found that $m = 5$ for the first cycle $i = 1$, $m = 25$ henceforth and $n = 5$ yield good results. The toolbox was implemented in MATLAB R2012a and the gradient-based optimization process uses the *minFunc* function developed by Mark Schmidt and freely downloadable from [61]. The descent direction and step length is computed using LBFGS, which is a quasi-Newton limited memory BFGS search direction method [62]. The line search strategy, which determines the step length, is based on the strong Wolfe condition (with a cubic interpolation strategy). The initial step size is the minimum between 1 and twice the previous step length. For the special case of assuming Gaussian noise of constant variance (as used in this manuscript), we can also compute the residual in Fourier space, thus avoiding two Fourier transformations per iteration cycle.

The novelty of our *thick slice* implementation is that, even though 2D data were acquired, a 3D deconvolution is performed. The algorithm calculates with a full three-dimensional volume of P focal slices, but in the comparison step between the 3D data predicted from the 3D guess and the 2D measured data, only the central slice is computed and all other comparison values are simply set to zero at this step. The whole stack is then propagated back from measurement space into object space as typically done for gradient-based maximum-likelihood methods [63]. The algorithm minimizes eq. 3.1, with h being the 3D PSF. We therefore perform a three dimensional deconvolution and the object estimates are three dimensional

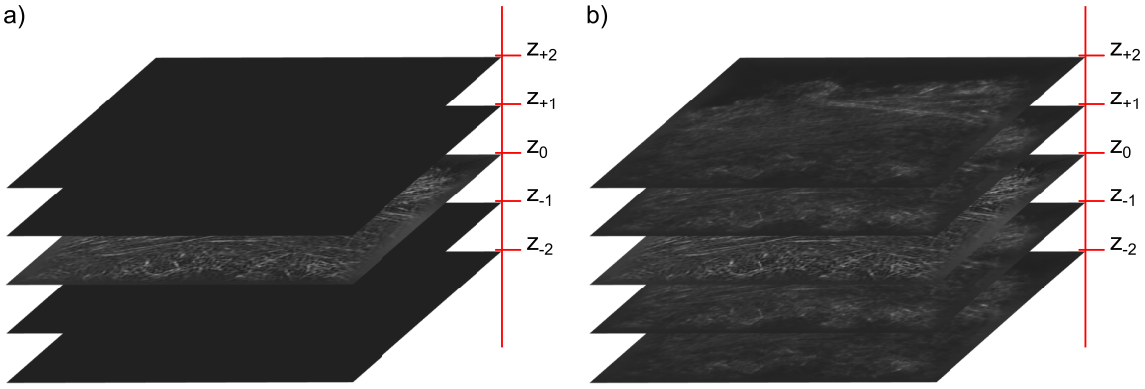

Figure 3.2.: Thick slice reconstruction. Here $P = 5$ for the sake of demonstration. a) Initial 3D sample estimate. The 2D acquired data is placed in the middle slice z_0, the other slices are empty (value of all pixels is 0). b) The result of the thick slice reconstruction is a stack in which each slice contains information.

despite the data being two-dimensional in nature. Due to the axial extent of the PSF, information — the out-of-focus contribution present in the focal slice — will propagate to and accumulate in the extra planes during the deconvolution process and the initially empty planes in 3D sample estimate are filled (see fig. 3.2). The error is calculated as described above in the middle slice only, without other planes contributing. Thus, the algorithm is free to place any information into these extra planes with the goal to decrease the error in the middle plane. The user can choose the number of reconstructed planes P according to the sampling of the discretized PSF, denoted scZ in table 3.1. P should be large enough to enable out-of-focus contribution to be efficiently rejected. However, increasing it further unnecessarily increases the computation time.

Using an unaberrated PSF which is double-sided leads to identical information content on both sides of the middle plane (see fig. 3.3a). To increase the computational efficiency, we use only a half-sided PSF to make use of this z-symmetry. In practice, we simply neglect the upper half of the PSF and replace this part of the PSF with the cyclic extension of the lower part of the PSF. In other words, we use only the lower part of a PSF of double size but place the focus cyclically at the middle plane (see fig. 3.3). We can thus prevent the redundancy on both sides of the middle plane. This gives an identical result as a “normal” double-sided PSF, but saves a factor of almost two in both computation time and memory. Finally, another symmetry that can be exploited is the real-valuedness of the object and measured data: a factor of

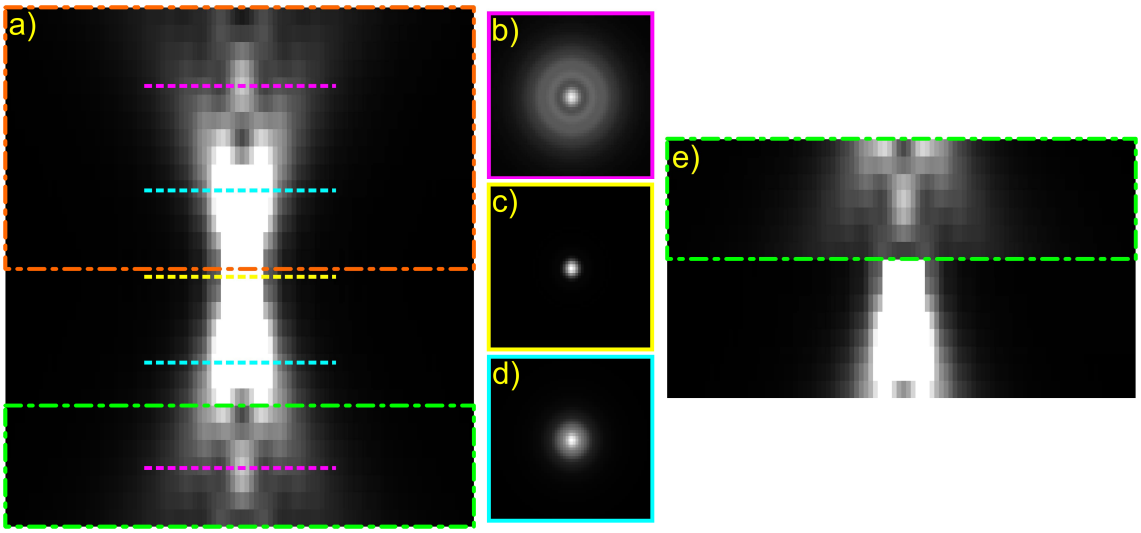

Figure 3.3.: Half-sided PSF. In all sub-images (except for c), the display range was manually adjusted for better visibility of all calculated planes. a) $x-z$ view of an unaberrated PSF calculated for $2P$ slices. b-d) Example $x-y$ views of three different focal planes of the PSF displayed in a). The respective z positions are indicated by the coloured dashed lines. c) Focal spot *i.e.* view for $z = z_0$ where z_0 is the nominal focal plane (yellow). Linear display. d) View for $z = z_0 \pm 5$ slices (cyan). b) View for $z = z_0 \pm 11$ slices (magenta). In the absence of aberrations, the information is symmetric on both sides of the nominal focal plane: b) displays the $x-y$ view both for slice number $z = z_0 + 11$ and for slice number $z = z_0 - 11$ e) Making use of this symmetry, we create the half-sided PSF. We ignore the lower half (orange dot-dashed box) and shift the lowest quarter (green dot-dashed) above the focal plane. The resulting half-sided PSF has therefore the same information content as a) but with twice less slices, reducing the computational cost.

two in speed is gained by using the half complex space Fourier Transform (RFT). A GPU (NVIDIA GeForce GTX 690) was used to speed up the processing (25 min vs. 330 min without GPU for processing fig. 3.8d). Our computer has 8 processors (Intel Core (TM) i7 - 3770 CPU @3.40 GHz) and 32 GB memory.

Further regularization and constraints were introduced to make the algorithm more robust. First, we apply a condition stating that the sum of each triplet of gratings (for each direction) is uniform. Thus, we estimate only two (resp. $J-1$ if J is the number of illumination patterns per direction) out of every three (resp. J) unknown illumination patterns and obtain the remaining ones using this sum condition. This reduces the number of unknowns of the system [41]. This condition should be fulfilled experimentally for a typical situation where relative pattern shifts

Table 3.1.: **Reconstruction parameters**

Fig.#	P	scZ nm	σ	N	Reg. type	λ
3.6b	1	N.A.	14	40	N.A.	N.A.
3.6c	1	N.A.	N.A.	100	GS	$1 \cdot 10^{-2}$
3.7b	1	N.A.	N.A.	100	GS	$1 \cdot 10^{-2}$
3.7c	9	200	N.A.	100	GS	$1 \cdot 10^{-3}$
3.7e	1	N.A.	5	50	GS	$7 \cdot 10^{-1}$
3.7f	9	200	3	100	GR	5
3.7i	9	200	13	100	GR	20
3.8a	1	N.A.	N.A.	100	GS	$1 \cdot 10^{-3}$
3.8b	1	N.A.	6	50	GR	$2 \cdot 10^{3}$
3.8c	30	91	N.A.	100	GS	$1 \cdot 10^{-5}$
3.8d	13	91	6	100	GR	20

For each blind-SIM reconstruction, a number of parameters can be tuned. In this table, we summarize the chosen parameters for the presented results. The number of planes corresponds to the number of planes in a double-sided PSF. Using a half-sided PSF, this value is divided by two as the PSF contains each plane only once.

are well controlled, but aberrations still being present, deforming the images of all patterns. The phase steps applied to a sinusoidal grating should be equal. In the appendix B, we present a detailed discussion concerning aberrations and show that the sum condition is still fulfilled even if the interfering wavefronts are aberrated.
Second, neither the reconstructed object nor the illumination should contain negative values since we are in the framework of fluorescence imaging. The non-negativity of the solution could be applied in the form of a penalty term [63], but we found that intrinsic positivity as in [41] for the sample estimate yielded nicer results.
We therefore wrote $\widehat{\rho}$ as the square of an auxiliary function ξ:

$$\widehat{\rho} = \xi^2. \tag{3.2}$$

As commonly done for this class of problems which are typically ill posed, we introduced a regularization term. For smoothness constraints, Good's Roughness (GR), gradient square (GS) or the hyperbolic Total Variation (hTV) regularization functions were applied [64, 65]. The regularization term is added to the error with a weight λ in the object estimation step. Practically, we tuned the type and λ of the regularization for each sample. The choice has to be made as a compromise

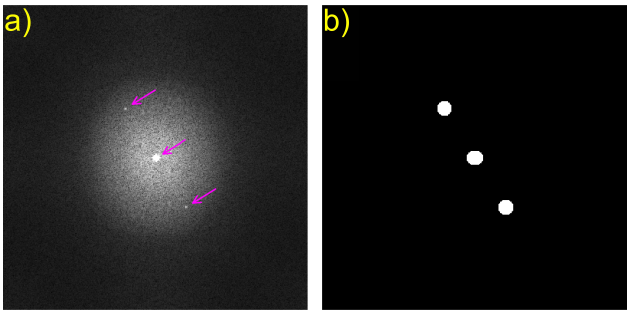

Figure 3.4.: Example of a Fourier mask used by the blind-SIM algorithm during the illumination iteration step. For this example, we have two-beam SIM data reconstruction with the 2D blind-SIM algorithm. In a first step, we reconstruct without using any mask. a) FT of one of the estimated illumination pattern (one direction, one phase) $\widehat{I}_{illu,1}$. For better visibility, we display $abs\left(FT\left(\widehat{I}_{illu,1}\right)\right)^{0.3}$ and we lower the upper bound of the display range. The magenta arrows point at the SIM peaks. b) Mask calculated from a). Black: boolean zero (false), white: boolean one (true). The algorithm only searches for solutions in the mask (true regions).

between resolution and smoothness of the result. No regularization was applied to the illumination function. In [41], no regularization term was applied, but the iterations were stopped at a user-defined number to prevent over-deconvolution artefacts.

Furthermore, *partial* knowledge of the grating, if available, can be used by using an illumination mask in Fourier space. A round kernel of radius σ is placed at the expected positions of the peaks of the FT of the grating. In the illumination iteration step, the algorithm searches for solutions exclusively inside of this Fourier mask. This constraint makes the algorithm more robust, *e.g.* the high frequencies are reconstructed with better contrast, while accounting for potential experimental imprecisions. For instance, the grating period may be slightly different than in theory, or the fringes may be distorted, and yet the grating will still be reconstructed [55].

An example of such a binary mask used for 2D blind-SIM reconstruction and two-beam SIM case in one of the grating orientations is given in fig. 3.4. There will therefore be one mask for each grating orientation. If three-beam SIM data is treated with a 2D blind-SIM algorithm, there will be another pair of discs in the mask at the corresponding half frequency.
If two-beam SIM data is treated with *thick slice* blind-SIM, the same mask is placed in the focal slice and the mask for the extra planes is set to zero everywhere. In the case where *thick slice* blind-SIM is applied to three-beam SIM data, the mask for the

$\pm 1^{st}$ orders - corresponding to the coarse grating frequency - should be adequately shifted in the z dimension of the Fourier space of an amount $k_{z,height}$ calculated as shown below and in fig. 3.5:

$$k_{z,height} = k_{max,z} \cdot \left(1 - \sqrt{1 - \langle \boldsymbol{k_{0,normed}}, \boldsymbol{k_{0,normed}} \rangle}\right), \tag{3.3}$$

where $\langle \cdot, \cdot \rangle$ symbolizes the scalar product. $k_{max,z}$ and $\boldsymbol{k_{0,normed}}$ are defined as:

$$k_{max,z} = \frac{P \cdot scZ \cdot \mathrm{NA}}{\lambda_{em}} \tag{3.4}$$

and

$$\boldsymbol{k_{0,normed}} = \frac{\boldsymbol{k_0}}{k_{max}}, \tag{3.5}$$

with $\boldsymbol{k_0}$ the k-vector of the coarse grating *i.e.* $\boldsymbol{k_0} = {}^{\boldsymbol{k_g}}/_2$ with $\boldsymbol{k_g}$ as defined in eq. 1.12.

k_{max} is the Abbe limit expressed in number of pixels and in Fourier space, defined as

$$k_{max} = \frac{s_x \cdot scX \cdot 2\mathrm{NA}}{\lambda_{em}}, \tag{3.6}$$

where s_x is the size of the image in x, y in number of pixels (assuming a square field of view) and scX is the size of the pixels in the sample space in x, y.

Interestingly, this procedure corresponds in spirit to a single slice from a stack as acquired with the multifocus SIM approach described in chapter 4 as well as to a single slice from a 3D scanning SIM stack.

In practice, the proposed method requires *a priori* known input parameters (*e.g.* the approximate grating constant) and tunable parameters such as the choice of regularization method and its weighting factor. This has the disadvantage of introducing subjectivity, but also constraints the solution to a more reasonable result, which is also of practical importance. In table 3.1, we state the reconstruction parameters used for each figure. We were so far unable to provide a proof of convexity of our alternating approach. However, we observed a fast convergence to useful results in all cases with the parameters set as given in table 3.1.

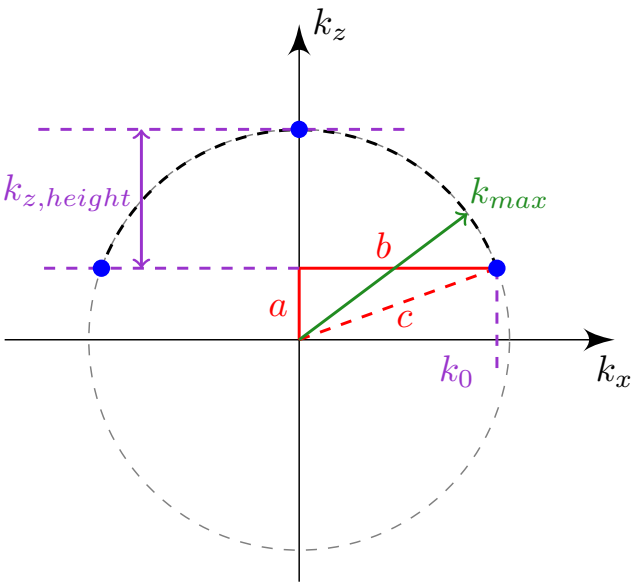

Figure 3.5.: Schematic representation for the $k_{z,height}$ calculation. Blue: SIM amplitude orders. The k-vectors are normalized with respect to k_{max}, *i.e.* $c = 1$ and $b = k_{0,normed}$. In normalized frequency, $k_{z,height} = 1 - a$ and a is found by applying the Pythagoras theorem in the red triangle.

3.2. Testing the performance of blind-SIM

Proof-of-principle. First, we demonstrate that the results obtained with the *alternate* estimation method are quite comparable to that obtained with the previously published blind-SIM algorithm [55]. In fig. 3.6, we compare both approaches on an ultra-thin paxillin labelled cell illuminated with a distorted grating. We applied the previously published [55] 2D blind-SIM approach (fig. 3.6a). As seen from fig. 3.6, both our deconvolution (fig. 3.6b) and the previously published result (fig. 3.6a) [55] show a roughly similar information content, especially when compared to the deconvolved WF image (fig. 3.6c). There are visible differences especially in the amount of thread-like appearances connecting the dot-like patterns. As we lack the underlying ground-truth information, we are unable to decide which of the reconstruction result is closer to reality.

Next to the joint optimization scheme, a further difference to our implementation is that, in [55], the authors did not use any regularization, but instead tuned by hand the number of iterations to stop the minimization before noise start to be amplified. Our maximum a posteriori likelihood (MAP) approach is a bit different.

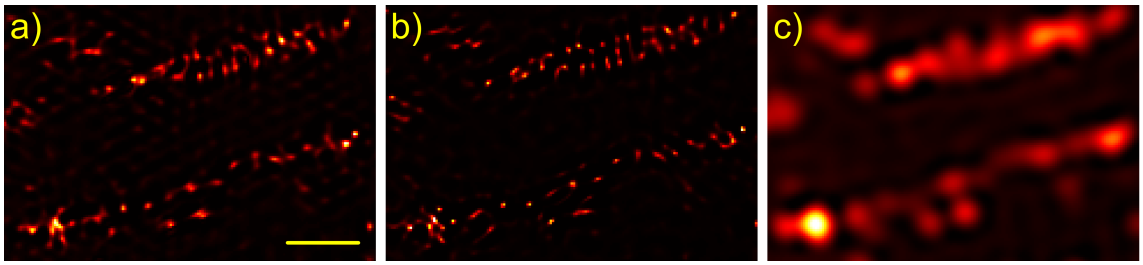

Figure 3.6.: Comparison of the different existing 2D blind-SIM algorithms on a paxillin sample illuminated with a distorted grating. a) 2D blind-SIM using simultaneous estimation of the object and illumination patterns [55]. b) 2D blind-SIM using the proposed method with alternating estimation. For improved comparability, a conjugate gradient update scheme was used here (the type and weight of the regularization are given in table 3.1). c) 2D WF deconvolution. The scale bar is 1 µm.

3.2.1. Simulated samples

Simulations. In order to test our *thick slice* blind-SIM algorithm, we used a simulated object consisting of several practical resolution test targets (fig. 3.7a) [23]. We introduced out-of-focus information by placing a $\pi/2$-rotated version of the same object 800 nm displaced along the axial direction. Two-beam illumination was simulated by multiplying this object with a grating of 214 nm period, that was positioned three times by $2\pi/3$ in the 0°, 60° and 120° orientations in the plane. Poisson noise was introduced in the data so that the expected value of the brightest pixel in the sum of all images corresponds to a count of $4 \cdot 10^5$ photons. The data were then convolved by a 3D PSF, simulating imaging through a microscope objective of NA 1.3 at an emission wavelength of 500 nm. The total object was 512×512×9 voxels, with a square voxel size of 25 nm × 25 nm × 200 nm.

Out of this 3D stack, only the focal plane data was selected ("measured" in the simulation). One of the 9 images with visible out-of-focus contributions is depicted in fig. 3.7d. The WF images for comparison were obtained by summing all individual raw SIM images. First, the 2D blind-SIM algorithm was applied to the single-slice data (fig. 3.7e). We observe that the out-of-focus blur is still present. We then applied the *thick slice* blind-SIM algorithm with the reconstruction parameters as presented in table 3.1. The middle plane of the *thick slice* result (fig. 3.7f) contains no out-of-focus light. The comparison of fig. 3.7e with the 2D WF deconvolution (fig. 3.7b)

and of fig. 3.7f with the 3D WF deconvolution, here using the entire simulated stack data rather than just the single slice data (fig. 3.7c), demonstrates the resolution enhancement. We also studied the case where the illumination was distorted as shown in fig. 3.7g. *Thick slice* blind-SIM reconstructed an object (fig. 3.7i) which is, except for a slight loss in the sectioning ability, still quite similar to that obtained in the non-distorted case (fig. 3.7f), as well as the illumination function (fig. 3.7h). By comparing the simulated illuminated pattern (fig. 3.7g) and its reconstruction (fig. 3.7h), one can observe three things: first, blind-SIM can only reconstruct the illumination pattern well for the regions in the field where there is information, *i.e.* where the sample emits photons. In such a simulated sample, there are dark regions where the illumination pattern cannot be retrieved reliably, hence the low contrast regions (magenta arrows) in fig. 3.7h. Second, the reconstructed frequency is correct, which means that the final resolution is optimal. Not only the frequency but also the phase distortions should be retrieved for a successful and correct reconstruction. In fig. 3.7h, we see that the applied phase jump, particularly on the right side of the image, was correctly recovered.

In addition to this resolution slide simulation, we tested several other simulated objects - including hollow spheres - which confirmed the optical sectioning ability of *thick slice* blind-SIM. For instance, if we place a single point in an out-of-focus and no information in the focal place, we manage to not only completely reject its light contribution but also to reconstruct it down to a single point in an out-of-focus plane.

3.2.2. Real thick samples recorded with the Elyra

Experimental validation. The commercially available ELYRA-S.1 (Carl Zeiss Microimaging, Germany) was used to produce the experimental data whose reconstructions are shown in this section. It is a 3D SIM system, *i.e.* three plane waves are interfering in sample space to produce the illumination modulation. A 3D set of data was available, which permitted us to compare with the 3D deconvolved WF image. The acquisition parameters were: NA 1.4, voxel size 79 nm, distance between the acquired planes 91 nm, excitation wavelength 488 nm and coarse grating period 440 nm. The sample was prepared by growing MCF-7 breast cancer cells on the coverslip with following fixation and staining of actin with "Alexa Fluor® 488

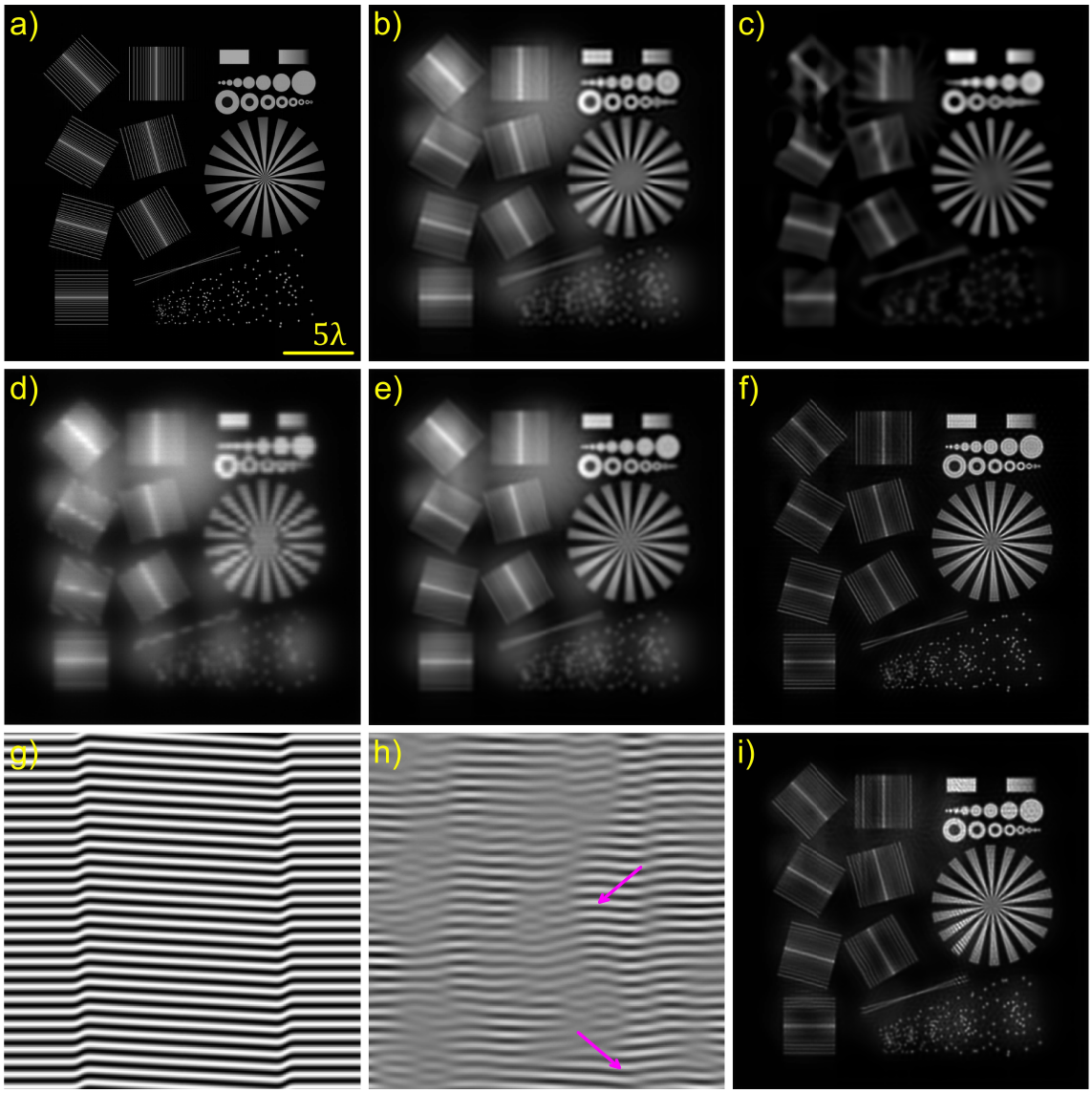

Figure 3.7.: Results of 3D simulations with *thick slice* reconstruction. a) Resolution test target placed in the focal plane of our simulated sample. 800 nm out-of-focus was a $\pi/2$-rotated version of the same structure. b) 2D WF deconvolution. c) Focal slice of 3D WF deconvolution of the entire WF image stack. d) One of the 9 simulated SIM images. Here we simulate a two-beam SIM. e)2D blind reconstruction of d) containing out-of-focus light. f) *Thick slice* blind-SIM result, showing optical sectioning and high resolution. g-i) Simulation as in a-f) but with a distorted illumination pattern as depicted in g) (zoom). h) Reconstructed illumination function. The magenta arrows point at regions where the reconstructed pattern has a low contrast, corresponding to dark regions of the sample. (i) *Thick slice* blind-SIM reconstruction of the object described in a) but illuminated with the distorted pattern g). The scale bar is 2.5 µm.

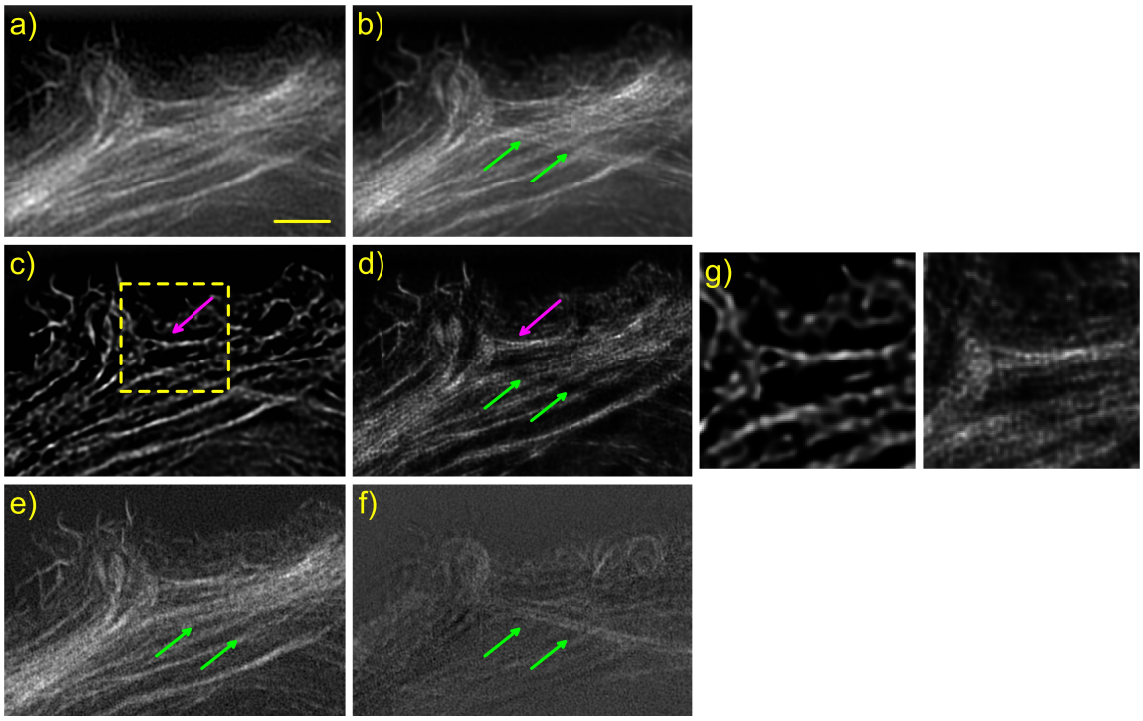

Figure 3.8.: Experimental results in a real thick sample. a) 2D WF deconvolution. b) 2D blind-SIM reconstruction with higher resolution but no optical sectioning. c) 3D WF deconvolution. d) *Thick slice* blind-SIM result. The resolution is improved and the out-of-focus contribution removed. The green arrows indicate a pair of filaments that is removed because it originally stems from another plane. e) and f) are the reconstructions of the original 3D data with the ZEN software (version 2010D). e) Plane that was selected. f) Two slices under slice e), *i.e.* 182 nm away. The scale bar is 2 µm. g) Zoom in the region represented by the dashed yellow box in c) and corresponding region in d).

Phalloidin", emitting at 550 nm.

We selected a 200×200 pixels region of interest in a given plane and performed 2D and *thick slice* blind-SIM reconstructions (resp. fig. 3.8b and d). The reconstruction parameters can be found in table 3.1. In addition, we perform 2D and 3D WF deconvolutions (respectively fig. 3.8a and c).
Comparing the blind-SIM results with the WF deconvolutions demonstrates the resolution enhancement due to the structured illumination. The magenta arrows indicate two filaments that appear to be merged in the WF images but are separated in the blind-SIM results. 2D blind-SIM cannot account for out-of-focus fluorescence,

leading to residual patterning in the background of fig. 3.8b. We observe another striking difference between 2D and *thick slice* blind-SIM, indicated by the green arrows. In fig. 3.8d, the indicated pair of filaments is removed, while being present in fig. 3.8b. It seems that these fibres did not preside precisely in the selected plane. The part which is close to the left arrow is located about 200 nm out-of-focus. We could verify this information thanks to the 3D reconstruction using the entire 3D datastack calculated with the ZEN software - same approach as PEM and available together with the Elyra system -. In these images, the filaments are also not visible in the focal plane (fig. 3.8e) but in focus in another plane located 182 nm away (fig. 3.8f).
In this case, the blind-SIM algorithm did not significantly improve the quality of the reconstructions as compared to the commercial software because the illumination was not distorted. We use this data as proof-of-principle to demonstrate that *thick slice* blind-SIM has the expected resolution enhancement and optical sectioning by processing only a single slice.

3.3. Comparison of the performance

In order to confirm the previously described working principle, we compare blind-SIM with respect to the classical Fourier-based SIM reconstruction algorithm, referred to as PEM, which stands for Patterned Excitation Microscopy [37, 38].

Performance on a 2D simulated object and SIM dataset. First, we apply 2D blind-SIM on the object depicted in fig. 3.9a (see fig. 3.9), both for the cases of perfect fringes (fig. 3.9d) and distorted fringes (fig. 3.9f). Both results are very similar, demonstrating the robustness of blind-SIM against distortions in the illumination pattern. Applying PEM to the same datasets reveals first that, in the case of perfect illumination, there is no qualitative difference between blind-SIM (fig. 3.9d) and PEM (fig. 3.9c), confirming that the attained resolution with blind-SIM is not an artefact. On the other hand, the PEM result on the distorted SIM data reveals artefacts (fig. 3.9e), for instance an artificial doubling of some features. This confirms the superiority of the blind-SIM reconstruction for this very simple simulated sample. This result was tested without appreciable change by introducing different levels of noise.

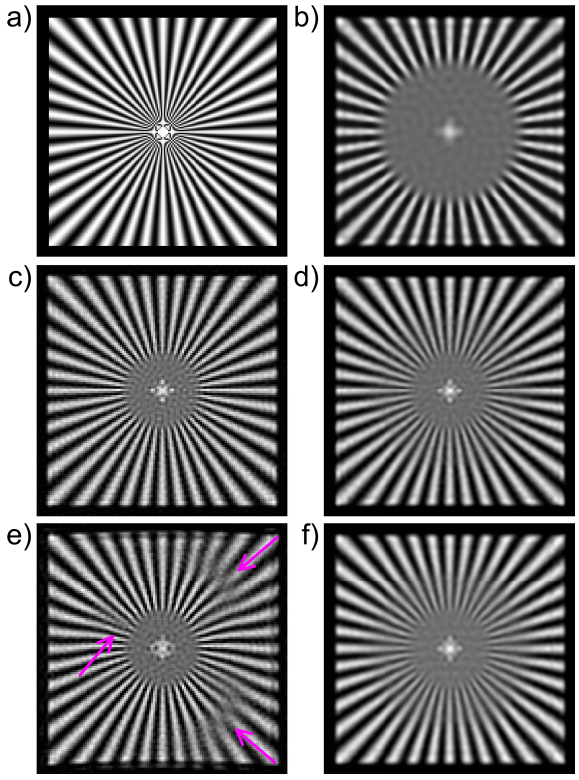

Figure 3.9.: Performance of PEM and of blind-SIM in the case of 2D SIM. a) Object used for these simulations. b) 2D WF deconvolution of the average of all nine individual raw SIM images. The calculated illumination pattern was either ideal (c and d) or distorted (e and f).(c) and e) display the PEM reconstructions, d) and f) the blind-SIM results. The magenta arrows point towards reconstruction artefacts. The star-like feature in the middle of all images comes from an aliasing issue already present in the simulated object but is of no consequence.

The performance in the case of real thick samples can be assessed by having a closer look at the data already presented in fig. 3.8. We compare *thick slice* blind-SIM with ZEN. By comparing the results of ZEN and *thick slice* blind-SIM in the focal slice z_0 (fig. 3.10a and b respectively), we see that the middle slice of the *thick slice* blind-SIM result stack (see fig. 3.2) contains the same information as the ZEN slice, albeit with better contrast. The same fine resolution features are visible, which confirms that *thick slice* blind-SIM does not produce artefacts. In fig. 3.10d, we display another slice z_2 of the *thick slice* blind-SIM result stack, with $z_2 = z_0 + 182\,\text{nm}$. Fig. 3.10c also corresponds to z_2. The major difference is that fig. 3.10c was obtained by processing of a 3D SIM stack with ZEN whereas fig. 3.10d is the result of a single slice processing using *thick slice* blind-SIM. We can therefore

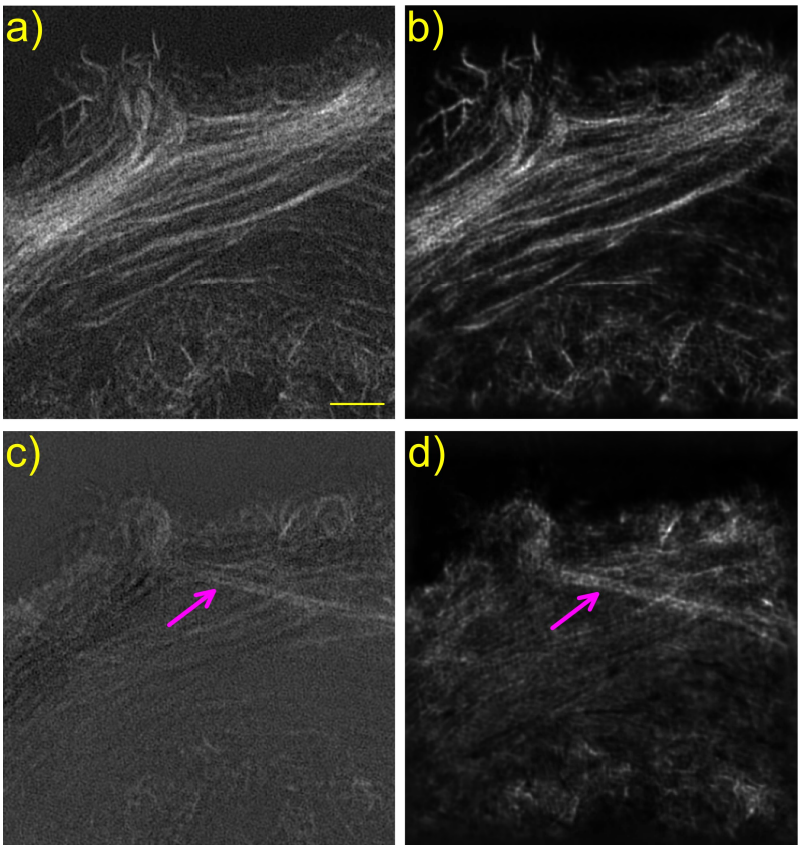

Figure 3.10.: Comparison of ZEN processing a 3D stack of SIM data with *thick slice* blind-SIM processing a single slice of data. a) ZEN result in the chosen slice z_0. b) Middle slice of the *thick slice* blind-SIM stack. c) ZEN result in slice z_2. d) Out-of-focus slice z_2 of the *thick slice* blind-SIM stack. The scale bar is 2 µm.

demonstrate that *thick slice* blind-SIM does not only reject the out-of-focus in the focal slice - even a bit better than the classical algorithm - but also correctly recovers information in the extra planes of the extended stack thanks to the axial extent of the 3D PSF.

3.4. Blind-SIM discussion and conclusion

We presented a state-of-the-art implementation of blind-SIM that is able to process two-dimensional SIM data of a thick sample requiring only a partial knowledge of the illumination patterns. We showed on simulated and measured biological objects that *thick slice* blind-SIM provides images with an optical sectioning and lateral resolution

enhancement similar to that of a 3D SIM system requiring only one single-slice acquisition.

It should be noted that a recently published blind reconstruction scheme [60] termed "patterned-illuminated Fourier Ptychography" may at first sight seem different, but is in fact identical if updating is performed after every single pattern comparison step by steepest descent with a step length of one [66].

With *thick slice* blind-SIM, we can reconstruct a 3D stack from a 2D slice measurement. However, a visual inspection shows that the retrieved out of focus information is not of very high image quality, therefore it is discarded in most of the cases. This can be improved by using a smart PSF design, for example with helical phase engineering [67].

Outlook for the blind-SIM project. In the future, we plan to modify the blind-SIM algorithm so that it can deal with 3D SIM serial slices in a unified model. This will be done with the help of multiple PSFs, one for each separated order.

To conclude this chapter of the present thesis, we have shown that our blind-SIM algorithm and especially its *thick slice* implementation contribute to the improvement of the SIM method on the side of the reconstruction. This was achieved by reconstructing mostly data by stable commercial systems, even though we also processed data of home-made set-ups, results which are not shown here. In the next chapter, we will turn to a more experimental approach on improving the speed performance of SIM and we will see that the deconvolution approach for data reconstruction is also in this case of great interest.

4. Speed enhancement in 3D SIM

4.1. The multifocus-SIM approach

4.1.1. Introducing multifocus microscopy

All light microscopy techniques based on wide-field detection - the WF microscope itself, and other examples like SIM or the single molecule localization microscopy (SMLM) approaches - require, in the simple implementation, mechanical z-scanning either of the sample or of the objective in order to bring different planes of interest in the nominal focal plane of the objective thus imaging them sharply but sequentially on the camera. To take the example of 3D SMLM, there exist realizations with sequential z-scanning - albeit neither simple nor traditional - for instance using selective plane illumination microscopy (SPIM) [68] or temporal focusing, where two-photon illumination confines the excitation to a single plane [69].

The scanning leads to acquisition speed limitation, vibrations, and enhanced risk of drift and other causes for artefacts. Thus, methods that enable parallel acquisition of two or more planes in the sample receive much attention. One possible way to realize this is the so-called biplane approach [70]. In the biplane approach, the emission path is split by one or several beam-splitters and directed to at least two cameras, or alternately different zones of the same camera [71]. In each of the arms, the distance between the camera and the tube lens is adjusted differently so as to image different focal planes. However, the biplane approach and all similar geometries are based on refocusing simply by translating the second camera away from the nominal focal plane, which leads to spherical aberration for large values of defocus [72].

In practice, the sequential mechanical scanning solution is rarely applied for 3D SMLM [73]. A first and still wide-spread possibility for performing 3D SMLM

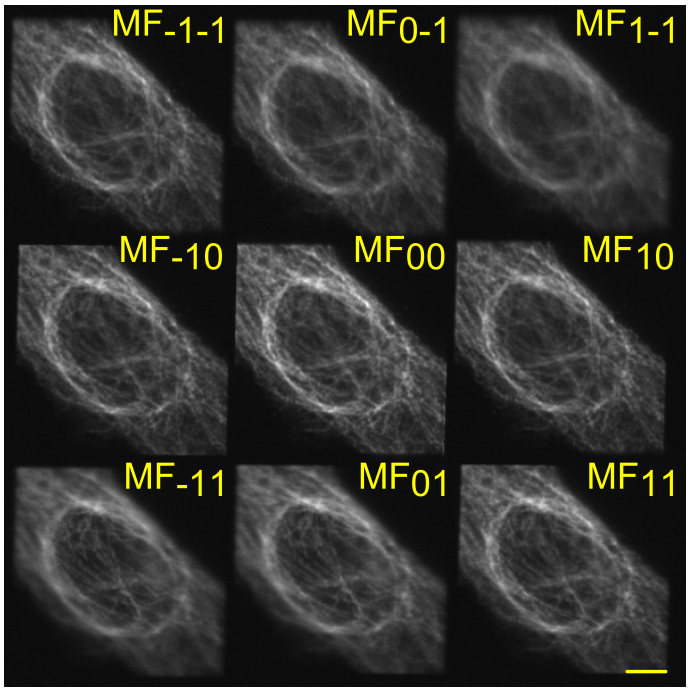

Figure 4.1.: An example of a 3×3 MFM image. We denote the different MFM slices with MF_{xy} with $x, y = 0, \pm 1$. The scale bar is 3 µm.

uses PSF engineering to perform the localization along z, typically with optically astigmatism [74], but other approaches exist [75, 76].
A second category of 3D SMLM or 3D tracking of single molecules uses multiplane detection [77, 78, 79], this approach also being commercially available [80]. An improved biplane design with eight planes was also applied to super-resolution optical fluctuation imaging (SOFI) [81].

An alternative to the biplane approach is the recently (2013) developed multifocus microscope (MFM). As explained in the following, the strength of MFM with respect to the biplane geometry is that it corrects for refocusing-induced spherical aberration. MFM enables instantaneous acquisition of a focal series [82] of typically 9 or even 25 planes [82, 83]. A diffractive element, the multifocus grating (MFG), splits the collected fluorescence signal into 9 components which each contain the desired defocus. Each component contains the full information of a WF detection, including out-of-focus light coming from other planes. The introduced chromatic dispersion is corrected by another diffractive element, the color correction grating (CCG), and a prism. As a result, the camera chip is separated into 9 sub-images, each corresponding

to the same lateral region of the sample but different focal positions.
In the following, we will describe the function of each of the MFM-specific components: the MFG, the CCG and the prism. However, we will give only a short description of the design and manufacturing considerations which can be found in more details in [82, 83, 84].

MFM can be implemented as a module to append to the camera port of an epifluorescence microscope without modification of the illumination optics. An example MFM image can be seen in fig. 4.1. It was successfully applied to superresolution microscopy by merging the method with 3D SMLM [85, 86] and to different imaging schemes based on WF detection [87]. The volumetric detection speed using MFM is either limited by the camera readout time of a single image or by the signal strength. Adding the MFM module to perform multifocus acquisition does not change the resolution, which is defined by the microscope to which it is attached.

The multifocus grating (MFG) is a diffractive component which is designed in two steps. First, using an iterative Fourier Transform Algorithm (IFTA) [83, 88], a phase-only pattern that evenly distributes light in 3×3 diffractive orders is calculated. The grating function, *i.e.* the basic shape which is reproduced with a certain periodicity, is thus determined. The grating function determines the energy distribution between the diffractive orders, which is adjusted to be as even as possible. In the case of the 3×3 MFG, the relative light intensity distribution in each order is typically of 10% of the incoming beam, except for the 0 order which intentionally suppressed to correct for losses in the CCG. If this diffractive element was manufactured, then we would simply obtain nine copies of the same WF image. Each copy corresponds to a diffraction order which we denote MF_{xy} where x and y can each take three values 0 or ± 1 (see fig. 4.1), thus yielding 9 combinations. There exists an alternate design with 5×5 orders, *i.e.* for $x, y = 0, \pm 1, \pm 2$ which we will not mention here. The desired distance between these copies depends on the experimental conditions (size of the sensor chip, focal length of the relay optics, hence MFG's average period). Hence, each MFG is designed for a specific set of experimental conditions and cannot always be used on another set-up [84].

Then, a carefully controlled distortion (chirp) is applied to the regular copies of the grating function in order to produce the focus shift Δz and compensate for depth-induced spherical aberration [89]. In order to understand the applied distortion, see

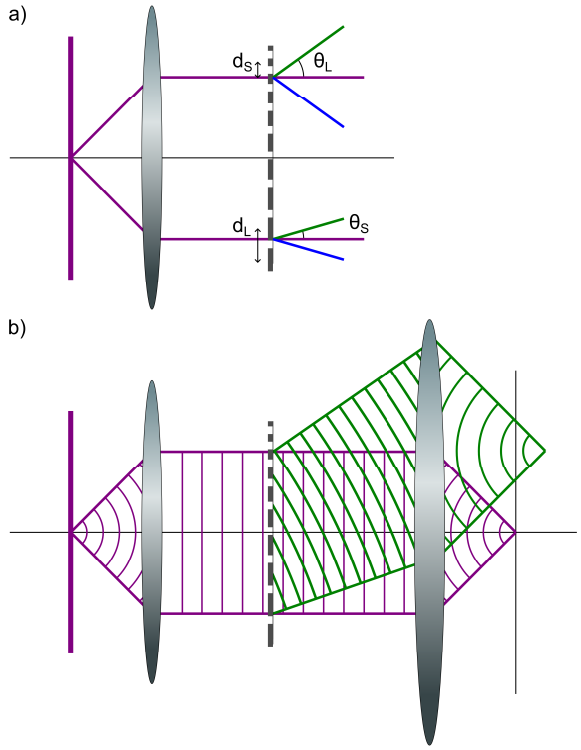

Figure 4.2.: Diffraction on a chirped grating illuminated by a plane wave (see also the supplementary material in [82]). a) The angle of diffraction θ is in relation with the grating constant d following $d \cdot \sin\theta_o = o \cdot \lambda$ where here we consider only the first diffraction order *i.e.* $o = 1$. Therefore if the grating is chirped, *i.e.* if the grating constant varies along the lateral coordinates, the light rays will be diffracted at a different angle depending on their position. In this example, at the top the grating constant is small d_S and therefore the diffraction angle θ_L is large, and at the bottom a large grating constant d_L leads to a small diffraction angle θ_S. b) The consequence is that the $+1^{st}$ diffraction order (green) is a diverging wave which therefore does not focus at the same axial position as the 0 diffraction order if we place a second converging lens. The -1^{st} diffraction order (blue in a), not represented here) is a converging wave focusing before the 0 order. b) also shows how light coming from the nominal focal plane does get spread into all diffraction orders. No optical sectioning is achieved with MFM detection.

fig. 4.2 and its caption [82, 89]. The principle demonstrated for a grating distortion in one dimension in fig. 4.2 and fig. 4.3 is applied in 2D on the grating described above which multiplexes the WF image in 3×3 copies. It should be noted that the grating distortion is calculated to introduce a defocus as well as to correct for the spherical aberration [82].

In the simple implementation, the MFG can be a binary phase-only element $(0 - \pi)$

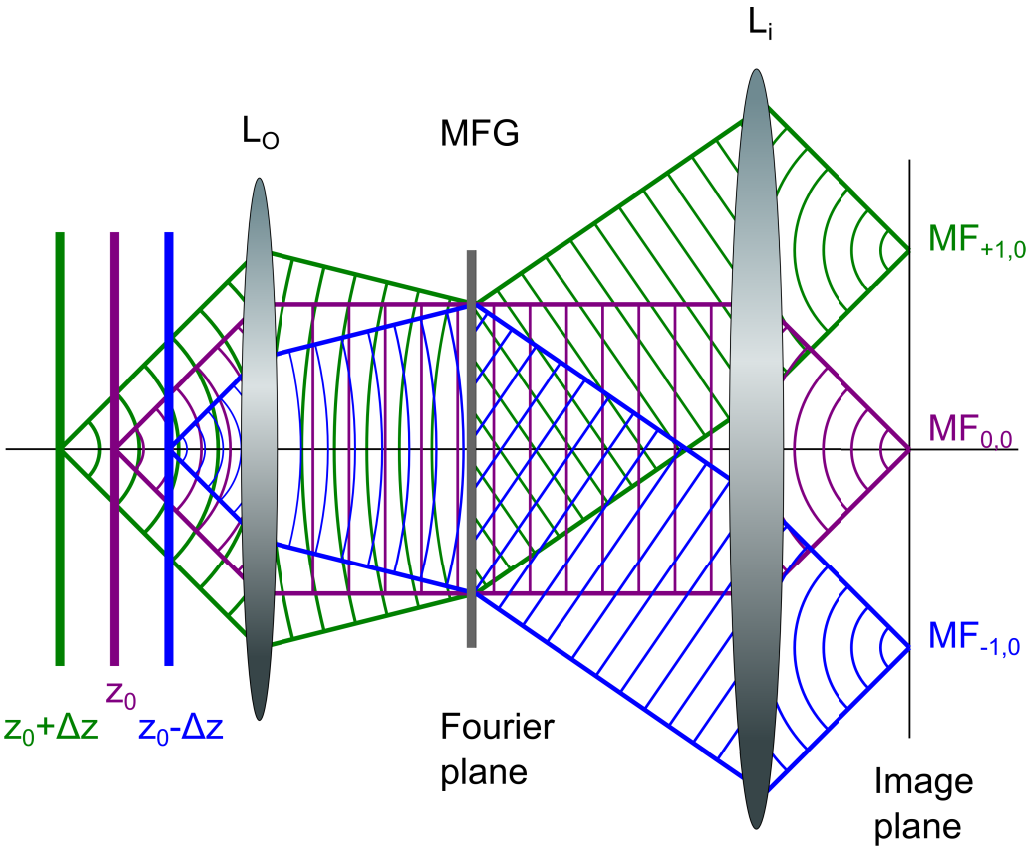

Figure 4.3.: Working principle of the MFG, presented here for three planes (see also the supplementary material in [82]). The purple rays describe schematically what happens to the light emitted in the nominal focal plane z_0. The objective lens L_O collects the rays and since they stem from the nominal focal plane, the resulting beam is parallel and is focused on the optical axis by an imaging lens L_i. Since the fluorophores lying in the planes above (blue) and under (green) the nominal focal plane were also excited, they will emit light which will also be collected by the objective. However, after the objective, the green and blue ray bundles will not be collimated since they stem from defocused plane at a distance of $\pm\Delta z$. The MFG, placed in the objective's Fourier plane, is a diffractive element calculated such that these beams are diffracted to the $\pm 1^{st}$ diffraction orders. Due to the calculated distortion in the MFG function, the diffracted beams are parallel. Therefore, each multifocus order MF_{xy} (where $x, y = -1..+1$ and $y = 0$ in this simplified example) converges in the focal plane of L_i, albeit at a position such that they do not overlap with each other. If a camera is placed in the imaging plane, it can record in a single exposure three focus-shifted copies of the sample in three different zones of the camera chip. It should be noted that MFM still performs WF detection, *i.e.* there is out-of-focus light of each plane into each of the MF orders, as pointed out in fig. 4.3b.

made of fused silica. In this case, the component can be realized using direct laser writing lithography. The etch depth corresponds to a π phase shift at the calibration wavelength. The theoretically reachable photon collection efficiency of such a binary MFG is ~67 % and it was measured in practice as ~65 %. To enhance the diffraction efficiency, it is possible to design and fabricate multi-phase devices but the fabrication is more challenging. The fabrication process involves successive rounds of deep-UV lithography [84]. The designed pattern of the MFG should consist of a finite number of smooth and continuous geometrical shapes, to make the fabrication using photolithography masks possible. The MFG used in this thesis has a eight-level grating function (eight equal steps from 0 to 2π, the last level corresponding to 2π) with a measured diffraction efficiency of ~80 % against ~90 % achievable in theory. Due to additional reflection losses of the order of 4 %, the total efficiency is therefore $0.96 \cdot 0.8 = 0.77$. The discrepancies between practically achieved and theoretical efficiency can be explained by the quality of the manufacturing process. It was determined that further increasing the number of levels, despite improving the theoretical efficiency further, does not significantly increase the practical performance, based on today's state-of-the-art nanofabrication facilities, while increasing the fabrication time and cost [84]. It is also possible to reduce the z-extent of the imaged volume, for applications that permit it, and to fabricate MFGs with 7 planes [84]. There are still 3×3 zones on the camera chip but the design of the diffraction efficiency is such that the first plane at the top as well as the last plane at the bottom do not receive light. Since the photon budget scales with the number of planes, each of the 7 plane will receive a higher signal than each of the 9 planes in the original 3×3 design.

We described here the working principle of the MFG which can produce an instantaneous focal series in the case of monochromatic light. However, such a diffractive component will introduce chromatic dispersion even within the spectral range of fluorescence emission (approx. 30 nm).

The color correction module (CCM) is made of two components that correct for the chromatic dispersion introduced by the MFG and keep the orders separation. First, the CCG consists of nine panels of differently oriented blazed transmission gratings. The CCG is placed at a distance from the MFG where the diffraction orders are well separated. The period of the blazed gratings is adjusted so that they compensate for the dispersion introduced by the MFG. However, the CCG alone

also reverses the image separation, leading to all diffraction orders again converging in the same spot on the optical axis. In order to deflect the diffracted orders while they are still separated, a multi-faceted refractive prism is placed directly after the CCG. The overall transmission of the CCM is quite high (~90 %) if the components fabrication quality is satisfactory and if the alignment is performed well.

The MFM detection scheme arrangement can be seen in the detection path of fig. 4.4. The total light efficiency of the whole MFM module is typically ~50 % in the best case.

4.1.2. Merging MFM with SIM

The SIM method is an obvious candidate for benefiting from a multifocus detection scheme. The extra factor gained in acquisition speed would reinforce the advantage of SIM over other superresolution approaches and pave the way to a new class of video rate imaging.

We combined the three-beam SIM (excitation side) and MFM (detection side) techniques. The resulting method, which we call MF-SIM, enables volumetric imaging at a two-fold 3D resolution enhancement with respect to the Abbe diffraction limit in three dimensions. The MF-SIM setup is represented in fig. 4.4.

4.2. Implementation with a commercial system

In a first step, we used an ELYRA-PS.1 (Carl Zeiss Microimaging, Germany) as the illumination module and opened the unused side port to insert the MFM components. A schematic representation of the Elyra-based MF-SIM set-up is shown in fig. 4.4. This configuration is not ideal for several reasons.

First, from the optical design point of view, it is not possible to know which components precisely are inside of a commercial microscope and how their design was optimized. The configuration of the objective and the tube lens is rarely that of a 4f system, *i.e.* the physical distance between objective and tube lens is not the sum of their focal lengths. The consequence is that the Fourier plane and the BFP

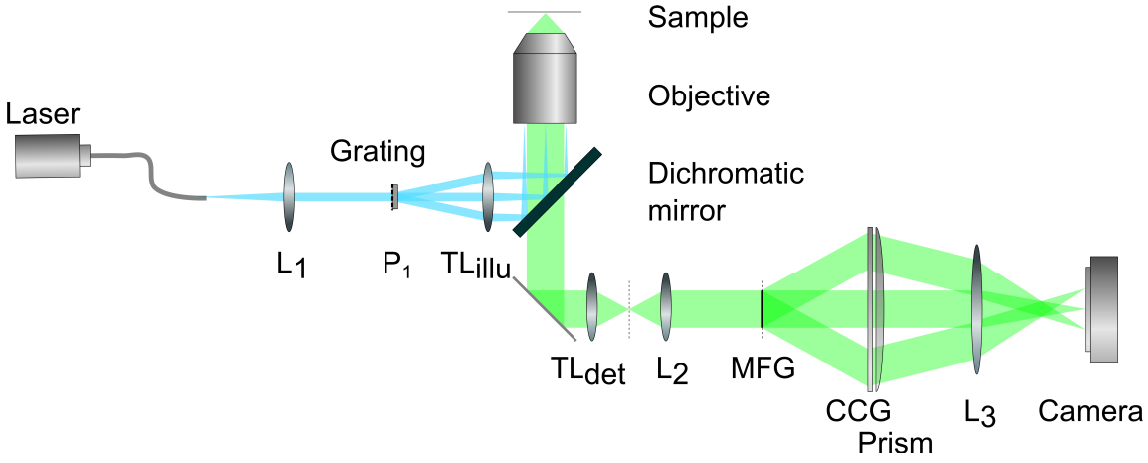

Figure 4.4.: MF-SIM set-up using the Elyra as SIM illumination module (blue beam path). The Elyra is represented in a very simplified sketch: a laser is collimated by lens L_1 and is illuminating a physical grating mounted on a motor. The polarization control necessary for maximum interference contrast is here represented by a polarizer P_1 placed directly after the grating. For phase shift and rotation of the illumination pattern, an image rotator is used. More detailed description of the SIM excitation path is given in the paragraph about the three-beam fast-SIM system in section 4.3. The detection beam path is directed to the side port via optical components here symbolized by a 45° mounted mirror. A first relay lens L_2 makes, together with the detection tube lens TL_{det} an image of the otherwise inaccessible BFP of the objective, where we place the MFG. After the CCM, a 75 mm diameter lens L_3 focuses the aberration-corrected multifocus orders on a camera.

are not coinciding. However, it is still possible to find the Fourier plane by using a Bertrand lens and to accordingly place the MFG in the Fourier plane. But this will slightly change the real magnification of the system, which can be taken into account in the design of the MFG.

Second, the triggering of the camera with the movement of the grating cannot be totally controlled since this is done by the complex and unmodifiable hardware-software structure of the Elyra. Hence, we can only adjust the setting of our camera on the side port so that it fits with the acquisition sequence. This is indisputably not the best way to synchronize the components, for instance because the risk for artefacts gets higher and the photon collection is not optimally efficient.

Finally, as we explained in section 1.3.1, the Elyra suffers from low acquisition speed. However, using the Elyra as SIM illumination module has the advantage of being a mechanically robust and light efficient solution, as well as being a well-known and widely used platform enabling comparison measurements, which permits a solid

starting base for a proof-of-principle experiment.

The sample used for the test experiments on the Elyra microscope was the FluoCells® prepared slide # 1 (Invitrogen Thermo Fisher Scientific, USA) containing bovine pulmonary artery endothelial (BPAE) cells tagged with different fluorophores. The dye that we are observing with the 488 nm excitation laser is Alexa Fluor® 488 phalloidin which is staining F-actin. The emission wavelength is 512 nm. The objective was a Plan-Apochromat 63 × /1.4 Oil DIC M27 (Zeiss). The relay lenses used in the MFM detection scheme had focal lengths of 150 mm (Thorlabs, USA) and 200 mm (Edmund Optics, UK) respectively. Since the tube lens in the Elyra PS1 is designed such that the magnification of the microscope is 1.6× higher, the total magnification of the sample through the MF-SIM detection optics is $63 \cdot 1.6 \cdot {}^{200\,\mathrm{mm}}/_{150\,\mathrm{mm}} = 134.4$. The camera used was sCMOS OrcaFlash 4 (Hamamatsu, Japan) with a physical pixel size of 6.5 µm, hence a pixel size in the sample plane of 48.4 nm. The exposure time was 1000 ms. These experimental parameters were applied to the set-up previously described and depicted in fig. 4.4. In fig. 4.5, we show an example of a raw MF-SIM image.

The reconstruction of the obtained raw MF-SIM data is not straightforward and is therefore the topic of section 4.4. The final reconstructed result of the raw data shown in fig. 4.5 is presented in fig. 4.29 and explained in section 4.4.2.

These results enable us to give a proof-of-principle for the MF-SIM technique with a commercial SIM instrument. The aim however is to apply MF-SIM to a home-built SIM system, which enables us a better control of the components and a higher flexibility. In the next section 4.3, we present a SLM-based three-beam fast-SIM system. In section 4.3.6 we present our preliminary MF-SIM results acquired with the SLM-based set-up.

4.3. Implementation with a home-built system

SIM systems which use a mechanical grating for the patterned illumination, like the Elyra, are typically suffering from a low acquisition speed. For the data presented in fig. 4.2, we observed that the laser shutter was closed in between the individual SIM acquisitions for 750 ms, which probably mostly corresponds to the mechanical

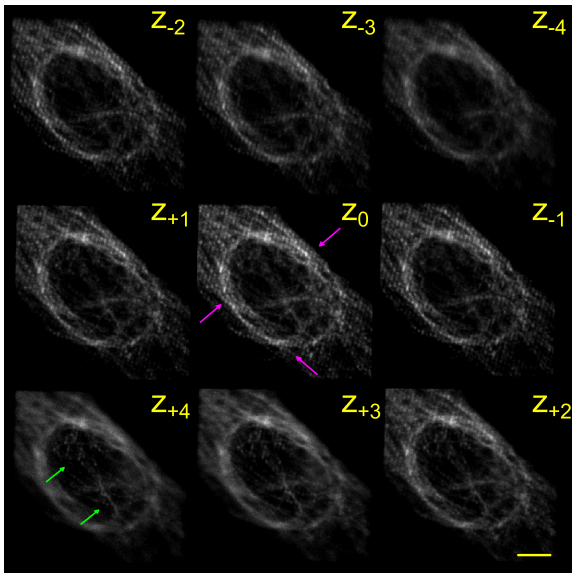

Figure 4.5.: One example of a raw MF-SIM image of a prepared F-actin sample. The camera chip is divided in nine zones corresponding to nine focal planes $z_i = z_0 + i \cdot \Delta z$ where z_0 is the nominal focal and for $i = -4..4$ the index referring to the different MF_{xy} orders. The defocus effect is visible: in each zone, different structures of the cell are in focus. Accordingly, the illumination pattern is blurry in the out-of-focus regions of the cell and sharp in the well focused features. As an example, in the zero MF order, corresponding to the nominal focal plane z_0, the filaments that form an oval shape are in focus and we can see the grating on them (magenta arrows). On the other hand, in the MF order at z_{+4} *i.e.* at the bottom of the imaged volume, the filaments that appear to be at the bottom of a bird's nest, are focused and modulated by the grating (green arrows). The scale bar is 3 µm.

movement of the grating. The manufacturers claim a minimal acquisition duration of one SIM image of 1.4 s for a size of the ROI of 512×512 pixels [42]. This corresponds to the whole acquisition process of fifteen raw images and the grating movement and possible other synchronization timings which play a role.

A meanwhile common approach to make SIM considerably faster consists in using a spatial light modulator (SLM), as mentioned in section 1.2.3. The SLM modulates the phase of the beam and thus produces a diffraction pattern that can be tuned by the pattern addressed to the liquid-crystal on silicone (LCoS) display. The update rate of the display we are using (SXGA display driven by the 3DM revB motherboard, Forth Dimension Displays, UK) can reach beyond 1 kHz. SLMs have been used in two-beam SIM systems [28, 29, 90, 91, 92] and in three-beam SIM systems [27, 54].

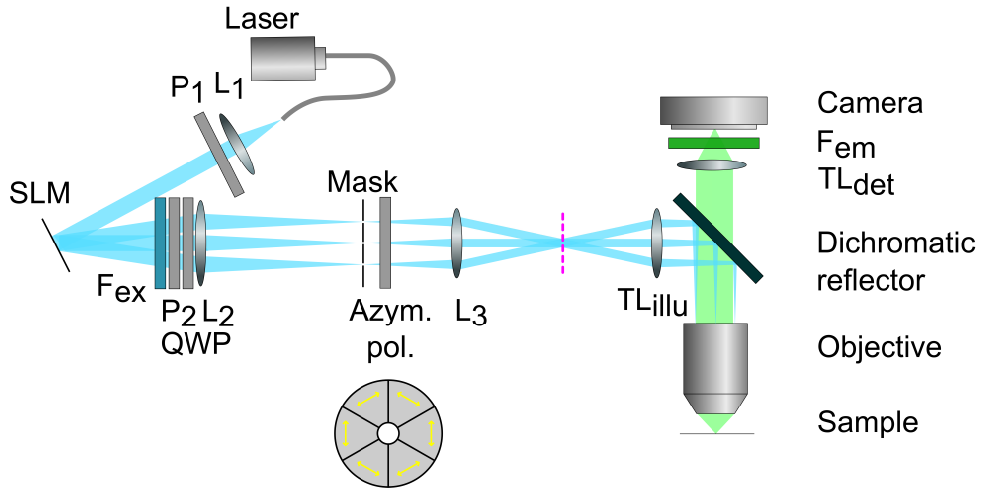

Figure 4.6.: Sketch of the three-beam fast-SIM system. A polarized and collimated laser beam illuminates the spatial light modulator (SLM). Due to the displayed binary grid, light is diffracted mostly to the 0 and $\pm 1^{st}$ orders. The polarization state is cleaned up by a the polarizer P_2 and rendered circular by a quarter wave plate (QWP). In the BFP of L_2, L_3, we place an aperture which cleans up the unwanted diffraction orders due to the pixellated nature of the SLM display. Only the 0 and $\pm 1^{st}$ orders are transmitted by the order selection aperture and azimuthally polarized by a segmented linear polarizer. The fluorescence light is cleaned up by an excitation filter F_{ex} placed directly after the SLM since this device leads to a small amount of auto-fluorescence. The three orders are focused in the BFP of the objective and can interfere in the sample space. Fluorescence light is collected and cleaned up by an emission filter F_{em}. Finally, a sCMOS camera performs the image in WF mode. The dashed magenta line represents an image plane.

As detailed in [92], using a reflective ferroelectric SLM and state-of-the-art components permits to go down to an acquisition time of 55 ms (corresponding to a SIM imaging rate of 18 Hz) for a ROI size of 512×512. It is even possible to further enhance the acquisition speed by synchronizing partial displays with the rolling shutter camera as detailed in [93].

The three-beam fast-SIM system that we built is inspired by the early design presented in [91, 92, 94], but extended to three-beam interference. A detailed set-up is depicted in fig. 4.6.

We use a 488 nm laser illumination (LuUX, Germany) which we collimate using an achromatic doublet (focal length 60 mm, Thorlabs, USA). The linear polarization of the laser is cleaned up by a polarizer (04 CA 25, Comar Optics, UK) oriented in

between the polarization axes of the on and off states of the SLM (see section 4.3.2 for more details). The SLM display (SXGA-3DM, ForthDD, UK) is a ferroelectric liquid crystal on silicon (FLCoS), which has the advantage of enabling an extremely fast change of display (up to 3.2 kHz). The section 4.3.2 below is devoted to more details on the SLM. Since the SLM has a small auto-fluorescence response, we place an excitation filter F_{ex} (BP 485/20, Carl Zeiss, Germany) right behind. The role of the second polarizer P_2 (04 CA 25, Comar Optics, UK) is to clean up to polarization state of the $\pm 1^{st}$ orders and explained in more details in section 4.3.2. The two lenses L_2 and L_3 (focal lengths 300 mm and 250 mm respectively, Thorlabs, USA) demagnify the grating and make an image of the Fourier plane where an order selection aperture is placed. Due to the pixellated nature of the SLM display, many unwanted orders are generated and need to be filtered out by an aperture (see fig. 4.7). The order selection aperture consists in a piece of black cardboard pierced of seven holes at the position of the 0 and $\pm 1^{st}$ orders for the three grating orientations. In order to reach optimal interference contrast, the polarization of the individual beams should be controlled. A detailed explanation about polarization control is given in section 4.3.3. The illumination tube lens, TL_{illu} (focal length 200 mm, Thorlabs, USA) focuses the 0 and $\pm 1^{st}$ orders on the BFP of the objective (UPlanSApo 60× / 1.20 W, Olympus, Japan, referred to as "the water objective"). The collected fluorescence signal is separated from the excitation light by a dichromatic beam-splitter (zt 488-rdc-phaseR, Chroma Technology Corporate, USA), cleaned up by an emission filter F_{em} (BrightLine® FF01 - 525/45 -25, Semrock, USA) and focused on a sCMOS camera (OrcaFlash 4 C11440-22CU, Hamamatsu, Japan) by the detection tube lens (focal length 180 mm, Thorlabs, USA). It should be noted that, as opposed to the set-up described in [92] where two dichromatic beam-splitters are used to ensure that the polarization is maintained, such a precaution is not required in our case. Indeed, the dichromatic beam-splitter used in this work benefits from a specific design that minimizes the phase shift between the reflection of the s- and p-polarization components at the wavelength of 488 nm.

The opto-electronic components (laser shutter, SLM, camera acquisition) need to be carefully synchronized in order to get rid of easily avoidable artefacts in the image. A whole section 4.3.4 is devoted to the synchronization task and the description of the home-built electronics board.

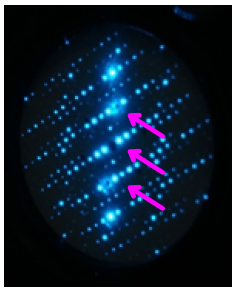

Figure 4.7.: Unwanted orders from the SLM. The magenta arrows point towards the holes in the clean-up aperture that filter only the wanted 0 and $\pm 1^{st}$ orders.

4.3.1. Fibre shaker

Goal and motivation. In fluorescence microscopy, monochromatic light is preferred since the stained samples have a well-defined excitation spectrum. Specifically in SIM, high temporal coherence is essential for high interference contrast and thus contrast of the illumination pattern. Spatial coherence is also important for the contrast of illumination pattern. Introducing a little bit of spatial incoherence will only have some positive effect though.

High spatial coherence often leads to speckle artefacts. Speckle is a random interference pattern which can be observed when shining a laser beam on a granular diffusing surface. In a microscope beam path, small dust particles on the optics lead to scattering and interference effects, and their coherent images also degrade image quality. Even though speckle is not necessarily a disturbing effect in microscopy, it is in most cases desirable to get rid of the speckle artefacts by introducing a certain degree of partial incoherence.

In SIM specifically, there is another advantage. If the light is only partially coherent, the contrast of the grating will decrease out of the focal plane which in turn leads to a better optical sectioning. Partial spatial incoherence slightly modifies the OTF. First, there is a smearing of the amplitude orders in BFP, *i.e.* they are not small dots any more but a sightly wider area made up out of many smaller spots which are all incoherent to each other. Second, before diffraction on the grating, the source should be seen as a multitude of mutually incoherent point sources. Thus, out of all point sources present in the diffracted orders, each can only interfere with one corresponding point source in another diffracted order. The effective illumination

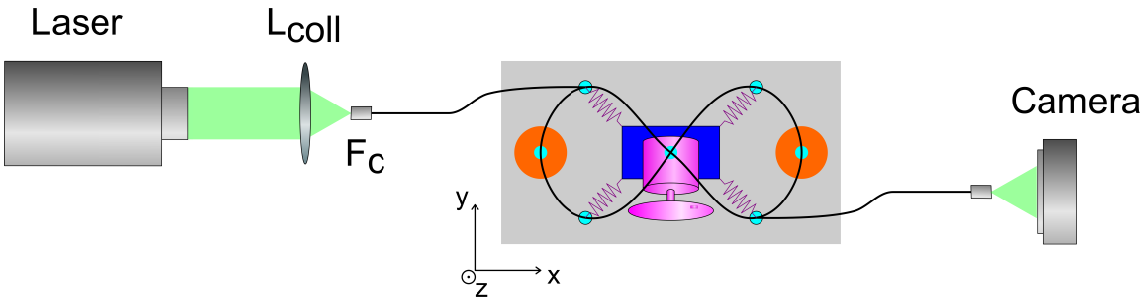

Figure 4.8.: Sketch of the fibre shaker and description of used components in the test bench. Light from a laser is coupled into a multimode optical fibre. The collimation and coupling optics is here symbolized by a single lens L_{coll}. The fibre connector F_c is a SPA adaptor. The fibre is folded in the shape of a 8 and attached at the center to a platform (blue) held by springs (purple). High amplitude, low frequency, vibrations are submitted to the platform via an excenter motor (magenta). On both sides of the 8, the fibre is glued to piezo loud speakers (orange)) which produce high amplitude, low frequency vibrations. Both vibrations are mostly along direction z. The cyan dots represent the anchor points. At the output of the fibre, the speckle pattern is directly observed on a camera.

pattern in the probe is therefore an incoherent superposition of point pairs (two-beam SIM) or triplets (three-beam SIM), as can be seen in fig. 1.9c.

Method. In order to introduce partial spatial incoherence in a laser illumination, we developed a simple mechanical solution inspired by the device used by the Gustafsson group [22, 27, 52].

The so-called fibre shaker produces high frequency mechanical vibrations to a folded optical fibre without plastic jacket. A sketch is depicted in fig. 4.8. The fibre is folded in the shape of an 8 several times over the length of 15 m. An excenter motor produces vibration at ~10 Hz at the center of the 8 (applied DC voltage 3 V). The excenter motor is a motor that has an off centre weight attached to the axle, hence when the axle rotates, the platform to which the motor is attached wobbles. Two piezo loud speakers (PT1-1010) placed at each most exterior side of the two loops of the 8 produce 15 kHz vertical vibration thanks to a high voltage function generator which applies a square wave of frequency 15 kHz.

The reason for using a fibre without plastic jacket is that attenuates and dampens the vibrations and thus lessens the modes mixing.
We used the available fibre AFS105/125Y (Thorlabs, USA), multimode fibre used

for the telecommunication field using near infrared wavelengths, which is also multimode at the work wavelength of 532 nm as it is the case in the test bench used for characterizing the fibre shaker.
Indeed, the number of modes is ${}^{V^2}/_2$ where the V-parameter is defined as [95]

$$V = \frac{2\pi \cdot R_{core}}{\lambda} \cdot \sqrt{n_{core}^2 - n_{clad}^2}, \tag{4.1}$$

where R_{core} is the radius of the fibre's core, n_{core} and $n_{cladding}$ are the refractive indices of the core and cladding respectively, and $\sqrt{n_{core}^2 - n_{clad}^2}$ is the fibre's NA. In our case, $R_{core} = 105\,\mu m$ and NA $= 0.22$, yielding a V-parameter of 273. A fibre is considered monomode for $V < 2.4$.

The mechanical shaking leads to a mixing of the modes in the fibre. It should be noted that the modes also mix without the mechanical shaking but in this case the mixing would always stay the same and still lead to speckle patterns. The mechanical shaking changes the phases of all the mixed modes, changing the speckle patterns. Optimally, the extent of this area should be approximately 5% of the BFP area. Further extending it leads to a loss of resolution because the center of the order is further away from the border of the WF OTF (see fig. 1.9).

Characterization. In order to characterize the incoherence, we measured the speckle pattern by directly imaging the output of the shaking fibre on a camera (Clara, Andor Technology, UK), and measured the standard deviation of the image. The comparison of the case where the fibre shaker is on and when it is off has been performed for several integration times. The results are presented in fig. 4.9.

Results. This simple fibre shaker device can reduce the speckle pattern up to 96% for a very short integration time of the camera of 1 ms and 97% for a longer integration time of the camera of 10 ms.

Conclusion. The fibre shaker is a useful device for future experiments with two-beam SIM. However, three-beam SIM already has a good optical sectioning capability and it is in our case not necessary to introduce partial spatial incoherence. Using the fibre shaker in our three-beam SIM system would lead to loss of light and no real advantage. Furthermore, the order selection aperture would need to be wider, thus creating a risk to collect unwanted orders. Therefore we did not use this component

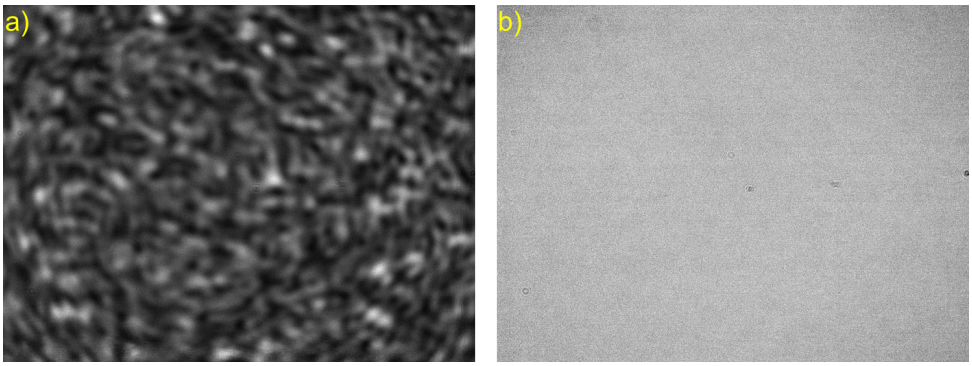

Figure 4.9.: Removal of the speckle thanks to the fibre shaker device. a) Image of the speckle observed at the output of the fibre if the fibre shaker is turned off. b) Same view as a) if the fibre shaker is turned on. Both acquisitions were realised with an exposure time of 1 ms.

in the remaining work presented in this thesis.

4.3.2. Considerations regarding the SLM

Working principle of the FLCoS display. Each pixel of the SLM acts effectively as a half wave plate (HWP) [94, 96]. A voltage that rotates the liquid crystals (LC) can be applied to each pixel, which results in a rotation of the fast axis of the HWP between two states (binary display). The manufacturer indicates an orientation of 0° if the pixel is OFF or 30° if the pixel is ON [97], where 0° is the parallel to the short side of the SLM and in our case perpendicular to the optical table. The SLM acts as a phase-only diffractive element [94]. The work in [94] explains in detail the implications of the wavelength change with respect to the calibration wavelength, the imperfections considering polarization states and other aspects related to the practical work with the SLM.

Polarization axes of the SLM. It is necessary to measure the real orientation of the HWP axis of the ON and OFF state. For this, we display an image on the SLM where all pixels have the boolean value 1 (referred to as “all bright”). We synchronize the laser shutter (see section 4.3.4) so that we illuminate the SLM only when it displays the “all bright” image. Section 4.3.4 presents, along with the synchronization procedure, the different electronic states (positive and negative image) of the SLM. We use a polarizer to make sure that the input polarization is vertical and we measure

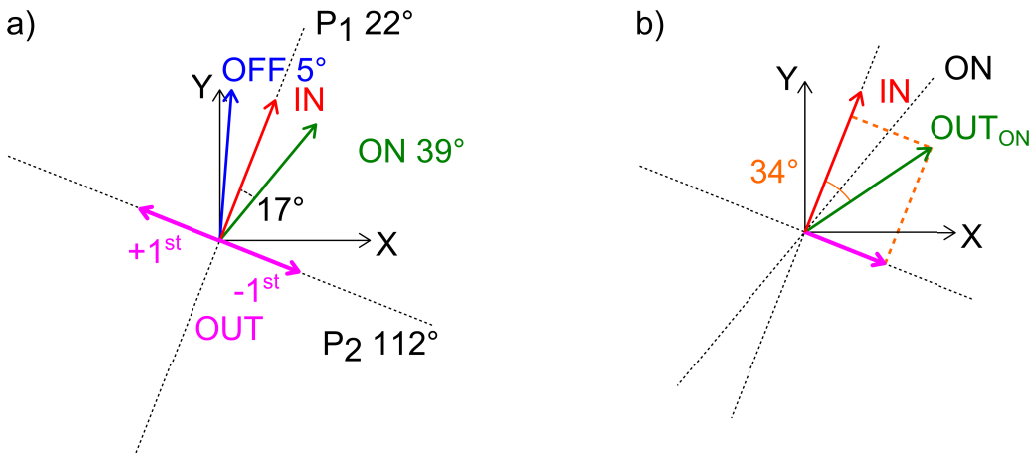

Figure 4.10.: a) Measured orientation of the axes of the SLM (X and Y are the laboratory coordinates): the ON state (green) corresponds to a HWP with a fast axis oriented at 39°, the OFF state at 5°. The input polarization P_1 (red) should be in between. b) A portion $\sin 34°$ of the incoming light is diffracted into one of the first orders.

the output polarization by rotating an analyser and searching for the best extinction. The extinction indicates the direction to which the input polarization vector (0°) has been rotated, *i.e.* twice the orientation of the HWP axis. We thus found an orientation for the ON state of 39°. Repeating the same procedure by synchronizing the laser illumination on the negative image (all pixels are OFF) yields an orientation for the OFF state of 5°.

The input polarization (orientation of P_1 in fig. 4.6) should be in between the ON and OFF axes of the SLM *i.e.* oriented at 22°. Interestingly, the $\pm 1^{st}$ diffracted orders (orange in fig. 4.10a) are polarized perpendicularly to P_1 as shown in [94]. It is still useful to use an analyzer P_2 (magenta in fig. 4.10a) which should be crossed to P_1 (see fig. 4.10a) for several reasons:

- to efficiently select the $\pm 1^{st}$ diffracted orders,
- to compensate for the phase error arising from the fact that the SLM does not behave as a perfect HWP due to dispersion in the LC [94],
- and to get rid of the fraction of light (~4 %) that gets reflected on the first glass surface on the SLM which is polarized as the input polarization.

In this configuration and if the measurement of the polarization axes was performed

correctly, we expect an almost extinguished zero diffraction order when we display one of the SIM gratings, which we can use a quality measure for this calibration and alignment step. We measured 0.33% (in average for all three grating orientations) of the intensity in the 0 order with respect to the sum of the intensities measured in the 0 and $\pm 1^{st}$ orders. These measurements were performed with a powermeter (Nova II, Ophir Optronics, Israel) after the order selection aperture to avoid the unwanted orders. As explained below in the paragraph dedicated to the three-beam case, the fill factor changes this value. These measurements were realized for FF=50 (see definition of FF below).

Efficiency of the SLM. As can be seen in fig. 4.10b, only a portion $\sin 34° = 0.56$ of the incoming electric field amplitude gets diffracted. The measured intensity in the first order is therefore $0.56^2 = 31\%$ that of the intensity incident on the SLM. This figure corresponds to the diffracted efficiency in all $\pm$ orders except the 0 order due to polarization losses. The diffraction efficiency is defined as the intensity in the $\pm 1^{st}$ orders with respect to the incoming intensity. In the case of a transmittance of 1 (perfect phase-only diffraction grating), the diffraction efficiency is therefore also the intensity in the $\pm 1^{st}$ orders with to all diffraction orders. It can be shown mathematically that the diffraction efficiency of a binary phase diffraction grating with phase shift π is then 40 % [98]. Therefore, we reach an intensity in a single one of the $\pm 1^{st}$ orders which is only $0.4 \cdot 0.31/2 = 6\%$ that of the incident beam. This is approximately the experimentally measured value of 3 %, the difference being explained by reflections on the device. This is a major limitation of our SLM-based system using the FLCoS display.

Three-beam case. Theoretically, the zero diffraction order should be totally extinguished in the configuration depicted in fig. 4.10a. However, we do want to perform three-beam interference. Additionally, it is desirable to have a 0 order polarized along the same direction as the $\pm 1^{st}$ orders and not perpendicular as would be the case if we were using the residual reflection. It is sufficient to have ~2 % of the total intensity in the 0 order. We can achieve this by changing the fill factor of the binary grating displayed on the SLM. The fill factor corresponds to the fraction of ON pixels out of the number of pixels in one period. We denote the parameter FF as the fill factor in % unit. Until now, we had as many ON pixels as OFF in a grating period, corresponding to FF=50. We measured the relative intensity in zero order for all three grating directions for different FF values and found that FF=45

yielded approximately the desired value of 2 %.

The grating constant on the SLM should be chosen according to the desired resolution improvement. Let us introduce the resolution enhancement factor F_{res} as:

$$F_{res} = \frac{d_{min}}{d_{samp}}, \tag{4.2}$$

where d_{min} is the Abbe limit as defined in eq. 1.1 and d_{samp} is the period of the fine grating in sample plane (see fig. 4.11). A user-defined F_{res} (typically around 0.8 - 0.9) therefore leads to the corresponding grating period on the SLM d_{SLM}:

$$d_{\mathrm{SLM}} = \frac{2 \cdot d_{samp}}{M_{im}}, \tag{4.3}$$

where M_{im} is the magnification between SLM and sample plane. M_{im} is defined by the lenses L_2, L_3, the illumination tube lens TL_{illu} and the objective (see fig. 4.6) of focal lengths denoted respectively f_2, f_3, $f_{\mathrm{TL},illu}$ and $f_{obj,\mathrm{eff}}$. $f_{obj,\mathrm{eff}}$ is the effective focal length taking into account the change of refractive index between the immersion medium and the objective. $f_{obj,\mathrm{eff}}$ is usually not given explicitly but the magnification of the objective M_{obj} as well as the manufacturer's detection tube lens focal length, $f_{\mathrm{TL},det}$ are known. For the Olympus objective we have:

$$f_{obj,\mathrm{eff}} = \frac{f_{\mathrm{TL},det}}{M_{obj}} = \frac{180\,\mathrm{mm}}{60} = 3\,\mathrm{mm}, \tag{4.4}$$

and

$$M_{im} = \frac{f_{obj,\mathrm{eff}}}{f_{\mathrm{TL},det}} \cdot \frac{f_3}{f_2} = 0.0125. \tag{4.5}$$

The grating period on the SLM display should be expressed in number of pixels:

$$d_{\mathrm{SLM},pixels} = \frac{d_{\mathrm{SLM}}}{s_{x,\mathrm{SLM}}}, \tag{4.6}$$

where $s_{x,SLM}$ is the pixel size of the SLM (13.6 µm for the SXGA). A home-written MATLAB algorithm calculates gratings of a period $d_{\mathrm{SLM},pixels}$ with the desired FF.

Practically, it is not possible to calculate gratings for $d_{\mathrm{SLM},pixels} \leq 2$. The choice of the lenses is made according to this limitation and also the available space.
It is possible to verify the grating's constant from the FT of the raw data where the peak of the coarse grating is usually visible. The Abbe limit in Fourier space expressed in number of pixels k_{max} was defined in eq. 3.6. Similarly, we can calculate the k-vector of the coarse grating k_0 in number of pixels with

$$k_0 = \frac{s_x \cdot scX}{d_{samp}}. \tag{4.7}$$

We should therefore observe a peak in the FT of the raw SIM images at a distance k_0 pixels from the center (origin of the k space). This corresponds to the period of the coarse grating (see fig. 4.11). Using the same SLM displays (same period $d_{\mathrm{SLM},pixels}$) in a two-beam SIM experiment (simply by blocking the zero order) leads to a period in the sample plane of $d_{samp}/2$ (see fig. 4.11) and equivalently a peak at $2k_0$, even though this is rarely visible in the FT of the raw data. This peak corresponds to the fine grating, also present in three-beam SIM. If the spatial frequency of the peak is too high to be observed in the FT of the raw data, it is possible to use a simple image processing approach using cross-correlation (see appendix C).

The Nyquist sampling should be fulfilled, *i.e.* the pixel size in sample plane scX should be smaller or equal to half of the minimal resolvable grating constant d_{min}.

$$scX \leq \frac{d_{min}}{2}. \tag{4.8}$$

In our case, assuming an emission wavelength of $\lambda_{em} = 520\,\mathrm{nm}$ and using the water objective with NA = 1.2, we have a maximum pixel size to fulfil the Nyquist sampling

$$scX_{max} = \frac{\lambda_{em}}{4\mathrm{NA}} = 108.33\,\mathrm{nm}. \tag{4.9}$$

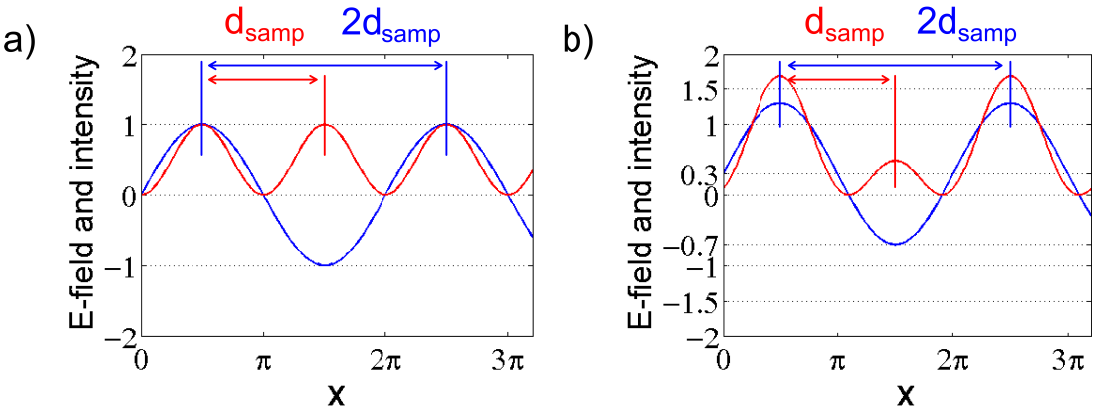

Figure 4.11.: Patterned excitation. a) Two-beam case (blue: amplitude of the electric field, in this sketch $\sin x$ is represented, red: intensity $\sin^2 x$). b) In the three-beam case, there is an offset a due to the zero order and the electric field becomes $\sin(x)+a$ (drawn here for $a = 0.3$).

The pixel size in sample plane for the OrcaFlash 4 (physical pixel size of 6.5 µm) with the water objective of magnification 60× is precisely at the Nyquist limit and we have $scX = scX_{max} = 108.33\,\text{nm}$.

Using the silicon objective, which also has a magnification of 60× but a NA = 1.3, yields an unchanged pixel size in the sample plane of 108.33 nm but a new Nyquist sampling limit of:

$$scX_{max} = 100\,\text{nm}, \tag{4.10}$$

and therefore the SIM measurements in the first image plane should be performed with the water objective.
Since the MFM arm has an extra magnification $^{200\,\text{mm}}/_{150\,\text{mm}} = 1.33$ due to the two relay lenses, thus a total magnification of 80× and a new pixel sample in the sample plane $scX = 81.25\,\text{nm}$, corresponding to a correct sampling.

4.3.3. Polarization control

Overview of theoretical considerations. The illumination pattern in SIM should have a high contrast as it directly relates to the SNR of the reconstructed high

frequencies [99]. Out-of-focus light, optical aberrations, and polarization in high NA imaging conditions are parameters that affect the contrast. Indeed, the illuminating two or three beams interfere with best contrast if their polarization vectors are parallel. Additionally, the contrast of the grating should be the same for all orientations. In fig. 4.12, we see that without polarization control, *i.e.*all orders are oriented along P2, the contrast depends heavily on the position of the beams in the BFP, and hence will not be the same for all directions. If we had a radial polarization arrangements (purple orders in fig. 4.12), we would have a constant interference contrast, however not as high as with a azimuthal arrangement (purple orders in fig. 4.12). This can be realized in practice with mechanically rotating components (typically a HWP), but for the SLM-based system, a faster variant is desirable. It should be noted that, for a given NA, it is indeed possible to find three grating orientations that enable acceptable contrast without external polarization control [99], at the cost of less flexibility. In the following, we describe and compare two different polarization control approaches, one of them using a passive optical element and the other an opto-electronical device.

Passive solution. The azimuthal polarization can be reached using a custom-made segmented azimuthal polarizer made of six segments of a glass polarizer foil (colorPol® VIS 500 BC4 CW01, Codixx, Germany) [91, 92]. After P_2, a quarter wave plate (QWP) is placed to create a circular polarization state. The segmented polarizer is placed directly after the order selection aperture, where the diffraction orders are small and well-separated. For three-beam SIM, the center of the segmented polarizer is made of a glass with no polarization properties of same refractive index as the polarizing segments, thus leaving the zero order circularly polarized (see the insert in fig. 4.6). It is manufactured so that the possibly introduced wavefront distortions are minimal.

The advantage of this solution is that, the component being passive, it does not limit the acquisition speed of the system. However, it introduces further intensity losses and the polarization state of the zero order is not optimal. The circularly polarized zero order can interfere equally with the $\pm 1^{st}$ orders of all directions, but the contrast would be higher if it was co-rotated for each direction. Nevertheless, this solution gave good results. The 1^{st} order strength, as defined by the sum of the intensity in the $\pm 1^{st}$ orders divided by the sum in all 0 and $\pm 1^{st}$ orders, was measured to be 93 %.

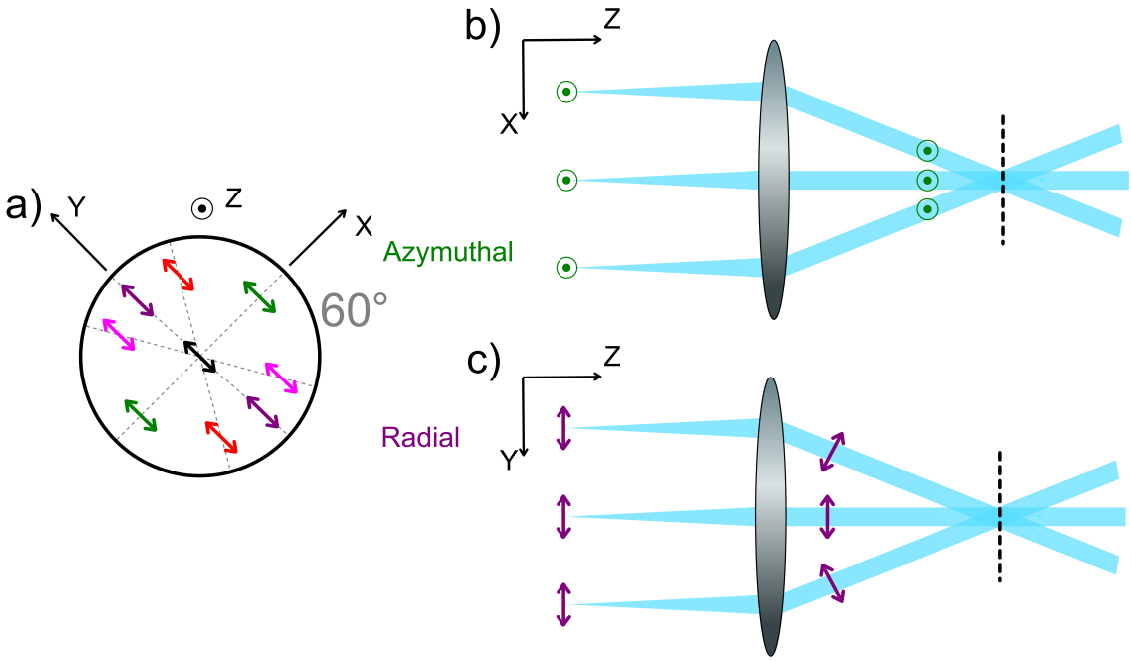

Figure 4.12.: Polarization and interference contrast. a) A homogeneously linearly polarized beam along P_2 (no polarization control) would lead to the interference of three different triplets of polarization states: green, magenta and red (with the 0 order). This situation leads to a different interference contrast for each orientation. b) Azimuthally arranged orders interfere with best contrast. c) Radially arranged orders interfere with lesser contrast [94]. If the whole BFP was radially arranged, all directions would have the same, albeit not maximal, interference contrast.

Active solution. Another solution exists, which is to use a swift liquid-crystal (LC) polarization rotator [52]. The device used (SRC-200-VIS, Meadowlark Optics, USA) consists more precisely of a variable retarder and is referred to in the following as "the LC cell". Depending on the voltage applied to the LC cell, the retardance between slow and fast axes can be continuously tuned. To reach effectively a rotation from the input linear polarization state to a rotated linear polarization state, a QWP is placed after the LC device (see fig. 4.13).

As we saw in section 4.3.2, the polarization of the first orders after the SLM, P_2, is defined by the SLM axes and cannot be rotated (unless one rotates the SLM display itself, which is practically very challenging). As depicted in fig. 4.10a, P_2 should be precisely oriented in between the fast and slow axes of the LC cell. A precise alignment is crucial. Even small angles mistakes ($\gamma_1 \neq -45°$, $\gamma_2 \neq -45°$, see fig. 4.13, or tip-tilt of the LC cell) can lead to an improper or inaccurate behaviour of the

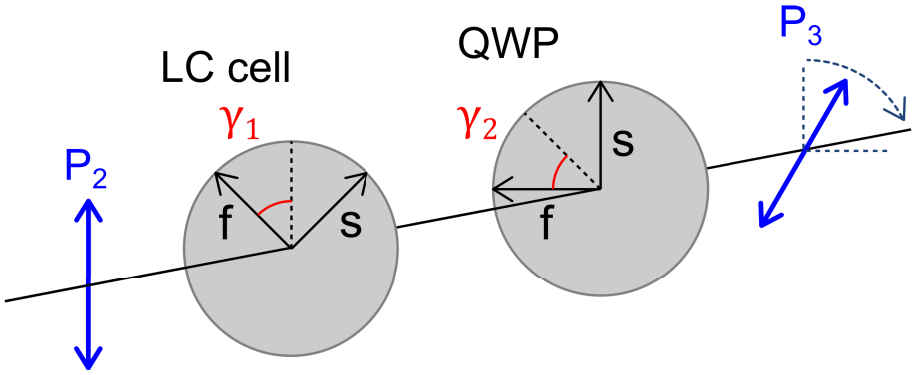

Figure 4.13.: Polarization rotation module made of a LC variable retarder and a QWP. The incident light should be linearly polarized. For simplicity, we draw here P_2 at 0° but as presented in fig. 4.10a, it is instead 112°, so that the whole module has to be rotated. The output polarization P_3 is rotated with respect to P_2.

polarization rotator module. We observed that

- the relation between input voltage and orientation of the output polarization is not linear,
- and the quality of the linearity (extinction ratio) is not constant over the whole voltage range,

if the sensitive alignment is not performed perfectly.
Additionally, we noticed that the retardance applied to the incident electric field depends on the angle and position of the beam on the first surface of the LC cell. We illuminate the polarization rotator module with a thin parallel beam (linearly polarized along P_2) perpendicular to the LC surface and we characterize the output polarization P_3 for several voltages and different position of the beam on the LC surface (cases A to C in fig. 4.14). The polarization state is always linear with a good extinction ratio of ~99 %, however a given voltage value does not give the same orientation of P_3 (measured thanks to the analyser A in fig. 4.14). This means that if the SIM orders go through different regions of the LC cells, their polarization will not be rotated of the same amount and therefore we will not reach the desired azimuthal arrangement. A similar observation is made if we illuminate the LC cell always in the same region but at different angles (case D in fig. 4.14). Interestingly, placing the LC cell in the image plane (dashed magenta line in fig. 4.6) corresponds to a geometry where all orders are going through the same zone. They come at different angles,

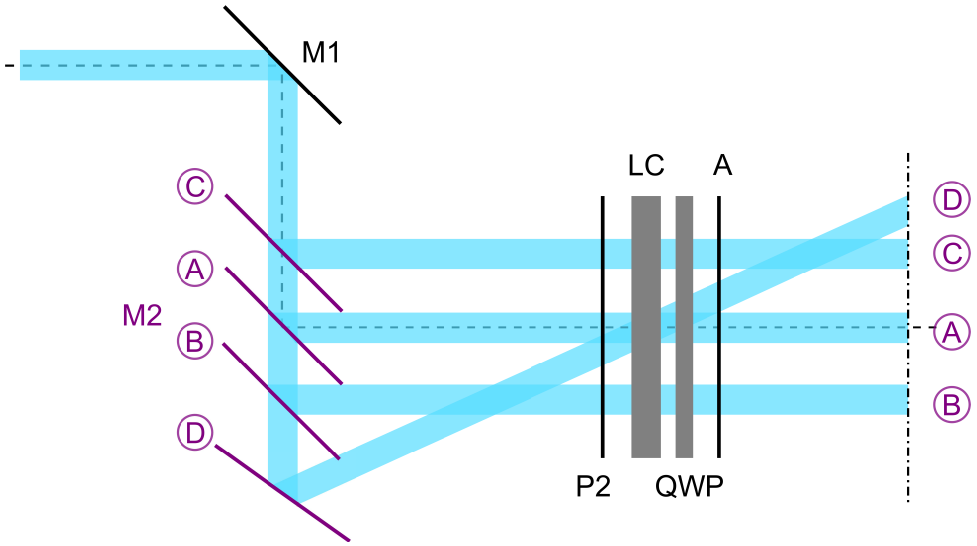

Figure 4.14.: Characterization of the LC polarization rotator: dependence on incident angle and position. The mirror M_2 is moved to different positions (A-D) so that we illuminate the LC cell at different positions and angles. The resulting polarization state is analysed using an analyser A and a powermeter placed in the plane represented by the dashed line.

but since the angles are small, we assume that it will lead to negligible errors.

Once the correct geometry is defined, it is necessary to determine three voltage values to apply to the LC retarder that lead to the desired P_3 orientation for each grating direction. Further calibration procedures are therefore necessary.
A first naive approach consists in placing an analyser after the dichromatic beamsplitter and orienting its axis along the orders for each grating orientation (see fig. 4.15a). We then apply different voltages to the LC and search for the best extinction. The voltage for which the powermeter reading after the analyser is minimum corresponds to azimuthal arrangement (see fig. 4.15a). However, this approach gives only a rough estimate of the correct voltage and it is impractical because it requires removing the objective. Nevertheless, these experiments enabled us to suspect an instability. Indeed, the voltages found seemed to be drifting over time. These two reasons motivated an automatic approach.

A home-written calibration procedure (see section 4.3.4) changes sequentially the voltage applied to the LC cell. The start and end values as well as the step are user-defined for each grating orientation. For each applied voltage, the five usual SIM phase steps are performed and a SIM acquisition series acquired for a bright

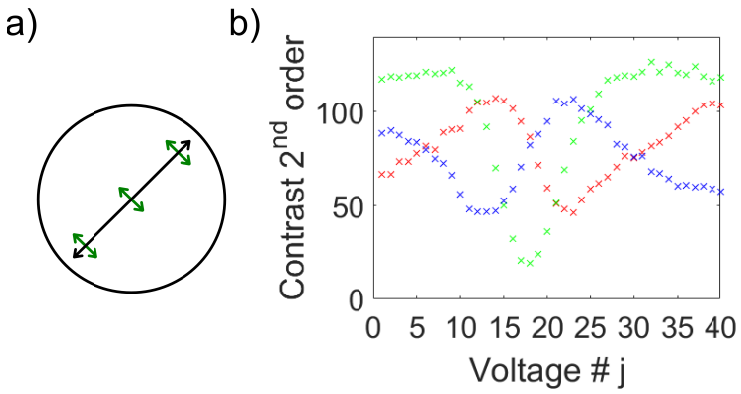

Figure 4.15.: Calibration of the voltage applied to the LC polarization retarder. a) Naive approach: search the voltage for which the SIM orders are best extinguished. Black: axis of the analyser for one SIM direction. Green: azimuthal polarization of the SIM orders. b) Calibration curves as a result of the automatic approach. The applied voltage V_{app} is iteratively changed so that $V_{\text{app}} = V_0 + (j+1) \cdot \Delta V$, where the start voltage V_0 and the increment value ΔV are user-defined. An algorithm (see appendix C) plots the peak-to-mean value of the 2^{nd} order SIM peak with respect to j. Red: direction 1 (50°), green: direction 2 (-10°), blue: direction 3 (-70°).

and homogeneous test sample (typically a dense monolayer of fluorescent particles, realized with a marker pen on a coverslip and air embedding). A MATLAB function then plots the peak-to-mean value of the second order peak with respect to the voltage (the code can be found in appendix C). The procedure is repeated for each direction and the three voltages giving maximal SNR are selected. A typical calibration curve is displayed in fig. 4.15b.

Performing the automatic calibration at several points in time (see fig. 4.16) enabled to confirm the drift. It is necessary to always perform an automatic calibration before a SIM measurement in order to reach and azimuthal polarization and thus a maximum interference contrast for all three grating orientation.

Comparison of both approaches. The LC-based system enables to rotate, thanks to an automatic calibration approach, the polarization for each direction. We checked that the rise time was sufficiently short for our application. We placed an analyser after the polarization rotator module so that it is crossed to P_3 for a given first voltage V_1 applied to the LC cell. We observed a bright sample in WF mode for a minimum exposure time of 1 ms. We changed the voltage to a second value $V_2 \neq V_1$

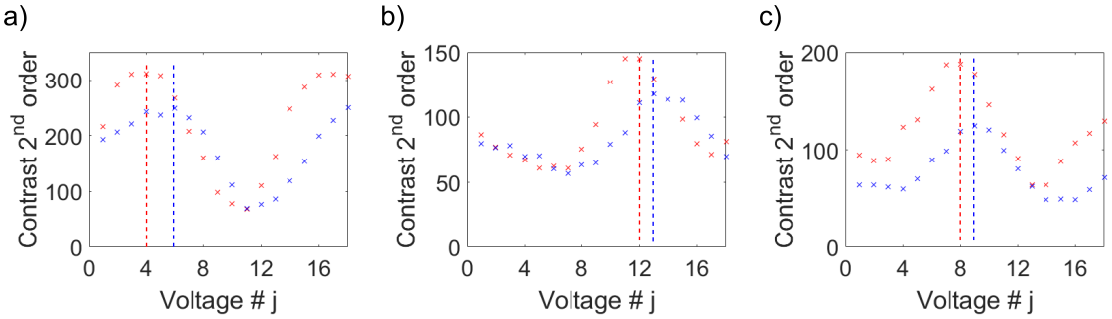

Figure 4.16.: Temporal stability of the LC polarization rotator. The automatic calibration was performed at several points in time (see fig. 4.15). Red: first calibration. Blue: second calibration performed half an hour later. a) Direction 1. b) Direction 2. c) Direction 3. It can be observed that the best voltage value (dotted lines) drifts over time. Additionally, the contrast diminished probably due to a thermal effect.

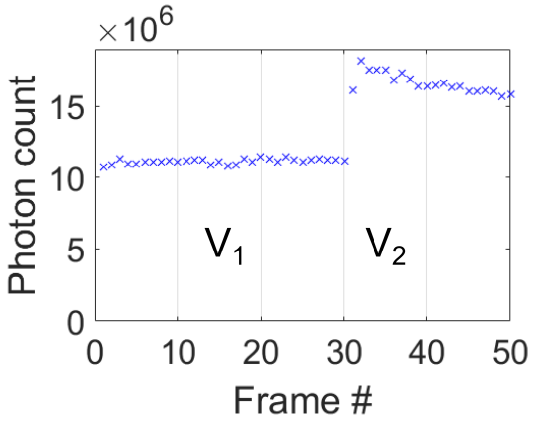

Figure 4.17.: Rise time of the LC polarization rotator module. A time series was performed. In each time frame, we sum all pixels and plot the resulting photon count. The voltage applied to the LC cell was changed from V_1 to V_2 just after the acquisition of frame # 30 was finished.

during the readout of a known frame. We confirmed that the new polarization state was already reached and stable in the next frame (see fig. 4.17).

On the other hand, the solution with the segmented polarizer is more practical. We could not see any qualitative nor quantitative difference in the contrast of the illumination pattern in the sample. We therefore select the passive solution for polarization control as easier and equally effective. The SIM data presented in section 4.3.6 are acquired with the passive segmented polarizer.

4.3.4. Synchronization approach

We are using several opto-electronic components: the camera, the SLM, the laser that can - and, as we will see, should - be shut on and off by an electronic shutter, and optionally the LC polarization rotator. These components need to be synchronized, by taking into account three requirements:

- Optimize the acquisition time,
- Protect the components,
- Optimize the image quality

The logical brain of the system, realizing the synchronization tasks, is an Arduino UNO micro-controller (Arduino, Italy), referred to as "the Arduino". In the following, we detail the synchronization considerations for all components and we finally present how we realized the implementation with the Arduino.

The camera has several operation modes and the one that fits best in this case is the so-called "free running mode". The camera is also the slowest of all opto-electronic components, therefore it is the master in the triggering sequence, *i.e.* the component that starts the synchronization sequence and for which all other devices are waiting [100]. In the free running mode, several input and output logical signals (triggers) are available. We use the signal called "global exposure", denoted `GLOB_EXP`, which indicates when all lines of the sensor in the chosen ROI are exposed. Indeed, this sCMOS has a rolling shutter which gradually exposes and reads the lines [101]. It is known [100] that exposing the sCMOS sensor during the opening or closing of the shutter leads to artefacts. `GLOB_EXP` is high when the shutter has finished opening all the lines and this is the trigger for starting the acquisition sequence (see fig. 4.19). Furthermore, the logical level of the input and output levels of the camera is 3.3 V [100], whereas the logical level of the Arduino and most other components is 5 V. In order to protect the electronic components, it is necessary to use a level-shifter.

The SLM also has several modes and is faster than the camera (3.2 kHz against 1.6 kHz for useful ROI size (*e.g.* 2048×128 pixels, longer for larger number of rows) [101]). Since typical exposure times in fluorescence microscopy are of the order of 100 ms, we choose a sequence which displays the pattern for $T_d = 5$ ms, and we repeat

the same pattern N_{rep} times to reach the desired effective exposure time. A sequence is a set of instructions - supplied by the manufacturer - given to the mother board (-3DM M117 revB) that determines the duration and settings of the display of an image. Amongst the supplied sequences, 5 ms corresponds to the longest possibility. If the probe is particularly bright, it is very easy to choose another sequence which can display patterns for a time as short as 100 µs.
The running order is programmed by the user and defines which sequence will be applied to each calculated patterns, for how many repetitions N_{rep} and, if necessary, after receiving an input signal.
When the high level of `GLOB_EXP` is detected, the Arduino triggers the beginning of the running order on the SLM display (`SLM_TRIG`). The SLM will start to load the first pattern, which was previously loaded and stored on the memory of the SLM mother board. Loading a pattern on the display takes $\tau = 434\,\mu s$ [97]. Illuminating the SLM display when some pixels are in an undefined state leads to artefacts, therefore it is desirable to have a feedback from the SLM mother board when the display is indeed loaded and when does the 5 ms sequence indeed starts. We therefore use the so-called "LED enable" output signal, denoted `LED_EN`, which is high when the SLM display can be illuminated (see fig. 4.19).
The working principle of the ferroelectric SLM imposes to apply the negative pattern, *i.e.* all pixels that were ON are turned OFF and inversely, to the display within 50 ms [97]. In our case, the negative pattern is applied directly after the positive pattern, with as always a loading time of $\tau = 434\,\mu s$ in between. It is easy to see how the π-shift leads to the same intensity pattern in two-beam SIM. Interestingly, it is also possible in three-beam SIM to use the negative pattern during the same camera acquisition because the fill factor also gets inverted (see fig. 4.18).

The electronic laser shutter, triggered with the signal `LAS_ON`, is used to make sure that the SLM display is illuminated only during the periods when `LED_EN` is high. The rise time is less than $\epsilon = 2\,\mu s$ [102]. The camera is integrating during the whole time. The SLM displays are repeated as often as necessary to reach a long enough effective integration time. The fact that the camera integrates over the whole time (manual exposure time setting is $T_{\text{exp}} = 2N_{\text{rep}} \cdot (T_d + \tau)$) including when the laser shutter is shut down (effective exposure time is $T_{\text{eff}} = 2N_{\text{rep}} \cdot T_d$) does not come at a cost of a noise increase with respect to the case where the camera is only integrating for $T_{\text{exp}} = T_{\text{eff}}$ since the thermal noise buildup is negligible for our

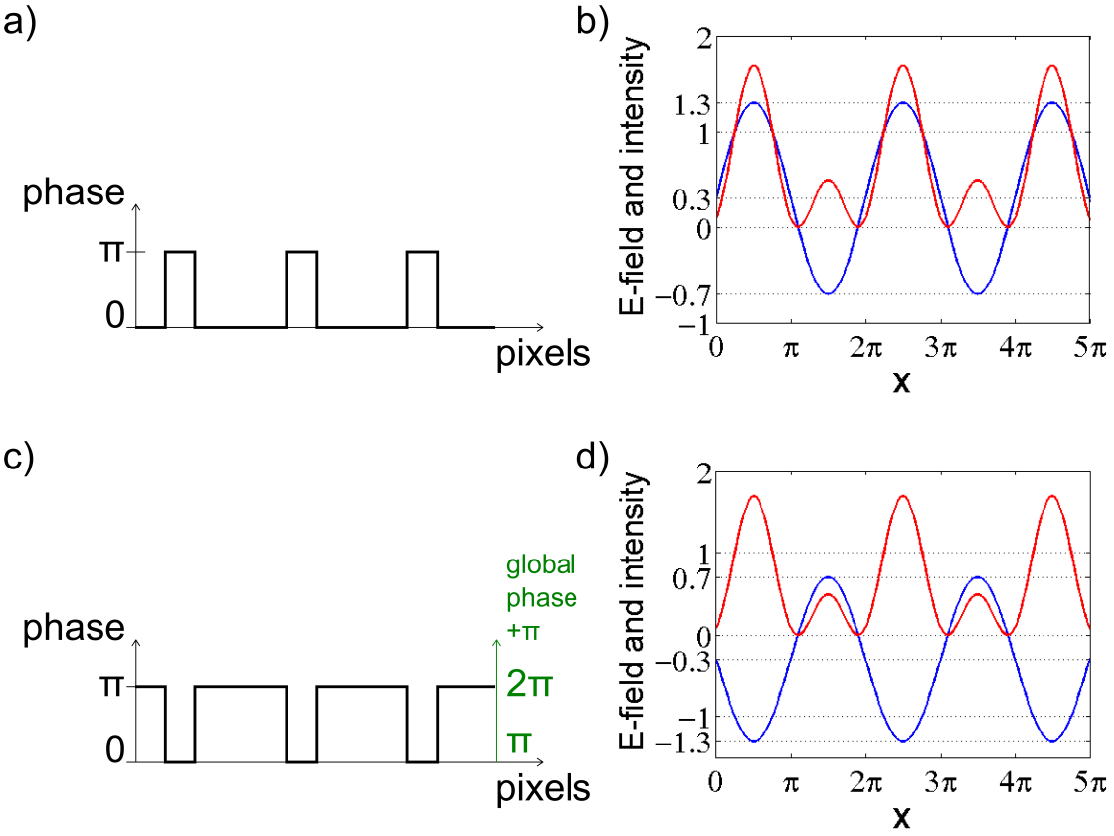

Figure 4.18.: a) Conceptual binary phase grating for an arbitrary fill factor (positive image on the SLM display). b) Resulting interference pattern in the sample (blue: electric field $\sin(x) + a$, red: intensity $|\sin(x) + a|^2$). Arbitrary offset a depending on the fill factor (here $a = 0.3$). c) Corresponding negative image. d) Blue: $\sin(x + \pi) - a$, red: $|\sin(x + \pi) - a|^2$). The intensity patterns (red) are the same in b) and d).

settings (0.02 electrons/pixel/s in the water cooling mode at −30 °C [101]). Then, the shutter starts to close and the read-out procedure starts. `GLOB_EXP` thus goes low, the laser shutter closes, and the SLM waits for the next trigger signal. In the free running mode, the rolling shutter opens each line to the new exposure as soon as the readout line has passed to next line [100]. If the whole sensor is used (2048 lines), the readout time is 10 ms, less if the chosen ROI has less lines [100]. Therefore, the acquisition of the next SIM frame starts after 10 ms, and the next grating pattern is loaded on the SLM display. We show in fig. 4.19 a logical diagram of the described acquisition sequence. In practice, logical signals were measured with a logic analyser (Saleae, USA).

The LC polarization rotator is driven by a high voltage controller (D3060 HV, Meadowlark Optics, USA). The controller can itself be driven by a computer via a USB or serial port, but it also provides the possibility of being driven directly by an external input signal, which in our case is an analog DC signal which we denote `MEAD_VAL`. The three pre-programmed values (see the calibration procedure in section 4.3.3) of `MEAD_VAL`, corresponding to the three rotation angles, should range between 0 and 5 V. For the experiments using the LC polarization rotator, we therefore needed a digital to analog converter (DAC, MAXIM MAX532) to enable the programming of an analog signal with the Arduino. Precise instructions to avoid damaging the controller and/or the LC cell itself are given in [103].

The practical implementation of the synchronization procedure presented above is realized with a home-built Arduino system. In order to protect the components, care is taken by choosing adequate resistors to limit the current applied to the Arduino ($I_{max,Arduino} = 40\,\mathrm{mA}$) and to each device (input impedance and maximal current are always specified). Additionally, the SLM mother board being in contact with the optical table (electrical ground), it is electrically isolated from the Arduino using an ADuM 1400. The ADuM makes sure the ground levels of the SLM mother board and that of the Arduino are indeed both at 0 V, therefore that the logic signals on both sides do not exceed 5 V.

4.3.5. Microscope stage and detection pathway

Most major microscope manufacturers work with infinity-corrected optical systems where the image formed by the objective is set at infinity and is focused on the detector by a detection tube lens. However, the involved optical design aiming at reducing or compensating optical aberrations (spherical and chromatic aberration) typically has two consequences. First, the corrections are only valid for use of an objective together with a tube lens from the same manufacturer. Second, the distance between objective and tube lens is fixed in the design of the microscope body and usually does not correspond to the sum of the focal lengths (4f configuration).

In our case, we need to have access to the detection path in order to place the MFM components. Especially, the MFG should be placed in the objective's Fourier plane. First, microscope bodies are bulky and second, the objective's focal length

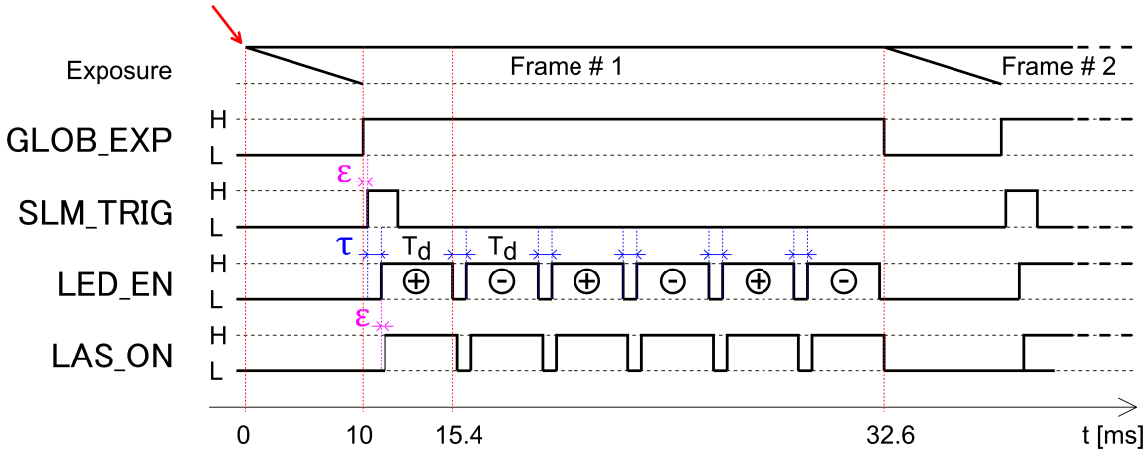

Figure 4.19.: Logic diagram of a SIM acquisition with a repetition of the SLM sequence of $N_{\text{rep}} = 3$. Here we display only what happens for the first SIM image (one grating phase, one orientation). The evolution of the different logical signals (states high H or low L) is represented with respect to time. The red arrow represents the start of the acquisition by the user: the camera exposure starts, *i.e.* the rolling shutter opens. Since for MF-SIM the whole camera chip is required, the readout time is of 10 ms. In this example with an equivalent exposure time of $T_{\text{eff}} = 30$ ms, a new SIM frame can be acquired after 32.6 ms. ϵ is a negligible loading time of certain components. In this mode, the SLM displays the negative image right after the positive image.

is usually smaller than its mechanical length. Therefore, it is necessary to image the Fourier plane by a system of two lenses, the detection tube lens TL_{det} and the first relay lens L_{R1} (150 mm focal length, Thorlabs, USA). It would be desirable to do so in a 4f configuration because in a telecentric system the BFP and the Fourier plane coincide. However, for the reasons stated above, this is not possible with a commercial microscope body and most of the available objectives.

We therefore chose to use an objective where the correction for spherical and chromatic aberration (infinity color correction) is entirely included in the objective design. The UPLSAPO 60XS (Olympus, Japan, referred to as "the silicon objective") fulfils this requirement. We can now use any achromatic doublet of focal length 180 mm as a tube lens TL_{det} (AC508-108-A-ML, Thorlabs, USA). In order to be able to place TL_{det} in a 4f configuration after the objective, we designed our own stage with scanning along x, y, z using piezo linear positioning systems the smarAct (SLC-24120 for $x - y$ scanning and SLC-2475 in z, smarAct, Germany). The design can be seen in appendix D.

It should be noted that, in order to fulfil Nyquist sampling (see the last paragraph of section 4.3.2), the water objective was used for the measurements presented in this section as well as all measurements performed for the camera in the first image plane.

Stability considerations. It is crucial to avoid sample drift during the SIM acquisition. For fixing the sample on the stage, we use three sapphire balls of diameter 1 mm (KS1-G25, Quick-Ohm, Germany) which are inlaid in the sample holder so as to offer three reference points. The microscope slides is held tight at these three points by three pairs of neodymium magnets (Magnetworld, Germany). Furthermore, all sources of vibrations in the room should be avoided. In particular, water cooling is preferable to air cooling with the integrated fan. However, we shut off the pump of the water cooling system shortly before each measurement.
Under these optimized conditions, we imaged 100 nm fluorescent beads (PCFP-0252, Kisker Biotech, Germany) over 1500 ms. The effective exposure time was 1.75 ms - exposure time setting in the acquisition software of 3 ms, with laser being triggered on the `GLOB_EXP` signal, for a ROI of 256×256 pixels. We performed the data analysis in MATLAB: after background subtraction, we used a self-written drift correction routine based on a correlation approach (see appendix C). The standard deviation of the vector of calculated shifts (a time series of 500 images were acquired) serves as quantitative stability assessment. The results of the stability calibration are depicted in fig. 4.20. We found a standard deviation of 0.07 pixels in x and y under optimized conditions (fig. 4.20a). Since this measurement was done with the water objective (magnification 60×) and the OrcaFlash 4 camera (physical pixel size 6.5 µm), the pixel size in sample plane is 108.3 nm. Hence we measured a standard deviation of 7.6 nm. As a comparison, the fan of the camera (air cooling mode) introduces strong vibrations (fig. 4.20b : standard deviation of 0.19 pixels *i.e.* 20.6 nm). Turning off the air flow in the room is equally important for stable measuring conditions since it also introduces vibrations (fig. 4.20c : standard deviation of 0.11 pixels *i.e.* 11.9 nm).

4.3.6. Experimental results

Imaging with the three-beam SLM-based system. In order to test our three-beam SIM set-up, we placed the camera in the first image plane and used several

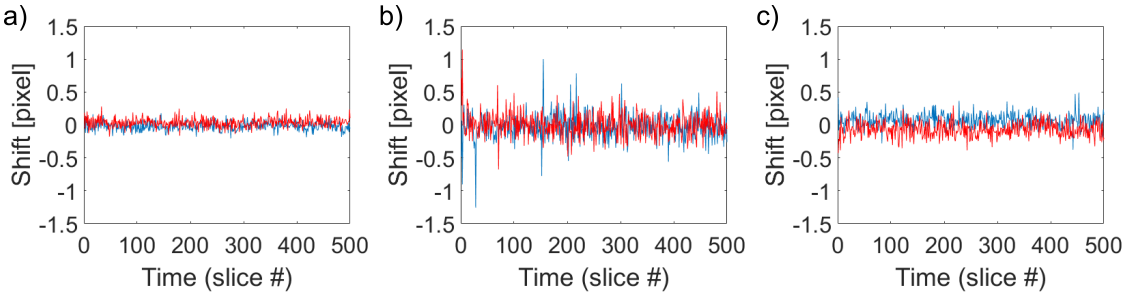

Figure 4.20.: Stability measurements. a) Optimal measurement conditions (water cooling is turned off for the time of the measurement, fans of the cleaning air flow in the room are turned off). b) Same as a) but in air cooling mode, *i.e.* fan of the camera is turning. c) Same as a) but by turning on the fans in the room. Blue: shift in x, red: shift in y.

test samples. The objective used for these measurements was the water objective. In fig. 4.21, we demonstrate the resolution enhancement of our system on a beads sample. We put a drop of 2 µL of 100 nm from a fluorescent beads solution (1/10 concentration) on the coverslip (18×18 mm, 170 ± 5 µm, $\#1.5H$, Marienfeld Superior, Germany), spread it with the pipette tip and let it dry. Then, we added a drop of 5 µL of distilled water and sealed the coverslip with two-component silicone putty (twinsil®, Picodent, Germany) on a microscope slide.
The grating period in sample space was 241 nm, *i.e.* the resolution enhancement factor F_{res} (see eq. 4.2) is 82% since the recorded emission of the fluorescence beads has a maximum at 515 nm. The exposure time was 33 ms and the laser power 140 mW (70% of maximal power). A 512×512 ROI was imaged.

Fig. 4.21 confirms the resolution enhancement and imaging performance of our SIM system. We subsequently inserted the MFM components on the detection arm of the microscope. A mirror mounted on a flip mount enables to direct the beam either to the first image plane or to the MFM set-up. On both arms, the detector is a OrcaFlash 4 camera.

MFM detection. The sketch of the MFM detection is presented in fig. 4.4, albeit for the traditional excitation scheme using a mechanical grating. We use the same MFM components as presented in section 4.2. A square slit is placed in the first image plane to adjust the size of the FOV and to avoid cross-talk between the different MF orders. The first relay lens has a focal length of 150 mm (Thorlabs, USA). The second relay lens should be wide enough to collect all MF orders without

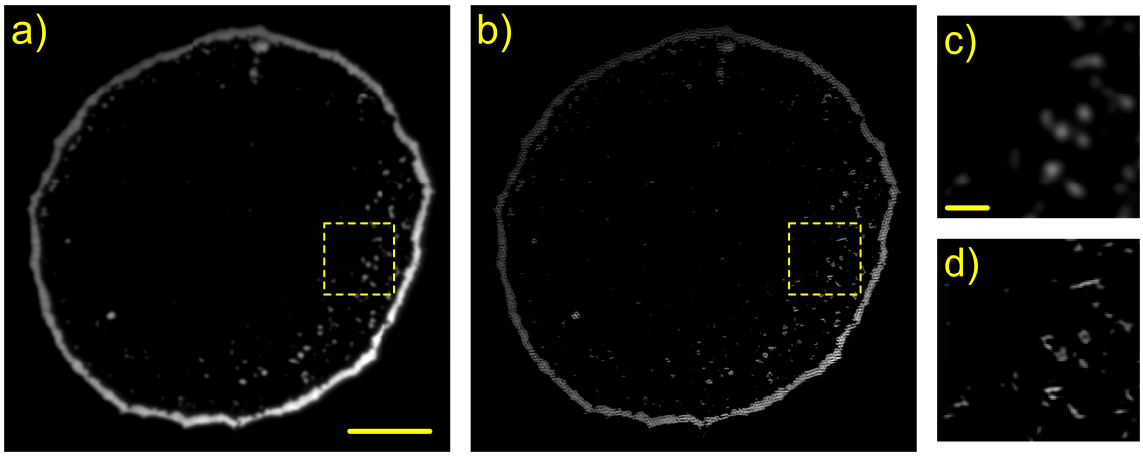

Figure 4.21.: Three-beam SIM result on a 100 nm beads sample. a) WF image deconvolved with a Wiener filter. b) Reconstructed SIM image. c) Zoom on the dashed box in a). d) Zoom on the same region in b). Scale bar in a) and b) is 5.8 µm, and in c) and d) 1 µm.

vignetting them, we therefore use a 75 mm diameter achromatic doublet of focal length 200 mm (Edmund optics, USA). Our preliminary results using WF excitation and MFM detection are presented in fig. 4.22 and fig. 4.23.

In order to check whether we can shift and focus features of the sample in each of the MF_{xy} orders, we used a sample made of a dense monolayer of fluorescent particles. This test sample has the advantage of being very thin, bright, and simple.
We developed an automatic acquisition procedure with LabVIEW (National Instruments, USA) which performs a z-stack acquisition, either in WF mode or in three-beam SIM mode. By changing the range and the spacing between the acquired slices, we could check whether we could focus the monolayer sample in turn in each of the MFM order. The results are presented in fig. 4.22.

In fig. 4.22, we observe that the multifocus effect is present, *i.e.* several MF_{xy} orders come in focus at different z positions, but significantly distorted by aberrations. The orders in the diagonal ($\mathrm{MF}_{1-1}, \mathrm{MF}_{-1-1}, \mathrm{MF}_{11}$ and MF_{-11} in right order following the z axis) are most affected by the aberrations, so that no clear focus is obtained in these zones. Furthermore, the distance between the orders where we do observe a focus does not correspond to theory. For instance, the two orders MF_{00} (fig. 4.22b) and MF_{-10} (fig. 4.22c) which are adjacent and should therefore be distant of 300 nm, whereas our observations in this dataset suggest a 600 nm axial distance. On the

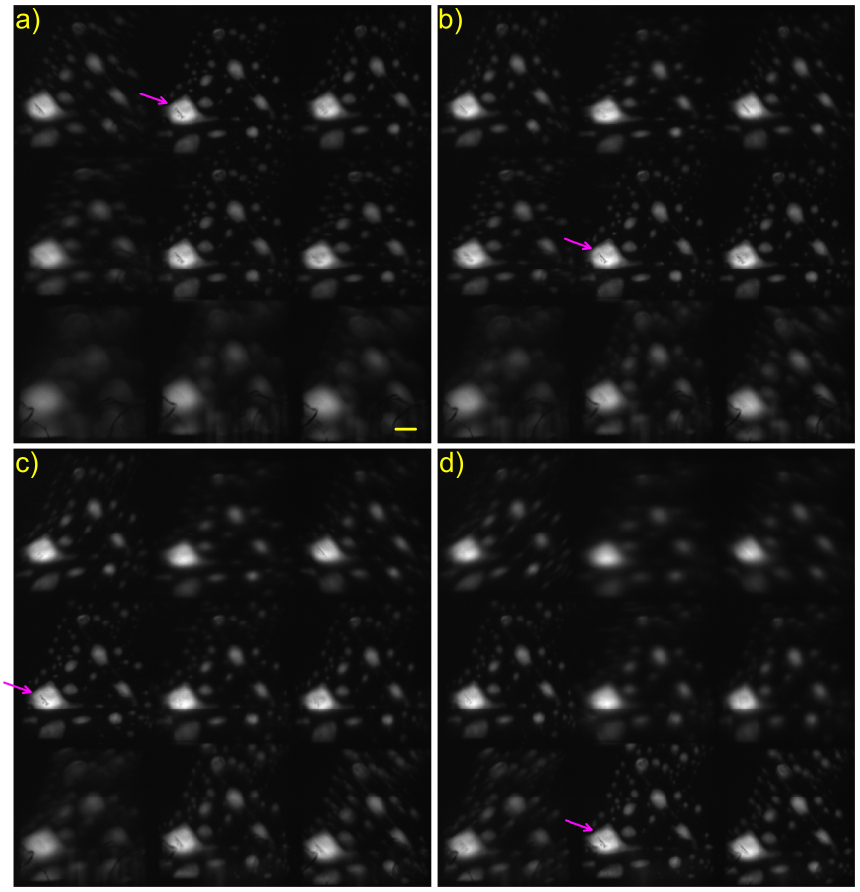

Figure 4.22.: MFM data of a thin fluorescent sample at different z-positions. Mechanical scanning was performed and here we selected four slices. The magenta arrows point at a recognizable feature which is focused in each of the slices. a) $z = z_0 - 600\,\text{nm}$ where the MF_{0-1} order is in focus. b) Focus on the MF_{00} order, *i.e.* $z = z_0$ nominal focal plane. c) The MF_{-10} order seems to be in focus for $z = z_0 + 600\,\text{nm}$. d) $z = z_0 + 1200\,\text{nm}$ where the MF_{01} order is sharp. Scale bar $5\,\mu\text{m}$.

other hand, MF_{0-1} (fig. 4.22a) and MF_{00} (fig. 4.22b) should appear in focus for a scanning of 900 nm.

In fig. 4.23 we display our preliminary MFM result imaging a sample consisting of fluorescent beads embedded in agarose (Agarose standard Roti®garose, Carl Roth, Germany) (see protocol in the appendix E). Thanks to the agarose embedding, beads are localized in several planes and we thus create a 3D test sample. We could verify the homogeneous 3D arrangement of beads with a conventional scanning 3D WF microscope.

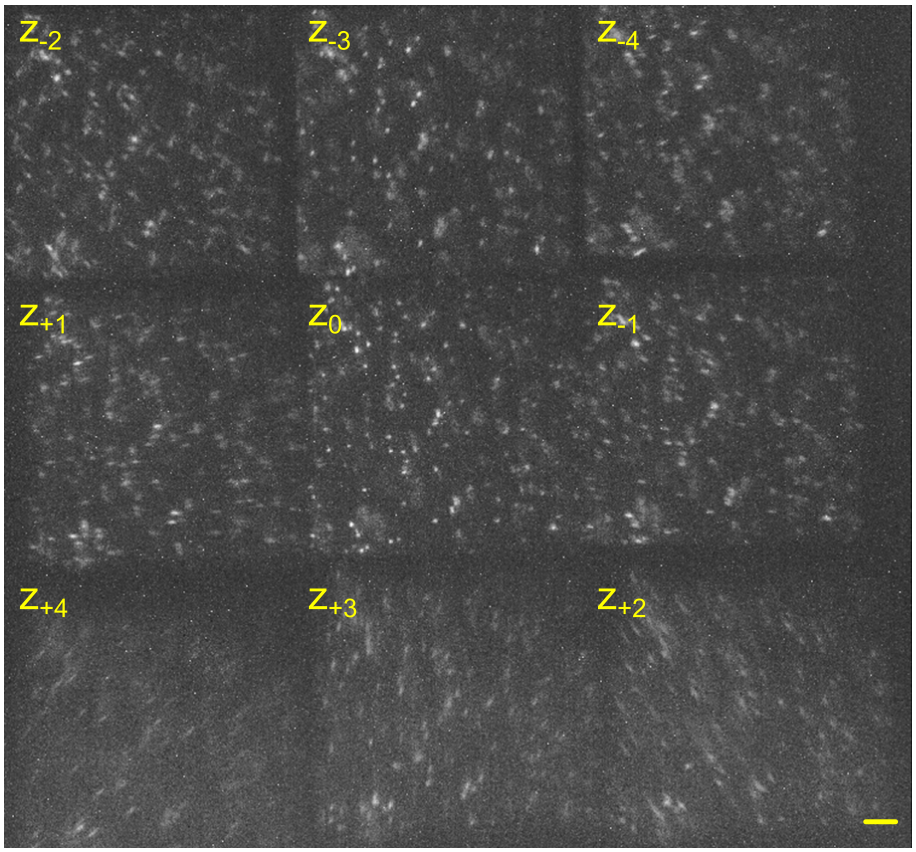

Figure 4.23.: Preliminary MFM data with the home-built microscope. The acquisition mode was WF and exposure time 200 ms at 100 % laser power. Each MF order was 400×400 pixel wide, corresponding to a FOV of 32.5 µm in x and also in y. Scale bar 3 µm

In our MFM data (fig. 4.23), we observe a strong astigmatism. The strong optical aberrations present in the system explain why:

- no focused information can be obtained in the diagonal orders MF_{-1-1}, MF_{1-1}, MF_{-11} and MF_{11} (dataset presented in fig. 4.22),
- the distance between the planes in fig. 4.22) is not as expected and
- the multifocus effect is not visible on the 3D beads sample (a different set of focused beads should be present in each of the MFM orders in fig. 4.23).

These results show that there is, despite our best effort, a misalignment in the system. The alignment of the MFM detection scheme on a home-built microscope is very delicate and requires high-precision tools.

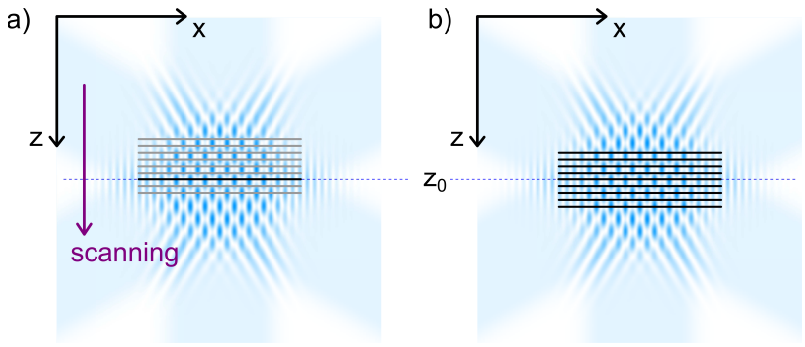

Figure 4.24.: Fundamental imaging difference between scanning three-beam SIM and MF-SIM. a) Sequential imaging of several planes: here, the third plane lies in the nominal focal plane z_0 and can be imaged. The purple arrow depicts the direction of the scanning in z, thus bringing every plane of interest sequentially in focus for imaging. In other words, the sample is scanned through the illumination pattern. Therefore, the illumination is fixed with respect to the nominal focal plane z_0. b) Simultaneous acquisition of nine focal planes with MF-SIM: in this case, the pattern is fixed with respect to the object. This has strong implications on the theoretical description of both cases.

4.4. Reconstruction of MF-SIM data

The MF-SIM data shown in this section were acquired with the Elyra SIM illumination as presented in section 4.2.

4.4.1. The challenge

The raw MF-SIM data looks similar to a 3D stack of three-beam SIM images, but there is a major difference since the sample is not moving with respect to the illumination pattern. Fig. 4.24 depicts this fundamental difference between the scanning three-beam SIM approach and the MF-SIM case.

The consequence of this fundamentally different way to image the sample has implications in the theoretical formulation of the problem [22].

Let us express the three dimensional illumination pattern $I_{illu}\left(\boldsymbol{r_{xy}}, z\right)$ as a sum of components, each of which can be separated into a term which depends only on the axial coordinate $I_m(z)$ and a term dependant on the lateral coordinates $J_m(\boldsymbol{r_{xy}})$ [22]:

$$I_{illu}\left(\boldsymbol{r_{xy}}, z\right) = \sum_{m} I_m(z) \cdot J_m(\boldsymbol{r_{xy}}) \tag{4.11}$$

where m is the index of the SIM order, *i.e.* in our case of three-beam SIM $m = 0..2$. It should be noted that all $J_m(\boldsymbol{r_{xy}})$ are harmonic functions (see each individual term of eq. 1.12 and eq. A.1).

If the illumination is fixed with respect to the nominal focal plane z_0 (fig. 4.24a), then the contribution in z of the illumination pattern can be expressed in the OTF of the first SIM order [22]:

$$I_{det} = \sum_{m} (h \cdot I_m) \otimes (\rho \cdot J_m) \tag{4.12}$$

with the usual variables for the PSF and sample information as introduced in eq. 1.4.

In other terms, the OTF for the 1^{st} SIM orders gets duplicated in z (middle column of fig. 4.25a) simply due to the scanning [22]. The shift of the information in Fourier space which is responsible for the axial resolution enhancement comes from the fact that the illumination is fixed with respect to the nominal focal plane z_0. Since this is not the case for MF-SIM, eq. 4.12 is not applicable. Hence, the OTF for the 1^{st} SIM orders still is the WF detection OTF, but the zero order of the detection gets separated in k_z (middle column of fig. 4.25b). Since in the MF-SIM case the same equations are not valid as in the scanning 3D SIM case, the same approach for 3D reconstruction cannot be applied. Thus, the MF-SIM reconstruction needs to find another approach to reach the extended 3D SIM OTF (see for example fig. 1.9d) as the equivalent OTF of the final image.

Remarks considering the z-sampling. One should also notice that, due to the extension of the 1^{st} order OTF in the scanning 3D SIM approach, the sampling in z should be adjusted according to the Nyquist criterion (modified according to eq. 4.8) [104]. For a WF microscope with highest transmittable z-frequency $k_{z,max}$ (see eq. 1.8), the correct z-sampling distance is of the order 300 nm (see eq. 1.9). In scanning 3D SIM, the distance between the acquired planes is twice smaller than what the WF axial Nyquist limit in order to compensate for the extended OTF

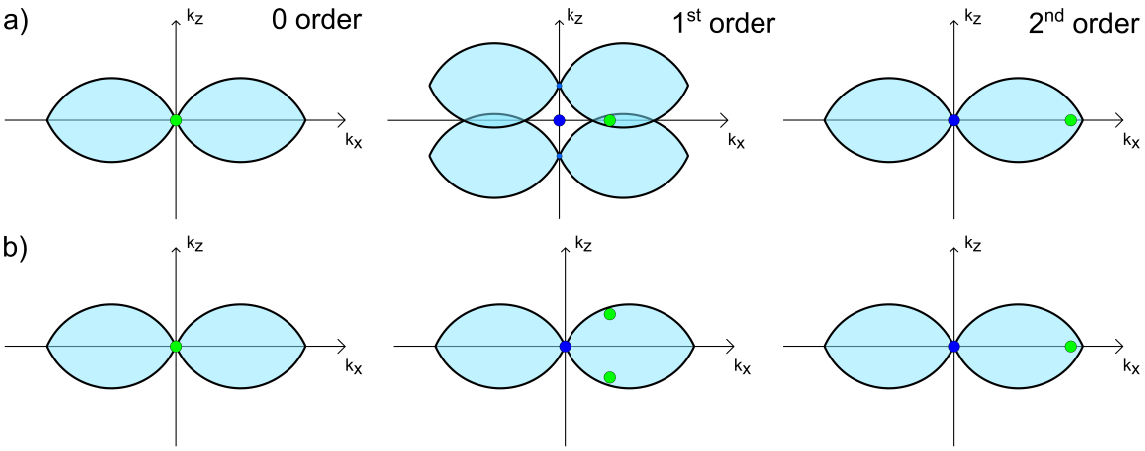

Figure 4.25.: Separated, unshifted orders. Green spot: zero object frequency. a) Sequential imaging of several planes. Middle column (1^{st} order): As explained in eq. 4.12, the axial modulation can be expressed in the OTF directly since there is an automatic demodulation of each pair of first orders during the scanning, hence the 1^{st} order doubled OTF. b) MF-SIM case: the defocusing is on the detection side and therefore inherently part of the sample. Thus the green spots in the 1^{st} order correspond to $\rho\left(\boldsymbol{r_{xy}}\right) \cdot \sin\left(\Delta k_z z\right)$.

support along k_z. If we take the same example as in eq. 1.9, an axial sampling of ~150 nm is required to correctly sample an OTF support which is extended to $2 \cdot k_{z,max}$ (see fig. 1.9d). Thus, twice as many planes are imaged and acquired to cover the same z-extent (fig. 4.24a is therefore not exactly correct since there should be extra planes in between those which were drawn). This also has consequences on the volumetric acquisition time.
In MF-SIM on the other hand, since there is only one WF detection OTF (see fig. 4.25b, middle), the distance between the imaged planes, which is defined by the design of the MFG, only needs to correspond to the WF sampling. The correct sampling in the reconstructed result will be introduced by intrapolation in between the acquired planes, as it is done in x, y in all SIM reconstruction approaches.

It is possible to check using simulations that every out-of-focus fluorophore will be excited by the illumination pattern in one of the 15 lateral shifts of the grating even without axial scanning. However, there will be no modulation along z if there is also no scanning of the pattern along z. It seems therefore difficult to separate top and bottom first orders which inherently have the same phase when using a symmetrical diffraction grating (see fig. 4.26).

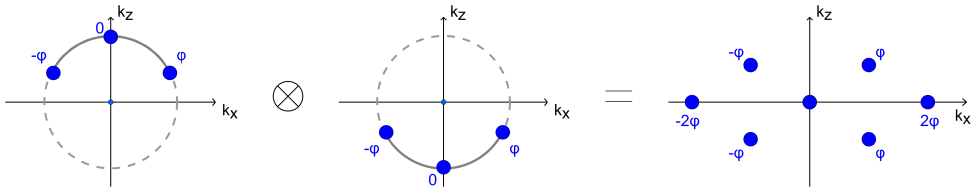

Figure 4.26.: Phases in the amplitude and intensity orders in three-beam SIM. Diffraction on a symmetric grating leads to the phases in the $\pm 1^{st}$ diffraction orders (amplitude) being exactly opposite, denoted here respectively $\pm\varphi$ [105]. Here for simplicity we take the phase in the zero order (offset) as being 0. After convolution with the complex conjugate, the 7 intensity orders have phases as depicted (right sketch). Each of the two pairs of 1^{st} orders at $\pm k_{z,max}$ always have the same phase. When acquiring a single slice, these pairs are projected on the $k_z = 0$ axis, thus leading to 5 SIM orders that are necessary to separate by lateral shifting of the grating. However, when the sample is scanned as in the classical 3D SIM approach, the information is automatically shifted in Fourier space. No further reconstruction step is necessary to separate these pairs of order and produce the extended OTF support, just an adequate z-sampling to avoid aliasing.

4.4.2. Reconstruction approach and results

A first naive approach consists in reconstructing sequentially each individual plane with a 2D SIM reconstruction approach enabling optical sectioning, for example PEM with zero order suppression (see section 3.1.1) or *thick slice* blind-SIM (see section 3.1.2) [32].
However, this does not give satisfactory results and cannot lead to a real resolution enhancement in z.

The solution we developed is based on a 3D deconvolution with known 3D illumination pattern, and it is described step by step in the following.

Step 1: pre-processing. First, background subtraction and if necessary flat fielding and denoising are applied to the raw data. Then, the 15 raw images (see for example fig. 4.5), *i.e.* 15 images of size 2048×2048 pixels (full camera chip sensor), are first cropped so as to roughly extract each of multifocus (MF) orders. In the case of the raw data presented in fig. 4.5 which serve here for the purpose of demonstration, the chosen optics and the optical alignment led to the sensor being not optimally used and each MF order being 340×340 pixels wide. We therefore have at this stage 15 series of nine 340×340 frames.

Each family of nine frames does not yet correspond to a 3D stack because of the distortions introduced to each MF order through an imperfect optical alignment, slightly different optical path for each MF order since they pass different portions of the MFM components. The registration toolbox flexible algorithms for image registration (FAIR) [106] is used to align the 9 slices. It is applied to the WF data (average of all 15 raw SIM data for each plane) and needs to be characterized only once. Then, if the optical system remains unchanged, the calibrated registration transform can be applied to the data directly.
As a result, at the end of step 1 we have 15 aligned 3D MF-SIM stacks. We can still apply, if necessary, a drift correction between the grating directions using the usual cross-correlation approach [37].

Step 2: PEM processing of the middle slice and grating parameters estimation. The central slice of the stack, *i.e.* to the MF_{00} order, corresponds to the 2D image in a normal WF detection scheme and can be processed as such. We use the PEM software because it enables to estimate the grating parameters (grating constant for each orientation, global lateral and axial phase, as well as relative phase step in each raw SIM frame in the MF_{00} order) [37]. These parameters are the output of step 2. The quality of the reconstructed SIM image is nonetheless an indication whether the reconstruction worked at all, and is presented in fig. 4.27b. The lateral resolution enhancement and a certain extent of optical sectioning are visible by comparing to the 2D WF deconvolution in fig. 4.27a, thus confirming that PEM performed well and we can trust the parameters that PEM indicates to us.

Step 3: Calculation of the 3D illumination pattern. Based on the knowledge of the grating parameters as found in step 2, we can calculate the 3D illumination pattern $I_{illu,l}$ using following formula:

$$\begin{aligned} I_{illu,l}(\mathbf{r}_{xy}, z) = 1 &+ m_1 \cos\left(\mathbf{k_g r}_{xy} + \theta_l\right) \cdot \cos\left(k_{z,height} \cdot z + \theta_z\right) \\ &+ m_2 \cos\left(2\mathbf{k_g r} + 2\theta_l\right), \end{aligned} \tag{4.13}$$

where $\mathbf{r}$, $\mathbf{k_g}$ and θ_l were defined when the two-beam illumination pattern (eq. 1.12) was defined in section 1.2.2. $\mathbf{z}$ is the vector of axial coordinates. In the sum, there are three terms corresponding to the zero, first and second SIM orders. $k_{z,height}$ was introduced in eq. 3.3 and θ_z is the global axial phase.

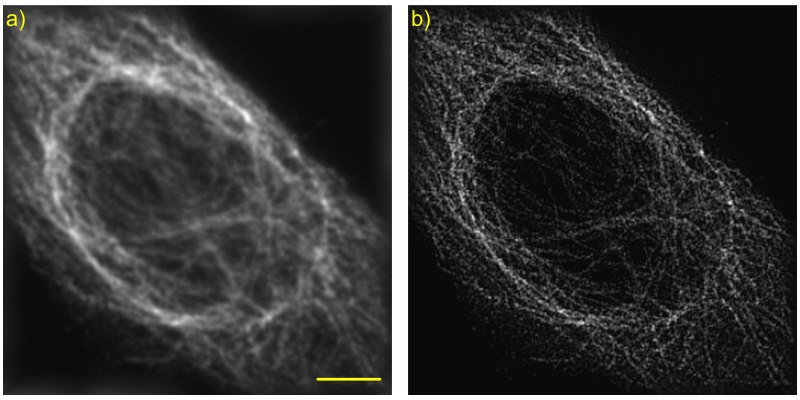

Figure 4.27.: Step 2 of the MF-SIM reconstruction. a) 2D deconvolution of the WF image of the middle slide, obtained by averaging the 15 images in the MF_{00} order. This corresponds to the 2D WF image of an unmodified epifluorescence microscope. b) PEM processing in 2D of the 15 raw SIM images in the MF_{00} order. The lateral resolution is improved and the out-of-focus light is partially rejected. This figure serves in the processing routine only as a quality estimation of the performance of step 2, but it is not used further. The scale bar is 3 µm.

We see that the distance between the MF planes Δz should be well known and constant. This is not always simple in practice. If Δz is not correct or if the registration was not precise, then the calculated pattern will not exactly overlap with the pattern that indeed excited the sample and the next reconstruction step will fail. For this dataset, we estimated Δz to be 80 nm. It should be stressed that this corresponds to a massive oversampling in z. It is due to the fact that the MFG used was custom-designed for the experimental parameters of the home-built system (see section 4.3) which are slightly different from the Elyra (see section 4.2).

An illustration of the calculated grating can be found in fig. 4.28.

It is possible to make a visual inspection in zones of the sample where the fluorophore density is rather high and where the fringes are in focus (out-of-focus features will still be visible and also be modulated but they should not be used for this visual inspection) to check whether the overlap is good, for all grating phases and orientations as well as for all slices containing focused information. The visual inspection allows us to adjust the value of θ_z.

Step 4: 3D deconvolution with known pattern. The blind-SIM algorithm presented in chapter 3 is only one specific feature of a MATLAB package that we call the generic deconvolution toolbox. The generic deconvolution toolbox enables also

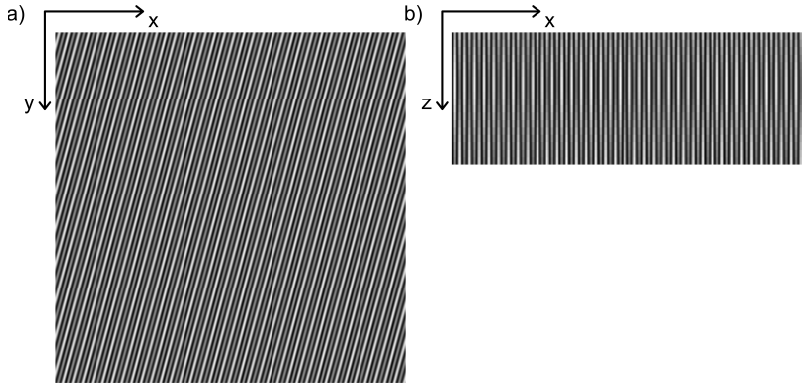

Figure 4.28.: Step 3 of the MF-SIM reconstruction. The 3D illumination pattern $I_{illu,l}$ is calculated using the result of step 2, the known distance between the MF planes Δz and eq. 4.13. a) $x-y$ view for $l=1$ (the first of the 15 illumination patterns) and $z=z_0$, the nominal focal plane corresponding to the MF_{00} order. b) $x-z$ view. In this dataset, we estimated $\Delta z = 80\,\mathrm{nm}$, which corresponds to a sampling z much finer than what is indicated by the Nyquist criterion for 3D WF.

to perform deconvolutions - in 2D or in 3D - using the known illumination $\{I_{illu,l}\}$ as an input, with respect to the blind estimation which estimates and outputs $\{I_{illu,l}\}$. We estimate ρ using a maximum likelihood approach by minimizing

$$F(\rho) = \sum_{l=1}^{L} \left| \left[\rho \cdot I_{illu,l}\right] \otimes h - I_{det,l} \right|^2 \tag{4.14}$$

and by using the known illumination patterns $\{I_{illu,l}\}$ calculated in step 3 thanks to eq. 4.13. The 3D PSF h is, in this case, calculated based on the experimental parameters, but an experimental PSF, obtained for example by imaging a sparse sample of sub-diffraction fluorescent beads, could be used. The data is oversampled of a factor of 2 along z. Theoretically, a re-sampling is also applied in x, y to avoid aliasing of the extra lateral frequencies in SIM. However, for this dataset we observed such a small lateral resolution enhancement that this was not necessary. The final reconstructed MF-SIM image is depicted in fig. 4.29.

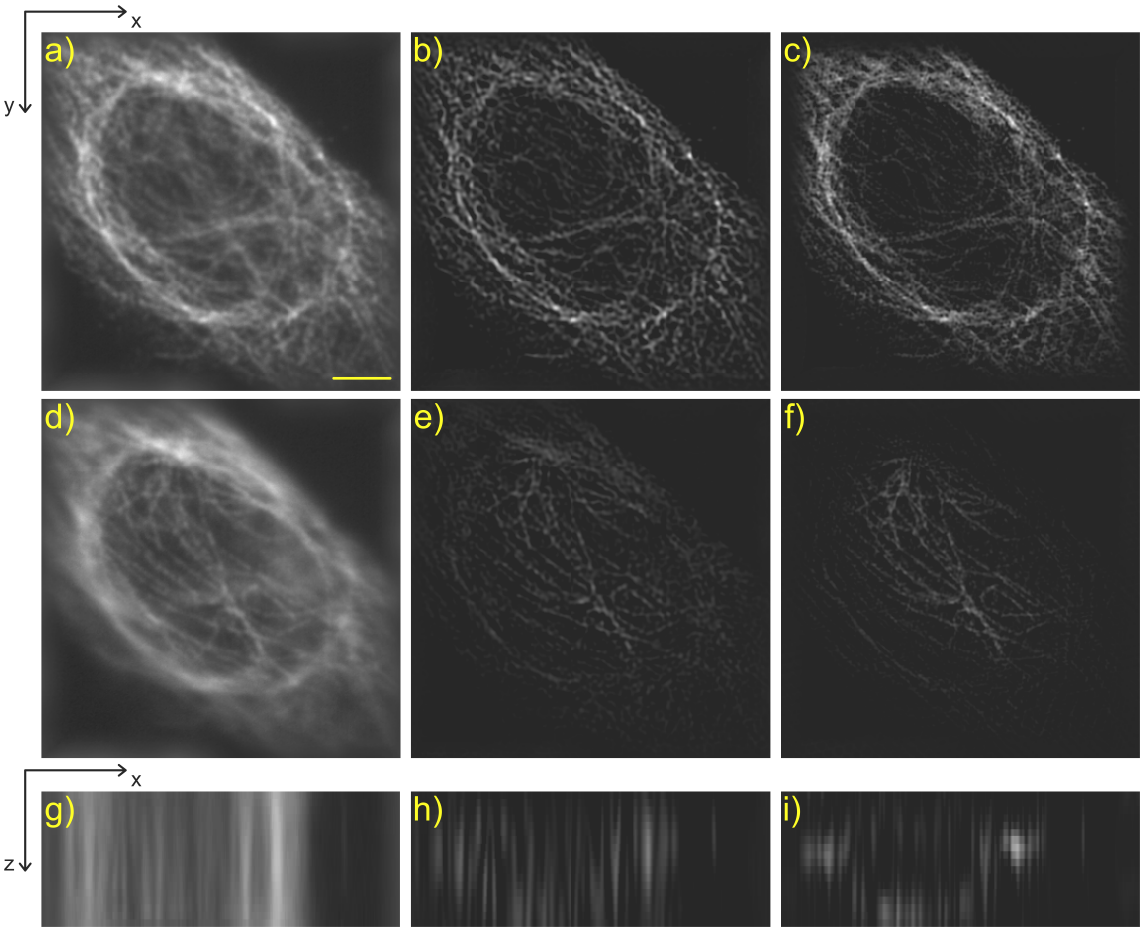

Figure 4.29.: Step 4 of the MF-SIM reconstruction and final MF-SIM result (c), f) and i)). As a comparison, the 3D WF image (a), d) and g)) after the registration process in step 1 shows low lateral resolution and a strong out-of-focus. A second comparison can be done with the 3D deconvolved WF image (b), e) and h)) *i.e.* the 3D WF image deconvolved by using the calculated PSF. It is visible that the 3D WF deconvolution already enhances the image quality in terms of contrast by removing a significant part of the out-of-focus blur. a), b) and c) display the middle slice corresponding to the MF_{00} order at $z = z_0$. d), e) and f) correspond to the bottom slice of the MF stack at $z = z_0 + 4\Delta z$ imaged in the MF_{-11} order (see the z_{+4} plane in fig. 4.5). g), h) and i) $x - z$ views where the optical sectioning of the 3D WF deconvolution in h) can be appreciated, as well as the extra resolution enhancement in z as shown in i). The scale bar is 3 µm.

4.5. Discussion of the experimental work

In order to improve the acquisition speed of three-beam SIM, we combined it with a multifocus detection scheme. Using a commercial instrument, the ELYRA-PS.1

(Carl Zeiss Microimaging, Germany), we acquired proof-of-principle MF-SIM data of biological test samples, albeit with non optimal acquisition parameters. Due to the low number of collected photons leading to long required exposure times, we can neglect the influence of ROI size on the readout time and hence on the acquisition speed. Thus, MF-SIM has a volumetric acquisition speed improvement factor which is 18×, if we consider only the hardware timings. Taking into account the photon losses leads to the fact that for the same intensity on the sample, the same SNR can be reached with MFM detection for a 20× longer exposure. Thus, the speed of MF-SIM is in practice levelled with that of 3D scanning SIM. A second advantage however is the absence of required mechanical scanning along z, which is a source of artefacts since it can lead to drift and vibrations. The acquired data enabled us to develop and demonstrate a novel reconstruction approach for MF-SIM. The reconstructed 3D image demonstrates enhanced lateral and axial resolution with respect to 3D WF microscopy.

It is however desired to attach the MFM module to a home-built SIM system for two reasons:

- We can better control the acquisition parameters: triggering, 4f configuration, design matching between MFG and the detection optics used, correct z-sampling;
- Reaching a real improvement of the acquisition speed is not feasible with the ELYRA microscope because the used components, *e.g.* a mechanical grating, do not enable optimal frame rate, as mentioned in section 1.3.

We therefore built a SLM-based three-beam SIM set-up which has a maximal, hardware limited speed of 6.35 Hz (see appendix F). This figure corresponds to the acquisition of a MF-SIM image, *i.e.* 15 SIM frames leading to a volume of nine slices. It does not take into account the fact that real samples need to be exposed for a longer time.
For this experimental work, we used a ferroelectric SLM, we studied and adjusted the polarization control and we optimized the synchronization sequence. The acquired data demonstrate the lateral resolution improvement of a three-beam SIM set-up. However, we were not able the acquire MFM data nor MF-SIM data with our home-made system. The main limitation of the SLM-based SIM set-up is the extremely

low light efficiency. Indeed, only ~0.5 % of the laser light reaches the sample. Since the MFM itself also has a low light efficiency of ~50 %, the realistically required integration time is by far higher than what was used for the experiments with the ELYRA.

In our system, the component leading to highest loss is the SLM. As explained in section 4.3.2, because of the 34° angle between the fast axes of the SLM ON and OFF states (see fig. 4.10), we measure only 7 % in front of L_2 (see fig. 4.6) in all orders with respect to the power at the output of the laser. The necessity of filtering the many unwanted orders (see fig. 4.7) leads to a measured overall efficiency of 2.8 % right after the order selection aperture.
The next major loss of light comes from the passive segmented azimuthal polarizer, after which we measure 1.2 %. After the remaining optical components, in particular the dichromatic reflector and the objective, we measure an overall throughput of 0.5 %.

We designed and implemented an alternative using a segmented QWP (see fig. 4.30). The input polarization should be circular for all orders, *i.e.* the set-up is not modified until the order selection aperture. The geometry is similar as the azimuthal polarizer (see inset in fig. 4.6) but each segment consists of a QWP foil made of mica (283/815, Spruce Pine Mica, USA). The advantage is that there is theoretically no loss since the QWP converts the whole electric field into the linear polarization at 45°. On the other hand, the component made of segments of linear polarizer throws away half of the light. Therefore, we expect a twice better energy throughput. In practice, we measure an improvement of a factor 1.5. The discrepancy with theory can be explained by different sources of errors: the Fresnel reflection with the mica, a non perfect transmission of the mica foil, a non perfect extinction ratio, and an unknown characterization wavelength.

A significant improvement can only be reached by exchanging the ferroelectric SLM for another SLM with higher diffraction efficiency, which would come at the cost of reduced update rate. An alternative is to use galvo-scanning devices.

Finally, the laser wavelength of 488 nm we use is not ideal since a huge majority of laser manufacturer reach a maximal power of 200 mW. Investing in a very expensive equipment (Genesis CX488-4000, Coherent, USA) or compromising on the wavelength could be beneficial. For instance, the usual green fluorophores can still be reasonably

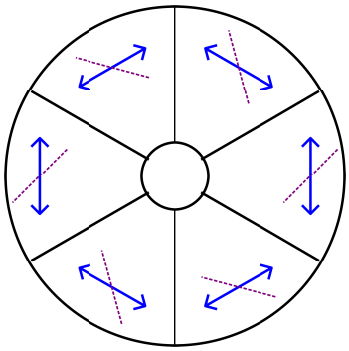

Figure 4.30.: Segmented QWP. In each segment, the fast axis of the QWP (purple) is oriented so that it is at 45° of the desired output polarization (blue).

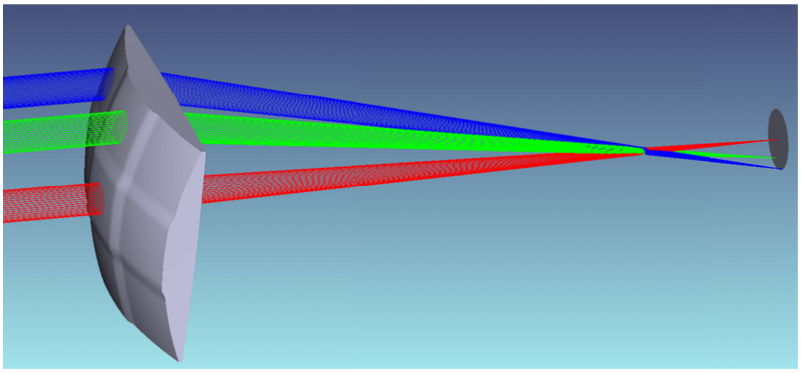

Figure 4.31.: Multi-lens array design: 3D layout and three example beams.

well excited at a wavelength of 473 nm, where lasers with higher specified output power are available.

On the MFM side, there is also a loss of light due to the numerous optical components. The diffraction efficiency of the MFG can be optimized but is already really close to the theoretical limit (see section 4.1.1). As an indication, a 20× longer integration time is needed on the MFM arm than with the camera placed in the first image plane for reaching a comparable SNR. To reduce the number of surfaces in the MFM scheme, we designed a multi-lens array which acts as a component that keeps the order separation and focuses them. It could therefore replace the multifaceted prism and the last lens in front of the camera. At the moment, the multi-lens array is designed (see fig. 4.31) but needs now to be manufactured and tested.

5. Conclusion and outlook

Structured Illumination Microscopy (SIM) is an imaging technique that owes its success to its high resolution combined with good acquisition speed. Its wide application to complicated, for instance thick or highly scattering, samples has been hampered by the challenging data reconstruction. We explored means to improve the performance of SIM along two main directions.

First, we contributed to the development of a new class of algorithm, referred to as blind-SIM, that enables an artefact-free reconstruction of the sample information even in cases where the illumination pattern was distorted. With our developed *thick slice* blind-SIM algorithm, we demonstrated that a single slice of interest can be acquired and processed, even in the presence of strong out-of-focus light and distortions of the illumination pattern, without the necessity to acquire a 3D stack of data.

Collaborative work on reconstruction issues shows that the demand for the blind-SIM algorithm, containing the *thick slice* blind-SIM feature, is high. Indeed, users of the SIM technique, irrespective of whether their system was bought from one of the major manufacturers or whether it was home-built, possibly at an imaging facility, often encounter difficulties with the SIM processing. In order to meet with the demand, we intend to develop a user-friendly blind-SIM package that can be distributed. A wide dissemination is however unlikely due to the fact that the deconvolution-based approach remains very computationally expensive and slow in the present form. Development of blind-SIM in another programming language than MATLAB should be realized.

Furthermore, we have not processed 3D SIM data (as acquired by a standard z-scanning approach) with blind-SIM so far. A 3D blind deconvolution requires several OTFs, as can be seen in fig. 4.25a. Work on a multi-view approach, using a doubled

OTF (middle column of fig. 4.25a) for the coarse illumination pattern and the normal WF OTF for the fine illumination, is in progress.

The second direction of improvement that we inquired concerns the acquisition speed of SIM. We inspired ourselves from an existing design using a ferroelectric SLM for three-beam SIM and combined it with a multifocus detection (MF-SIM). The proof-of-principle experiment was performed using a commercial SIM system and enabled us to successfully develop and demonstrate this novel imaging modality. The processing of MF-SIM data uses a deconvolution-based approach but at the moment, still requires the knowledge of the illumination pattern. A next step is to implement the MF-SIM reconstruction with blind estimation of the illumination pattern. This would avoid the time-consuming and non-reproducible adjustment of certain parameters, like the z-sampling and θ_z phase, which is currently done by visual inspection.

The work on the home-built system enables to conclude that, in order to enhance the speed of a 3D SIM microscope, the choice of components should not only be directed by their pure, hardware-limited, operating speed, but also by taking into consideration the induced loss of light as well as practical experimental difficulties like the precision of the available opto-mechanical components. We discussed ideas to improve the light throughput of our system in section 4.5.

Appendices

A. Illumination pattern in three-beam case

For the three-beam case, the periodic function of the two-beam case (see eq. 1.12) is overlapped with a periodic function of half period $\mathbf{k_g}/2$. Furthermore, these two periodic function do not have the same contrast, therefore we introduce here the contrast parameters m_1 and m_2. Finally, here for this appendix we change the notation and we take $2\mathbf{k_g}$ the period of the periodic function for the two-beam case and therefore the three-beam case function contains two frequencies $2\mathbf{k_g}$ and $\mathbf{k_g}$:

$$\begin{aligned} I_{illu,l}(\mathbf{r}) &= 1 + m_1 \cos\left(\mathbf{k_g}\mathbf{r} + \theta_l\right) + m_2 \cos\left(2\mathbf{k_g}\mathbf{r} + 2\theta_l\right) \\ &= 1 + \frac{m_1}{2}\left(e^{i(\mathbf{k_g}\mathbf{r}+\theta_l)} + e^{-i(\mathbf{k_g}\mathbf{r}+\theta_l)}\right) \\ &+ \frac{m_2}{2}\left(e^{2i(\mathbf{k_g}\mathbf{r}+\theta_l)} + e^{-2i(\mathbf{k_g}\mathbf{r}+\theta_l)}\right), \end{aligned} \tag{A.1}$$

In Fourier space, eq. A.1 becomes:

$$\begin{aligned} \tilde{I}_{illu,l}(\mathbf{k}) = \delta(\mathbf{k}) &+ \frac{m_1}{2}e^{i\theta_l}\delta\left(\mathbf{k} - \mathbf{k_g}\right) + \frac{m_1}{2}e^{-i\theta_l}\delta\left(\mathbf{k} + \mathbf{k_g}\right) \\ &+ \frac{m_2}{2}e^{2i\theta_l}\delta\left(\mathbf{k} - 2\mathbf{k_g}\right) + \frac{m_2}{2}e^{-2i\theta_l}\delta\left(\mathbf{k} + 2\mathbf{k_g}\right). \end{aligned} \tag{A.2}$$

B. Aberrations and the sum condition

This appendix has been published in [32]. More specifically, the appendix to the published article [32] is reproduced here (the formalism in the equations was adapted for consistency). Reprint permission according to the CC-BY license.

In situations where we want to apply our blind SIM algorithm, we can assume that the aberrations are relatively minor and a single parallel beam would not lead to significant brightness variations or otherwise only to relatively coarse brightness changes resulting a similarly modified deconvolution result. By now interfering two or more beams, of locally always correct phase steps, we can show that the incoherent sum of all coherently interfering waves leads to equal brightness which, in the worst case again, will lead to slightly wrong reconstructed sample brightnesses. However, in situations of deep tissue imaging with fully developed speckles, this assumption does not hold, however this is not the application that blind-SIM is targeted for. In the following, we assume that we are in the single scattering regime, there are only few refractive surfaces, no fully developed speckles, which means that the intensity is relatively smooth although the phase distortions can reach several multiples of π. The aberrations foremost affect the relative phase of the interfering beams. This seems justified when only a few cell layers are illuminated and without large refractive index difference and little absorption. As demonstrated below, even complicated phases still average out.

We have three beams corresponding to the zero and two first amplitude orders of a diffraction grating. We index the amplitude order with the letter a. In the SIM configuration, they are plane waves in the sample space.

$$E_a(\boldsymbol{r},t) = |E_a| \cdot e^{i\left(\boldsymbol{k}_a \cdot \boldsymbol{r} - \omega t + \phi_{a,l} + \chi_a(\boldsymbol{r})\right)}, \tag{B.1}$$

with $a = -1, 0$ or 1 and where

$$\phi_{a,l} = a \cdot \frac{l}{L} 2\pi, \tag{B.2}$$

for $l = 1..L$ (L equidistant phase steps). $\phi_{a,l}$ is a constant phase term determined by the diffraction grating and which can be changed by translating the grating. The aberration term is modelled as a phase term $\chi_a(\boldsymbol{r})$. This function describes the deformation of the wavefront and varies smoothly with position. However, it does not depend of the order phase step $\phi_{a,l}$. The aberration map for the two first orders are generally different from one another, as the beams do not traverse the same part of the sample. However the phase terms are maintained (caused by the shift of a diffraction grating).

The light intensity at a position $\boldsymbol{r}$ is the interference of all electric field order contributions at this spot. In the SIM case, each intensity order is the result of the interference of two amplitude orders (except for the zero order for which phase contributions cancel out). Here we denote these two orders a and b, which can each be $-1, 0$ or 1. Their interference can be written in the following way:

$$E_a \cdot E_b^* = |E_a||E_b| \cdot e^{i(\boldsymbol{k}_a - \boldsymbol{k}_b)\cdot \boldsymbol{r}} \cdot e^{i(\omega-\omega)t} \cdot e^{i(\chi_a(\boldsymbol{r}) - \chi_b(\boldsymbol{r}))} \cdot e^{i\left(\phi_{a,l} - \phi_{b,l}\right)}. \tag{B.3}$$

When we sum over all L patterns we obtain for interferences between any two different orders a and b:

$$\sum_{l=1}^{L} E_a \cdot E_b^* = |E_a||E_b| \cdot e^{i(\boldsymbol{k}_a - \boldsymbol{k}_b)\cdot \boldsymbol{r}} \cdot e^{i(\chi_a(\boldsymbol{r}) - \chi_b(\boldsymbol{r}))} \cdot \sum_{l=1}^{L} e^{i\left(\phi_{a,l} - \phi_{b,l}\right)} = 0. \tag{B.4}$$

Sums out to zero since the phase steps are chosen to be equidistant, for example in the case where we have three equidistant phase steps:

$$\sum_{l=1}^{L} e^{i\left(\phi_{a,l} - \phi_{b,l}\right)} = \sum_{l=1}^{L} e^{i\left(a \cdot \frac{l}{L} 2\pi - b \cdot \frac{l}{L} 2\pi\right)} = e^{i \cdot \frac{2\pi}{3}} + e^{i \cdot \frac{4\pi}{3}} + e^{i \cdot 2\pi} = 0. \tag{B.5}$$

In this case taking the example of a=1, b=0 and L=3 for the sake of demonstration. Note also, that only the contributions for a=b do not cancel, which thus results in illumination being well described as constant to a good approximation.

C. Selection of useful MATLAB functions

In the following, the code for creating the blind-SIM mask.

```
% Creates a Fourier Transform mask for the illumination by clicking on the FT of the illumination (first phase image for each direction)
%
% INPUTS:
% data: Fourier Transform of the illu
% radius: radius of the mask in number of pixels. Default 5
% nb: number of orders (number of clicks). Default 1
% numDir: number of directions. Default 3
% numPhases: numbre of phase shifts per direction. Default 3
% userft: if 1, the mask will be created in half complex space. Default 1
% sZ: number of slices in the mask (extra slices will be empty). Default 1

function resMask=clickMask(b,radius,nb,numDir,numPhases,userft,sZ)

%Default values
if nargin<2
    radius=5;
end
if nargin<3
    nb=1;
end
if nargin<4
    numDir=3;
end
if nargin<4
    numPhases=3;
end
if nargin<4
    userft=1;
end
if nargin<5
    sZ=1;
end

% Preparation
asize=size(b); sX=asize(1); sY=asize(2);
mymask=newim([sX sY]); resMask={};

for d=1:numDir
    n=d-1;
    % Create autocorrelation image
    offs=n*numPhases; % offset enables to choose the direction
    han=dipshow( abs(b(:,:,offs)).^0.3) %display
    % click on the correlation spot
    fprintf('********Pick the highest frequency peak! ***********\n')
    mycoords=dipgetcoords(1);
    if nb>1 %more than 1 order, for example three-beam SIM
        fprintf('********Pick the lowest frequency peak! ***********\n')
        mycoordsL=dipgetcoords(1);
```

```
    end
    mid=floor(asize(1:2)/2); %Middle coordinate is zero in k space
    diffvec=(mycoords-mid); %2nd order
    if nb>1
        diffvecL=(mycoordsL-mid); %1st order
    end
    mycoords2=mid-diffvec; %mirrored position 2nd order
    if nb>1
        mycoords2L=mid-diffvecL; %mirrored position 1st order
    end

    if nb>1 && sZ>1 %thick slice
        global kmax %these are calculated externally
        global kmaxz

        k0=sqrt(diffvecL(1,1).^2+diffvecL(1,2).^2); %Period of the coarsest grating in pixels
        k0normed=2*k0/kmax; % Normalize the Ewald sphere to 1 in x,y
        myHeight=round(kmaxz * (1-sqrt(1 - k0normed*k0normed'))); %to undo the effect of the normalization, use here the z-scaling
    end

    mypoints=cat(1,mid,mycoords,mycoords2); %List of points 2nd order
    if nb>1
        mypointsL=cat(1,mycoordsL,mycoords2L); %List of points 1st order
    end
    mymask=GenMask(mypoints,radius,[sX sY]); %Generate the mask
    if nb>1
        mymaskL=GenMask(mypointsL,radius,[sX sY]); %Generate the mask. 1st order
    end
    if userft
        mymask=fft2rft(dip_image(ifftshift(double(mymask))));  % fft-shifts and converts to rft style
        if nb>1
            mymaskL=fft2rft(dip_image(ifftshift(double(mymaskL))));  % fft-shifts and converts to rft style
        end
    end
    for p=1:numPhases
        if sZ>1
            resMask{numPhases*n+p}=newim([size(mymask,1) size(mymask,2) sZ]);
            resMask{numPhases*n+p}(:,:,0)=mymask; %First slice: high frequency order
            if nb>1
                if (myHeight-1)<1
                    resMask{numPhases*n+p}(:,:,0)=mymask+mymaskL; %Some slices away: low frequency order
                else
                    resMask{numPhases*n+p}(:,:,myHeight-1)=mymaskL; %Some slices away: low frequency order
                end
            end
        else
            resMask{numPhases*n+p}=mymask; %Final mask
            if nb>1
                resMask{numPhases*n+p}=mymask+mymaskL;
            end
        end
    end
end
```

In the following, the code for calibration of the LC polarization rotator.

```
%% Finds the best voltage applied to the LC cell which leads to the highest peak/mean of the second-order correlation peak
% dataname is the name of the 3D tif file containing the data in order: phase steps > orientation > applied voltage
% NumDirs:number of directions acquired in the data
% NumPhases: number of phase steps in the acquired data
% radMask: radius of the mask where to look for the maximum. Default 10
% radIn: Inner radius of the doughnut mask where to take the mean. Default radMask*2
% radOut: Outer radius of the doughnut mask where to take the mean. Default 2*radIn
% doDisp: boolean to display certain information like the masks and the peak-to-mean vs. voltage curve. Default 1

function MeadCalib_correl(dataname,NumDirs,NumPhases,radMask,radIn,radOut,doDisp)

aa=read3dtiff(dataname); %Loads the data
sV=size(aa); %size vector
```

```

%Default values
if nargin<4
    radMask=10; %radius of the mask where to look for the maximum.
end
if nargin <5
    radIn=radMask*2; %inner radius of the doughnut
end
if nargin <6
    radOut = 2*radIn; %outer radius of the dougnut (to calculate the mean)
end

if nargin <9
    doDisp=1; %Displays the calibration curves
end

%% Get the coordinates (just once)

op=squeeze(aa(:,:,:,1)); %First voltage
bb=reshape(op,[size(op,1) size(op,2) NumPhases NumDirs]);

PeakCoords=zeros(NumDirs,2); PeakMask=[]; PeakDMask=[];

for o=1:NumDirs
    pstack=squeeze(bb(:,:,:,o-1)); %series of phase steps
    dat=DampEdge(pstack,0.2,2,1); % To avoid FFT artefacts
    allft=ft(dat); %Rough separation of the orders
    cc2=ift(ft(allft(:,:,2)) .* conj(ft(allft(:,:,4)))); %cross-correlation: second order
    [mymask PeakCoords(o,:)]=MakeSingleMask(cc2,radMask); %make a mask and save the coords
    PeakMask=cat(3,PeakMask,mymask);
    myDmask=makeDoughnutMask(PeakCoords(o,:),radIn,radOut,size(squeeze(cc2))); %make a mask in a shape of a dougnut around previous
          position
    PeakDMask=cat(3,PeakDMask,myDmask);

end

PeakMask=PeakMask>0.5; PeakDMask=PeakDMask>0.5; %Boolean mask

if doDisp
    PeakMask %visual inspection
    PeakDMask %visual inspection
end

%% Now, for all values

Kratio=zeros(NumVal,NumDirs); %init

for ii=1:NumVal %different Meadowlark voltages
    op=squeeze(aa(:,:,:,ii-1));
    bb=reshape(op,[size(op,1) size(op,2) NumPhases NumDirs]);
    for o=1:NumDirs
        pstack=squeeze(bb(:,:,:,o-1)); %series of phase steps
        dat=DampEdge(pstack,0.2,2,1); % To avoid FFT artefacts
        allft=ft(dat); %Rough separation of the orders

        cc2=ift(ft(allft(:,:,2)) .* conj(ft(allft(:,:,4)))); %cross-correlation: second order
        Kmax=max(abs(squeeze(cc2)),squeeze(PeakMask(:,:,o-1))); %max value
        Kmean = mean(abs(squeeze(cc2)), squeeze(PeakDMask(:,:,o-1))); %mean value
        PeakToMean = Kmax /Kmean; %peak to mean value
        Kratio(ii,o)= PeakToMean; %in an arrow
    end
end

if (doDisp)
    figure
    plot(Kratio(:,1),'rx')
    hold on
    plot(Kratio(:,2),'gx')
    plot(Kratio(:,3),'bx')
    legend('dir1','dir2', 'dir3','Location','Best')
end
```

```
function [mymask mycoords]=MakeSingleMask(data,radius,expn)
% data is an image where the user will be asked to click (only once). The display will be abs(b).^expn
% radius is the radius of the mask in number of pixels. Default 5
% expn: exponent for the display. Default 0.3
% resMask is a binary image

if nargin<2
    radius=5; %default radius of the mask
end
if nargin<3
    expn=0.3; %default exponent for display
end

% Preparation
asize=size(data); sX=asize(1); sY=asize(2);
b=data;
mymask=newim([sX sY]);

han=dipshow( abs(b).^expn) ; %display
fprintf('********click on the wanted center of the mask ************\n')
mycoords=dipgetcoords(1); %get coordinates by a click in the displayed image

mymask=GenMask(mycoords,radius,[sX sY]); %make a mask around this position

end
```

```
function mymask=makeDoughnutMask(pointList,radIn,radOut,asize)

% Initialization:
mymask=newim(asize);
mykernel = rr(asize)>radIn & rr(asize)<radOut; %doughnut

%Compute position:
for n=1:size(pointList,1)
    mypos=floor(pointList(n,:)+0.5);
    if numel(mypos) == 2
        if mypos(1) > 0 && mypos(1) < asize(1) && mypos(2) > 0 && mypos(2) < asize(2)
            mymask(mypos(1),mypos(2))=1;
        end
    else
        if mypos(1) > 0 && mypos(1) < asize(1) && mypos(2) > 0 && mypos(2) < asize(2) && mypos(3) > 0 && mypos(3) < asize(3)
            mymask(mypos(1),mypos(2),mypos(3))=1;
        end
    end
end

mymask=convolve(mymask,mykernel) > 0.5; %place the doughnut at the position
```

D. Home-built stage

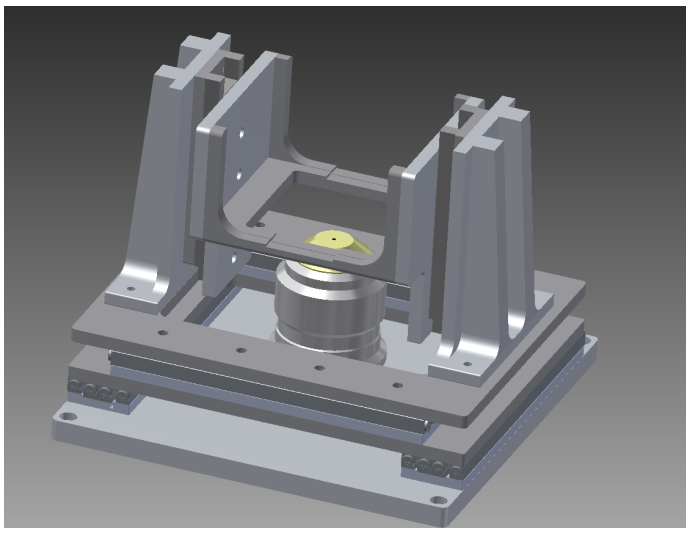

Figure D.1.: View of the home-built 3D stage. The objective is only for illustrative purpose and is not true to scale.

E. Protocol for the 3D beads sample

1. Clean a beaker and a stirring fish with ethanol.
2. Place them on the oven (130 °C) to get rid of the ethanol. After that, let the beaker cool down.
3. Place the beaker and stirring fist on the weighing machine, push the tare button, then pour in some cold tab water (approximately 15 g). The measured mass is denoted M_{wat}.
4. On a plastic cup, measure X% of agarose powder *i.e.* $M_{\text{ag}} = \frac{X \cdot M_{\text{wat}}}{100}$, where:
   - $X = 1$ leads to a transparent result,
   - $X = 2$ till $X = 3$ leads to a milky but more viscous result: the proportion should be optimised depending on the application.
   - Use standard agarose, which is more robust against high temperatures.
5. Pour the agarose powder into the beaker of cold water and quickly dissolve it.
6. Put the beaker on the oven at 150 °C with a stirring of 600 turns per minute.
7. Wait until the solution turns transparent (typically 5 min), while making that:
   - Cover with a glass or plastic petri dish to avoid evaporation and therefore reduction of the volume,
   - If bubbles appear, place the beaker in the ultra-sound bath for a short time but not too long because the liquid should not cool down.
8. When the solution is transparent, take 10 µl of a diluted (1:100 or 1:10 depending on the volume and desired concentration) beads solution and add it to the

beaker without touching the surface.

9. Put a drop of 1 µl of diluted beads on a clean coverslip and do not spread the drop but proceed with the two following steps quickly.

10. Using a 100 µl pipette, dip the pipette tip in the liquid agarose solution, let it some time to heat up and then suck in some small volume. Do not fill the pipette tip completely.

11. As fast as possible, put a drop of this agarose solution on the coverslip with the drop of beads solution and seal the sample on a microscope slide.

12. Reduce the oven to 140 °C: the solution can be kept like this for a few hours, it will stay liquid and then before the end of the day it will solidify.

13. For cleaning, use tab water.

F. Calculation of the gain in volumetric acquisition speed

The speed of the SLM-based three-beam SIM set-up can be calculated as follows:

- The shortest sequence possible with our SLM corresponds to $T_d = 100\,\mu s$.
- Assuming an extremely bright sample, we can use $N_{\text{rep}} = 1$ and use only the positive display (see fig. 4.19), thus reaching an effective exposure time of $T_{\text{eff}} = 1 \cdot N_{\text{rep}} \cdot T_d = 100\,\mu s$.
- The loading time remains $\tau = 434\,\mu s$ [97], thus the corresponding exposure time setting on the camera is $T_{\text{exp}} = T_d + \tau = 534\,\mu s$.
- For MF-SIM, we still need to illuminate the whole camera chip (or maybe a few lines less, which we neglect here) and therefore the main limitation to the speed is the readout time of 10 ms.
- The acquisition of one SIM frame thus requires in total 10.5 ms. We require 15 such frames, thus an acquisition duration for a whole MF-SIM image of 157.5 ms.

It should be noted that this corresponds to the hardware-limited speed and is indeed very unrealistic already for bright test samples like beads, all the more so for real biological samples.

Bibliography

[1] Aurélie Jost and Rainer Heintzmann. Superresolution Multidimensional Imaging with Structured Illumination Microscopy. *Annual Review of Materials Research*, 43(0):261–282, 2013.

[2] Jerome Mertz. *Introduction to optical microscopy*, volume 138. CSIRO, 2010.

[3] Lothar Schermelleh, Rainer Heintzmann, and Heinrich Leonhardt. A guide to super-resolution fluorescence microscopy. *The Journal of cell biology*, 190(2):165–175, 2010.

[4] L.M. Hirvonen and T.A. Smith. Imaging on the nanoscale: Super-resolution fluorescence microscopy. *Australian Journal of Chemistry*, 64(1):41–45, 2011.

[5] Justin Demmerle, Eva Wegel, Lothar Schermelleh, and Ian M Dobbie. Assessing resolution in super-resolution imaging. *Methods*, 88:3–10, 2015.

[6] Talley J Lambert and Jennifer C Waters. Navigating challenges in the application of superresolution microscopy. *J Cell Biol*, 216(1):53–63, 2017.

[7] Rainer Heintzmann. *Resolution enhancement of biological light microscopic data*. PhD thesis, University of Heidelberg, 1999.

[8] Joseph W Goodman. *Introduction to Fourier optics*. Roberts and Company Publishers, 2005.

[9] Rainer Heintzmann. Band-limit and appropriate sampling in microscopy. *Cell Biology: A Laboratory Handbook*, 3:29–36, 2006.

[10] Rainer Heintzmann and Gabriella Ficz. Breaking the resolution limit in light microscopy. *Briefings in functional genomics & proteomics*, 5(4):289–301, 2006.

[11] Rainer Heintzmann and Colin JR Sheppard. The sampling limit in fluorescence

microscopy. *Micron*, 38(2):145–149, 2007.

[12] Stefan W Hell and Jan Wichmann. Breaking the diffraction resolution limit by stimulated emission: stimulated-emission-depletion fluorescence microscopy. *Optics letters*, 19(11):780–782, 1994.

[13] E. Betzig, G.H. Patterson, R. Sougrat, O.W. Lindwasser, S. Olenych, J.S. Bonifacino, M.W. Davidson, J. Lippincott-Schwartz, and H.F. Hess. Imaging intracellular fluorescent proteins at nanometer resolution. *Science*, 313(5793):1642–1645, 2006.

[14] M.J. Rust, M. Bates, and X. Zhuang. Sub-diffraction-limit imaging by stochastic optical reconstruction microscopy (storm). *Nature methods*, 3(10):793–796, 2006.

[15] Rainer Heintzmann and Christoph G Cremer. Laterally modulated excitation microscopy: improvement of resolution by using a diffraction grating. In *BiOS Europe'98*, pages 185–196. International Society for Optics and Photonics, 1999.

[16] M.G.L. Gustafsson. Surpassing the lateral resolution limit by a factor of two using structured illumination microscopy. *Journal of Microscopy*, 198(2):82–87, 2000.

[17] K.A. Lidke, B. Rieger, T.M. Jovin, and R. Heintzmann. Superresolution by localization of quantum dots using blinking statistics. *Opt. Express*, 13(18):7052–7062, 2005.

[18] S. Cox, E. Rosten, J. Monypenny, T. Jovanovic-Talisman, D.T. Burnette, J. Lippincott-Schwartz, G.E. Jones, and R. Heintzmann. Bayesian localization microscopy reveals nanoscale podosome dynamics. *Nature Methods*, 9(2):195–200, 2011.

[19] MAA Neil, R. Juskaitis, and T. Wilson. Method of obtaining optical sectioning by using structured light in a conventional microscope. *Optics Letters*, 22(24):1905–1907, 1997.

[20] Daniel Appelt and Rainer Heintzmann. Structured illumination microscopy (SIM). In *Encyclopedia of Biophysics*, pages 2495–2502. Springer, 2013.

[21] R. Heintzmann. Structured illumination methods. *Handbook of Biological Confocal Microscopy*, pages 265–279, 2006.

[22] M.G.L. Gustafsson, L. Shao, P.M. Carlton, CJ Wang, I.N. Golubovskaya, W.Z. Cande, D.A. Agard, and J.W. Sedat. Three-dimensional resolution doubling in wide-field fluorescence microscopy by structured illumination. *Biophysical journal*, 94(12):4957–4970, 2008.

[23] Kai Wicker, Ondrej Mandula, Gerrit Best, Reto Fiolka, and Rainer Heintzmann. Phase optimisation for structured illumination microscopy. *Optics express*, 21(2):2032–2049, 2013.

[24] R. Heintzmann. Saturated patterned excitation microscopy with two-dimensional excitation patterns. *Micron*, 34(6-7):283–291, 2003.

[25] François Orieux, Eduardo Sepulveda, Vincent Loriette, Benoit Dubertret, and Jean-Christophe Olivo-Marin. Bayesian estimation for optimized structured illumination microscopy. *IEEE Transactions on image processing*, 21(2):601–614, 2012.

[26] Siyuan Dong, Jun Liao, Kaikai Guo, Liheng Bian, Jinli Suo, and Guoan Zheng. Resolution doubling with a reduced number of image acquisitions. *Biomedical optics express*, 6(8):2946–2952, 2015.

[27] L. Shao, P. Kner, E.H. Rego, and M.G.L. Gustafsson. Super-resolution 3D microscopy of live whole cell using structured illumination. *Nature methods*, 1734(5):1–5, 2011.

[28] Reto Fiolka, Markus Beck, and Andreas Stemmer. Structured illumination in total internal reflection fluorescence microscopy using a spatial light modulator. *Optics letters*, 33(14):1629–1631, 2008.

[29] P. Kner, B.B. Chhun, E.R. Griffis, L. Winoto, and M.G.L. Gustafsson. Super-resolution video microscopy of live cells by structured illumination. *Nature methods*, 6(5):339, 2009.

[30] E Hesper Rego, Lin Shao, John J Macklin, Lukman Winoto, Göran A Johansson, Nicholas Kamps-Hughes, Michael W Davidson, and Mats GL Gustafsson. Nonlinear structured-illumination microscopy with a photoswitchable protein

reveals cellular structures at 50-nm resolution. *Proceedings of the National Academy of Sciences*, 109(3):E135–E143, 2012.

[31] Dong Li, Lin Shao, Bi-Chang Chen, Xi Zhang, Mingshu Zhang, Brian Moses, Daniel E Milkie, Jordan R Beach, John A Hammer, Mithun Pasham, et al. Extended-resolution structured illumination imaging of endocytic and cytoskeletal dynamics. *Science*, 349(6251):aab3500, 2015.

[32] Aurélie Jost, Elen Tolstik, Polina Feldmann, Kai Wicker, Anne Sentenac, and Rainer Heintzmann. Optical sectioning and high resolution in single-slice Structured Illumination Microscopy by thick slice blind-SIM reconstruction. *PloS one*, 10(7):e0132174, 2015.

[33] Rainer Heintzmann, Thomas M Jovin, and Christoph Cremer. Saturated patterned excitation microscopy - a concept for optical resolution improvement. *JOSA A*, 19(8):1599–1609, 2002.

[34] M.G.L. Gustafsson. Nonlinear structured-illumination microscopy: wide-field fluorescence imaging with theoretically unlimited resolution. *Proceedings of the National Academy of Sciences of the United States of America*, 102(37):13081, 2005.

[35] Liisa Hirvonen, Ondrej Mandula, Kai Wicker, and Rainer Heintzmann. Structured illumination microscopy using photoswitchable fluorescent proteins. In *Biomedical Optics (BiOS) 2008*, pages 68610L–68610L. International Society for Optics and Photonics, 2008.

[36] Hui-Wen Lu-Walther, Wenya Hou, Martin Kielhorn, Yoshiyuki Arai, Takeharu Nagai, Michael M Kessels, Britta Qualmann, and Rainer Heintzmann. Nonlinear Structured Illumination Using a Fluorescent Protein Activating at the Readout Wavelength. *PloS one*, 11(10):e0165148, 2016.

[37] Kai Wicker. *Increasing resolution and light efficiency in fluorescence microscopy.* PhD thesis, King's college London, 2010.

[38] Ondrej Mandula. Patterned excitation microscopy, 2008. Master's thesis, King's College London.

[39] Steffen J. Sahl, Francisco Balzarotti, Jan Keller-Findeisen, Marcel Leutenegger,

Volker Westphal, Alexander Egner, Flavie Lavoie-Cardinal, Andriy Chmyrov, Tim Grotjohann, and Stefan Jakobs. Comment on "Extended-resolution structured illumination imaging of endocytic and cytoskeletal dynamics". *Science*, 352(6251):527, 2016.

[40] Dong Li and Eric Betzig. Response to comment on "Extended-resolution structured illumination imaging of endocytic and cytoskeletal dynamics". *Science*, 352(6285):527–527, 2016.

[41] E. Mudry, K. Belkebir, J. Girard, J. Savatier, E. Le Moal, C. Nicoletti, M. Allain, and A. Sentenac. Structured illumination microscopy using unknown speckle patterns. *Nature Photonics*, 6(5):312–315, 2012.

[42] Carl Zeiss Microimaging GmbH. ELYRA Enter the world of superresolution, 2012. Elyra manual.

[43] Nikon. N-SIM Super-Resolution Microscope System. `https://www.nikoninstruments.com/en_DE/Products/Super-resolution/N-SIM-Super-Resolution`. Accessed: 2017-05-04.

[44] GE Healthcare Life Sciences. DeltaVision OMX SR product sheet, 2017. Data file 29-1467-19 AA. Accessed: 2017-04-21.

[45] Amit Lal, Chunyan Shan, and Peng Xi. Structured illumination microscopy image reconstruction algorithm. *IEEE Journal of Selected Topics in Quantum Electronics*, 22(4):50–63, 2016.

[46] Pavel Křížek, Tomáš Lukeš, Martin Ovesnỳ, Karel Fliegel, and Guy M Hagen. SIMToolbox: a MATLAB toolbox for structured illumination fluorescence microscopy. *Bioinformatics*, 32(2):318–320, 2016.

[47] Marcel Müller, Viola Mönkemöller, Simon Hennig, Wolfgang Hübner, and Thomas Huser. Open-source image reconstruction of super-resolution structured illumination microscopy data in ImageJ. *Nature communications*, 7, 2016.

[48] Caroline A Schneider, Wayne S Rasband, and Kevin W Eliceiri. NIH Image to ImageJ: 25 years of image analysis. *Nature methods*, 9(7):671, 2012.

[49] Johannes Schindelin, Ignacio Arganda-Carreras, Erwin Frise, Verena Kaynig, Mark Longair, Tobias Pietzsch, Stephan Preibisch, Curtis Rueden, Stephan

Saalfeld, Benjamin Schmid, et al. Fiji: an open-source platform for biological-image analysis. *Nature methods*, 9(7):676–682, 2012.

[50] Sapna A Shroff, James R Fienup, and David R Williams. Phase-shift estimation in sinusoidally illuminated images for lateral superresolution. *JOSA A*, 26(2):413–424, 2009.

[51] Kai Wicker. Non-iterative determination of pattern phase in structured illumination microscopy using auto-correlations in fourier space. *Optics express*, 21(21):24692–24701, 2013.

[52] Reto Fiolka, Lin Shao, E Hesper Rego, Michael W Davidson, and Mats GL Gustafsson. Time-lapse two-color 3D imaging of live cells with doubled resolution using structured illumination. *Proceedings of the National Academy of Sciences*, 109(14):5311–5315, 2012.

[53] Christian Lesterlin, Graeme Ball, Lothar Schermelleh, and David J Sherratt. RecA bundles mediate homology pairing between distant sisters during DNA break repair. *Nature*, 506(7487):249–253, 2014.

[54] Liisa M Hirvonen, Kai Wicker, Ondrej Mandula, and Rainer Heintzmann. Structured illumination microscopy of a living cell. *European Biophysics Journal*, 38(6):807–812, 2009.

[55] R Ayuk, H Giovannini, A Jost, E Mudry, J Girard, T Mangeat, N Sandeau, R Heintzmann, K Wicker, K Belkebir, et al. Structured illumination fluorescence microscopy with distorted excitations using a filtered blind-SIM algorithm. *Optics letters*, 38(22):4723–4726, 2013.

[56] Kevin O'Holleran and Michael Shaw. Optimized approaches for optical sectioning and resolution enhancement in 2D structured illumination microscopy. *Biomedical optics express*, 5(8):2580–2590, 2014.

[57] Michael Shaw, Lydia Zajiczek, and Kevin O'Holleran. High speed structured illumination microscopy in optically thick samples. *Methods*, 88:11–19, 2015.

[58] Junhong Min, Jaeduck Jang, Dongmin Keum, Seung-Wook Ryu, Chulhee Choi, Ki-Hun Jeong, and Jong Chul Ye. Fluorescent microscopy beyond diffraction limits using speckle illumination and joint support recovery. *Scientific reports*,

3:1–6, 2013.

[59] Margret Keuper, Thorsten Schmidt, Maja Temerinac-Ott, Jan Padeken, Patrick Heun, Olaf Ronneberger, and Thomas Brox. Blind deconvolution of widefield fluorescence microscopic data by regularization of the optical transfer function (OTF). In *Proceedings of the IEEE Conference on Computer Vision and Pattern Recognition*, pages 2179–2186, 2013.

[60] Siyuan Dong, Pariksheet Nanda, Radhika Shiradkar, Kaikai Guo, and Guoan Zheng. High-resolution fluorescence imaging via pattern-illuminated Fourier ptychography. *Optics express*, 22(17):20856–20870, 2014.

[61] Mark Schmidt. minFunc. `http://www.cs.ubc.ca/~schmidtm/Software/minFunc.html`. Accessed: 2017-01-19.

[62] Stephen J Wright and Jorge Nocedal. *Numerical optimization*, volume 2. Springer New York, 1999.

[63] Walter A Carrington, Ronald M Lynch, ED Moore, Gerrit Isenberg, Kevin E Fogarty, and Fredric S Fay. Superresolution three-dimensional images of fluorescence in cells with minimal light exposure. *Science*, 268(5216):1483–1487, 1995.

[64] Peter J Verveer, MJ Gemkow, and Thomas M Jovin. A comparison of image restoration approaches applied to three-dimensional confocal and wide-field fluorescence microscopy. *Journal of Microscopy*, 193(1):50–61, 1999.

[65] Ferréol Soulez, Loïc Denis, Yves Tourneur, and Eric Thiébaut. Blind deconvolution of 3D data in wide field fluorescence microscopy. In *Biomedical Imaging (ISBI), 2012 9th IEEE International Symposium on*, pages 1735–1738. IEEE, 2012.

[66] Nadya Chakrova, Rainer Heintzmann, Bernd Rieger, and Sjoerd Stallinga. Studying different illumination patterns for resolution improvement in fluorescence microscopy. *Optics express*, 23(24):31367–31383, 2015.

[67] Clemens Roider, Rainer Heintzmann, Rafael Piestun, and Alexander Jesacher. Deconvolution approach for 3d scanning microscopy with helical phase engineering. *Optics express*, 24(14):15456–15467, 2016.

[68] Francesca Cella Zanacchi, Zeno Lavagnino, Michela Perrone Donnorso, Alessio Del Bue, Laura Furia, Mario Faretta, and Alberto Diaspro. Live-cell 3D super-resolution imaging in thick biological samples. *Nature methods*, 8(12):1047–1049, 2011.

[69] Alipasha Vaziri, Jianyong Tang, Hari Shroff, and Charles V Shank. Multilayer three-dimensional super resolution imaging of thick biological samples. *Proceedings of the National Academy of Sciences*, 105(51):20221–20226, 2008.

[70] Prashant Prabhat, Sripad Ram, E Sally Ward, and Raimund J Ober. Simultaneous imaging of different focal planes in fluorescence microscopy for the study of cellular dynamics in three dimensions. *IEEE transactions on nanobioscience*, 3(4):237–242, 2004.

[71] Erdal Toprak, Hamza Balci, Benjamin H Blehm, and Paul R Selvin. Three-dimensional particle tracking via bifocal imaging. *Nano letters*, 7(7):2043–2045, 2007.

[72] Edward J Botcherby, R Juškaitis, Martin J Booth, and Tony Wilson. An optical technique for remote focusing in microscopy. *Optics Communications*, 281(4):880–887, 2008.

[73] Bo Huang, Sara A Jones, Boerries Brandenburg, and Xiaowei Zhuang. Whole-cell 3d storm reveals interactions between cellular structures with nanometer-scale resolution. *Nature methods*, 5(12):1047–1052, 2008.

[74] Bo Huang, Wenqin Wang, Mark Bates, and Xiaowei Zhuang. Three-dimensional super-resolution imaging by stochastic optical reconstruction microscopy. *Science*, 319(5864):810–813, 2008.

[75] Sri Rama Prasanna Pavani, Michael A Thompson, Julie S Biteen, Samuel J Lord, Na Liu, Robert J Twieg, Rafael Piestun, and WE Moerner. Three-dimensional, single-molecule fluorescence imaging beyond the diffraction limit by using a double-helix point spread function. *Proceedings of the National Academy of Sciences*, 106(9):2995–2999, 2009.

[76] Shu Jia, Joshua C Vaughan, and Xiaowei Zhuang. Isotropic three-dimensional super-resolution imaging with a self-bending point spread function. *Nature photonics*, 8(4):302–306, 2014.

[77] Manuel F Juette, Travis J Gould, Mark D Lessard, Michael J Mlodzianoski, Bhupendra S Nagpure, Brian T Bennett, Samuel T Hess, and Joerg Bewersdorf. Three-dimensional sub-100 nm resolution fluorescence microscopy of thick samples. *Nature methods*, 5(6):527–529, 2008.

[78] Sripad Ram, Prashant Prabhat, Jerry Chao, E Sally Ward, and Raimund J Ober. High accuracy 3D quantum dot tracking with multifocal plane microscopy for the study of fast intracellular dynamics in live cells. *Biophysical journal*, 95(12):6025–6043, 2008.

[79] Sripad Ram, Dongyoung Kim, Raimund J Ober, and E Sally Ward. 3D single molecule tracking with multifocal plane microscopy reveals rapid intercellular transferrin transport at epithelial cell barriers. *Biophysical journal*, 103(7):1594–1603, 2012.

[80] Bruker. Vutara 352 Super Resolution Microscope. `https://www.bruker.com/products/fluorescence-microscopes/vutara-super-resolution-microscopy/technical-details.html`. Accessed: 2017-05-09.

[81] Stefan Geissbuehler, Azat Sharipov, Aurélien Godinat, Noelia L Bocchio, Patrick A Sandoz, Anja Huss, Nickels A Jensen, Stefan Jakobs, Jörg Enderlein, F Gisou Van Der Goot, et al. Live-cell multiplane three-dimensional super-resolution optical fluctuation imaging. *Nature communications*, 5, 2014.

[82] Sara Abrahamsson, Jiji Chen, Bassam Hajj, Sjoerd Stallinga, Alexander Y Katsov, Jan Wisniewski, Gaku Mizuguchi, Pierre Soule, Florian Mueller, Claire Dugast Darzacq, et al. Fast multicolor 3D imaging using aberration-corrected multifocus microscopy. *Nature methods*, 10(1):60–63, 2013.

[83] Sara Abrahamsson, Molly McQuilken, Shalin B Mehta, Amitabh Verma, Johannes Larsch, Rob Ilic, Rainer Heintzmann, Cornelia I Bargmann, Amy S Gladfelter, and Rudolf Oldenbourg. MultiFocus Polarization Microscope (MF-PolScope) for 3D polarization imaging of up to 25 focal planes simultaneously. *Optics express*, 23(6):7734–7754, 2015.

[84] Sara Abrahamsson, Rob Ilic, Jan Wisniewski, Brian Mehl, Liya Yu, Lei Chen, Marcelo Davanco, Laura Oudjedi, Jean-Bernard Fiche, Bassam Hajj, et al.

Multifocus microscopy with precise color multi-phase diffractive optics applied in functional neuronal imaging. *Biomedical optics express*, 7(3):855–869, 2016.

[85] Bassam Hajj, Jan Wisniewski, Mohamed El Beheiry, Jiji Chen, Andrey Revyakin, Carl Wu, and Maxime Dahan. Whole-cell, multicolor superresolution imaging using volumetric multifocus microscopy. *Proceedings of the National Academy of Sciences*, 111(49):17480–17485, 2014.

[86] Laura Oudjedi, Jean-Bernard Fiche, Sara Abrahamsson, Laurent Mazenq, Aurélie Lecestre, Pierre-François Calmon, Aline Cerf, and Marcelo Nöllmann. Astigmatic multifocus microscopy enables deep 3D super-resolved imaging. *Biomedical Optics Express*, 7(6):2163–2173, 2016.

[87] Carlas S Smith, Stephan Preibisch, Aviva Joseph, Sara Abrahamsson, Bernd Rieger, Eugene Myers, Robert H Singer, and David Grunwald. Nuclear accessibility of β-actin mRNA is measured by 3D single-molecule real-time tracking. *J Cell Biol*, 209(4):609–619, 2015.

[88] Ralph W Gerchberg and W.O. Saxton. A practical algorithm for the determination of the phase from image and diffraction plane pictures. *Optik*, 35(2):237–246, 1972.

[89] Paul M Blanchard and Alan H Greenaway. Simultaneous multiplane imaging with a distorted diffraction grating. *Applied optics*, 38(32):6692–6699, 1999.

[90] Bo-Jui Chang, Li-Jun Chou, Yun-Ching Chang, and Su-Yu Chiang. Isotropic image in structured illumination microscopy patterned with a spatial light modulator. *Optics express*, 17(17):14710–14721, 2009.

[91] Ronny Förster, Hui-Wen Lu-Walther, Aurélie Jost, Martin Kielhorn, Kai Wicker, and Rainer Heintzmann. Simple structured illumination microscope setup with high acquisition speed by using a spatial light modulator. *Optics express*, 22(17):20663–20677, 2014.

[92] Hui-Wen Lu-Walther, Martin Kielhorn, Ronny Förster, Aurélie Jost, Kai Wicker, and Rainer Heintzmann. fastSIM: a practical implementation of fast structured illumination microscopy. *Methods and Applications in Fluorescence*, 3(1):014001, 2015.

[93] Liyan Song, Hui-Wen Lu-Walther, Ronny Förster, Aurélie Jost, Martin Kielhorn, Jianying Zhou, and Rainer Heintzmann. Fast structured illumination microscopy using rolling shutter cameras. *Measurement Science and Technology*, 27(5):055401, 2016.

[94] Ronny Förster. Fast Structured Illumination Microscopy, 2012. Master's thesis, Friedrich Schiller University Jena.

[95] Allan W Snyder and John Love. *Optical waveguide theory*. Springer Science & Business Media, 2012.

[96] Forth Dimension Displays. Amplitude Modulation - Optical Principle of a FLCoS microdisplay. `http://www.forthdd.com/technology/optical-principle/`. Accessed: 2017-05-13.

[97] Forth Dimension Displays. -3DM Hardware User Manual, 2009. SLM manual.

[98] Ma del Mar Sánchez-López, Ignacio Moreno, and Antonio Martínez-García. Teaching diffraction gratings by means of a phasor analysis. In *Education and Training in Optics and Photonics*, page EMA1. Optical Society of America, 2009.

[99] Kevin O'Holleran and Michael Shaw. Polarization effects on contrast in structured illumination microscopy. *Optics Letters*, 37(22):4603–4605, 2012.

[100] Hamamatsu Photonics K.K. Digital Camera C11440-22CU Instruction manual, 2012.

[101] Hamamatsu Photonics K.K. Orca-Flash 4.0 V2 technical note, 2015.

[102] Omicron-Laserage Laserprodukte GmbH. User manual LuxX laser series, 2015.

[103] Meadowlark Optics. Liquid Crystal Digital Controller Manual, 2011.

[104] Ronny Förster, Kai Wicker, Walter Müller, Aurélie Jost, and Rainer Heintzmann. Motion artefact detection in structured illumination microscopy for live cell imaging. *Optics Express*, 24(19):22121–22134, 2016.

[105] Max Born and Emil Wolf. *Principles of optics: electromagnetic theory of propagation, interference and diffraction of light*. Elsevier, 1980.

[106] Jan Modersitzki. *FAIR: flexible algorithms for image registration.* SIAM, 2009.

Acknowledgements

First, I would like to express my deepest gratitude to my Ph.D supervisor Prof. Rainer Heintzmann. For the continuous support during my Ph.D study, for his immense knowledge and eagerness to share it, and for his guidance in all phases of my work as well as for the great help on writing this thesis, I am very grateful.
Special thanks go to Dr. Anne Sentenac and her team at the Fresnel Institute in Marseille - especially Roland Ayuk, Prof. Hugues Giovannini and Dr. Kamal Belkebir - for welcoming me for four months. The experience was extremely enriching and gave a decisive and successful start to the blind-SIM project.
I am also very grateful to Dr. Sara Abrahamsson for giving me the opportunity to work on the MF-SIM project, for lending me the MFM components and for the numerous pieces of advice. I would also like to thank Prof. Hjalmar Brismar and Dr. Hans Blom for inviting me to Stockholm for two productive weeks and for making their Elyra microscope available to us.
Both Anne and Sara did not only act as second supervisors on the respective part of my work but are also for me inspiring figures of successful women in science. I consider myself very lucky to have been given the chance to collaborate with them.
I also thank Dr. Reto Fiolka for the constructive remarks on MF-SIM reconstruction and for the inspiring and motivating discussions.

I had a wonderful time in the FA8 at the Leibniz Institute of Photonic Technology in Jena thanks to all my colleagues who created a productive yet friendly work environment. For being more than labmates, for all the fun, as well as for the support through harder times, thank you, you could not have been better.
To Dr. Kai Wicker, Ronny Förster, Dr. Walter Müller, Dr. Christian Karras and Dr. Hui-Wen Lu-Walther, thank you for the invaluable help in the lab and for the many enlightening discussions. I especially want to stress that Ronny pioneered a significant part of the work on the fast-SIM project and thank him for being always available and patient to share his knowledge and experience with me. This thesis would never have been ready on time without the valuable help of Christian, Ronny, Walter, Kai, as well as Benedict Diederich and Sapna Shukla to whom I am therefore deeply indebted.
I am very grateful to Robert Kretschmer and Florian Blase for the great engineering

support, especially concerning the design and fabrication of the scanning stage. They, as well as Dr. Martin Kielhorn and Kishore Mariappan, assisted me also for the realisation of the electronic circuit.
Many thanks to Franck Gounou for his excellent work on the multi-lens array design.
Ivana Šumanova Šestak and Martin Reifarth receive my gratitude for the simple yet precise explanations on chemistry and biology.
My time as a Ph.D student was greatly facilitated by the constant, friendly support and availability of Bärbel Schäfer, Antje Raabe, Marion Krause and Benita Göbel.

Last but not least, I would like to thank my beloved family and friends for being here for me in moments of doubt and pressure, for creating a loving and also fun atmosphere where I could relax and gain strength and motivation. I am forever grateful to my parents who bestowed me the taste for science in general, who taught me to appreciate the value of curiosity, education and knowledge and who supported me in all possible ways throughout the years.
I would like to make a special note of thanks to all my former teachers, professors and mentors who I was honoured to meet on my path and who contributed to my development. I am happy of every single decision I took each time there was a choice in orientation, because it led me here, and this is thanks to you.
To Markus, who is so much more than a partner and a soulmate, thank you for filling my life with love and happiness, for being patient and supportive, and for all the fun and unforgettable moments. I really appreciate the way we can share and discover together, for instance on scientific topics, and in this case I should again express my gratitude for the help with LaTeX writing. We already share memories, and I am looking forward to creating a life full of stories with you.

Selbständigkeitserklärung

Ich erkläre, dass ich die vorliegende Arbeit selbständig und unter Verwendung der angegebenen Hilfsmittel, persönlichen Mitteilungen und Quelle angefertigt habe.

Jena, den.....

Unterschrift der Verfasserin